Processing Rate and Energy Consumption Analysis for Additive Manufacturing Processes: Material Extrusion and Powder Bed Fusion

by

Sheng Jiang

B.S. Mechanical Engineering, University of Michigan, 2013
B.S. Electric Engineering, Shanghai Jiaotong University, 2013

SUBMITTED TO THE DEPARTMENT OF MECHANICAL ENGINEERING IN PARTIAL FULFILLMENT OF THE REQUIREMENTS FOR THE DEGREE OF

MASTER OF SCIENCE IN MECHANICAL ENGINEERING

AT THE

MASSACHUSETTS INSTITUTE OF TECHNOLOGY

June 2017

Signature of Author Signature redacted
Department of Engineering
May 19th, 2017

Certified by Signature redacted
Timothy G. Gutowski
Professor of Mechanical Engineering

Accepted by Signature redacted
Rohan Abeyaratne
Quentin Berg Professor of Mechanics
Department of Mechanical Engineering

Processing Rate and Energy Consumption Analysis for Additive Manufacturing Processes: Material Extrusion and Powder Bed Fusion

by

Sheng Jiang

Submitted to the Department of Mechanical Engineering
on May 19th, 2017, in partial fulfillment of
the requirements for the degree of
Master of Science in Mechanical Engineering

Abstract

Additive technologies have given birth to an expanding industry now worth 5.1 billion dollars. It has been adopted widely in design and prototyping as well as manufacturing fields. Compared to conventional technologies, additive manufacturing technologies provides opportunity to print unique complex-shaped geometries. However, it also suffers from slow production rate and high energy consumption. Improving the rate and energy becomes an important issue to make additive manufacturing competitive with conventional technologies. Among all the different limiting factors including printing strategy, heat transfer and mechanical movement limitations, heat transfer is the fundamental limiting barrier preventing further improvement the production rate. This thesis looks at the heat transfer mechanisms in material extrusion and powder bed fusion processes. In all the models developed for these two processes, processing rate is bounded by an adiabatic rate limit at which all the input energy is perfectly utilized to heat up the material to its molten/flowable state. In material extrusion, fused deposition technology suffers low throughput due to poor conductive heat transfer, big area additive manufacturing technology achieves high throughput by introducing viscous heating at the cost of resolution. In powder bed fusion, due to the intensive laser heating, the process window is limited to ensure high density material while avoid exessive evaporation. Further study quantifies the inefficiency from heat transfer mechanisms which leads to lower processing rates than the adiabatic rate limit. Energy consumption for material extrusion and powder bed fusion machines are reviewed to evaluate significance of energy consumed to heat up the material. For fused deposition technology, most of the energy is consumed by environment heating; while for powder bed fusion technology, laser unit takes the most energy. Life cycle energy consumption for products made with powder bed fusion process is compared with same/similar parts made from conventional manufacturing processes to explore senarios in which manufacturing with additive technologies is less energy intensive.

Thesis Supervisor: Timothy G. Gutowski
Professor of Mechanical Engineering

Acknowledgement

This thesis is a poetic path into the woods.

First and foremost, I would like to extend my sincere gratitude to my advisor, Professor Timothy Gutowski, for being an excellent mentor throughout the past four years. From his great mind, I learned the fundamental principles of conducting research. He equipped me with all the skills and abilities a young engineer would ever need to solve research problems, and gifted me with the spirit to be always seeking and questioning until the pursuit of truth. From his kind heart, I learned patience, fortitude, forgiveness and faith. It is through these wells of life that I gain strength and courage to embrace this journey. I am thankful to the great opportunity learning and working with him, and I will never forget all the meetings and talks we have about research and life.

I will always cherish the time I spent with all my beloved colleagues in Environmentally Benign Manufacturing group. Dan Cooper and Katie Rossie have been great big brother and big sister to me. Together they bring so much energy and laughter to the lab and into my life. I am truly blessed to have these two caring lab mates who are not only always there when I am feeling down, but also always more than ready to surround their loving arms around me during cold nights. I spent so many late nights face to face with Sumant Raykar working in the lab that I find nobody else more suitable to spend even more time together swimming and sailing. We shared so many stories and secrets that turned us from colleagues into best friends in Boston. I will always remember all the happy times I spent with Gero Corman, Anne Raymond, Marta Baldi, Michael Lloyd, Michael Hausmann, Mathias Schmieder and Karine Ip. Together we drank so much beer, and together we sang so many Karaoke's.

I would also like to thank Karuna Mohindra for being a great administrator for the lab, and Dean Jason McKnight for great his help during my Master's program. Thanks to Leslie Regan from the MIT Mechanical Engineering Graduate Office who has always been kind, patient and helpful.

Last but not least, I would like to thank my family and friends. Mom and dad, thank you for your unconditional love and support, you have always been the harbor in my life. My father, who's also a mechanical engineer, is the role model I looked up to when beginning this journey at MIT; and my mother taught me how to live in this world with a sensitive and loving heart. I love you. Thank my uncle, aunt and little cousin for all the time we spent together back in the days and while we were in Chengdu. It's the love from you and my parents that helped me through the toughest time of my life. Guanye Zheng and Wangyang Xia, my best friends, thank you for always being there, talking to me and listening to me no matter how late it is into the night. It is from you that I learned true friendship would never fade with time or distance. I would also like to thank Yiwei Chen, Haichen Liu, Wenjia Zhang, Shaoyi Li, Jiacheng Gu, Yizhe Wang, Hao Wang, Zhuoxuan Li, Xiawei Wang, Brian Chuang, Ethan Wampler, Michelle Bacarella and many more for being great friends in my life and making this journey warm and happy.

I am deeply loved and I love you all deeply.

Contents

List of Figures

List of Tables

I. Introduction

Additive manufacturing is the term to describe technologies that directly builds three dimensional objects from computer data, usually computer aided design (CAD) file, of a three dimensional model. It is also known as 3D printing, rapid prototyping, freeform fabrication, etc. An additive manufacturing process often involves joining or solidifying material layer by layer to make dense parts. Compared to well-known conventional manufacturing technologies, additive manufacturing technologies offer enormous design freedom for complex geometries partially because of the absence of tooling in the printing process. Moreover, it allows customized unique design to be manufactured at lower cost and with less effort, especially when using material extrusion machines. It is therefore widely adopted by researchers for design and prototyping. Over the decades, researchers have broaden the range of printable materials from polymer to ceramics, metal, and, nowadays, human tissue [1]. As to make additive manufacturing technologies competitive with conventional manufacturing technologies, improving processing rate and energy consumption has always been a heated research topic. However, the throughput of additive technologies still remains orders of magnitude slower than conventional technologies, while the energy consumption stays one to two orders of magnitude higher. It is therefore the interest of this thesis to apply mathematical and physics principles to provide a quantitative performance measure of print rate, and to identify possible barriers and limitations for future improvement. In this thesis, we specifically look into powder bed fusion and material extrusion processes because of their popularity on the market and their capability of printing functional parts.

The first part of this thesis gives an introduction to the field of additive manufacturing, standardizing terminology and classifying different categories of additive technologies. In this part, we also explore the current standing of powder bed fusion technology in both industrial and research fields. Topics on product quality, processing rate and cost for metal powder bed fusion technology are reviewed.

In the second part, we present two different heat transfer models for polymer extrusion processes fused deposition modeling and big area additive manufacturing respectively. We demonstrate that heat transfer mechanism is correlated with the processing rate for both processes. Moreover, it could be a limiting barrier for achieving higher throughput. With these models, we try to explain the big processing rate difference between the two processes, and offer potential routes for increasing their processing rate respectively.

In the next part, we present three different analytical models to study the processing rate of selective laser melting with the focus on conductive heat transfer. Among these three models, an adiabatic processing rate model predicts the theoretic maximum processing rate by assuming perfect energy transmission into the material. The theoretic maximum processing rate is then used as baseline to evaluate the performance of current powder bed fusion processes. To quantify the effect of heat transfer on limiting the processing rate, some crucial physical parameters involved in the process are reviewed including laser material absorptivity, thermal conductivity, capillarity, etc. The other two models are constructed to explain the discrepancy between theoretical maximum processing rate and empirical measurement.

In the final part, we studied the energy consumption for typical metal powder bed fusion process. The lifecycle energy consumption for products made with metal powder bed fusion process breaks down into energy consumption during five different phases: material production, manufacturing, transport, use phase and end of life. The chapter focuses on the first three phases, highlighting major energy consumption units. Two metal powder bed fusion and one polymer powder bed fusion case studies are presented to compare their energy consumption with corresponding conventional manufacturing technologies. In these comparisons, we seek the boundaries within which additive manufacturing shows advantages in terms of energy consumption.

II. State of the Technology

1. Terminology and technology definition

The terminology for additive manufacturing processes has been chaotic from the very beginning. Since a lot of technologies share the concept of additively adding material to build a part, every different technology is branded separately for promotion. Some of the names are related to the nature of the process and applied physical principles, while the others are less related. The abundance in the technology definition can pose difficulties/barriers in education and communication in the additive manufacturing area. In the current stage, especially, due to the fast development and process/principle variation in designs, standardizing the whole additive manufacturing processes is challenging.

Standard terminology for additive manufacturing technologies (F2792 – 12a)[2], published by ASTM Committee F42, categorizes additive manufacturing processes into seven subgroups, i.e. binder jetting, directed energy deposition, material extrusion, material jetting, powder bed fusion, sheet lamination, and vat photopolymerization. Each technology category has processes and/or underlining physical principle different from the others. Different technology name and trademarks are then categorized accordingly and shown in Table II.1 below.

Technology category	Materials	Technology name/trademarks	Manufacturer
Binder jetting	Polymers, ceramics, metal powders	3D Printing (3DP)	3D Systems
			ExOne
			Voxeljet
Directed energy deposition	Metal powders	Laser-engineered net shaping (LENS)	Optomec
		Direct metal deposition (DMD)	POM Group (AM3D)
		Powder Deposition Welding	Trumpf (DepositionLine)
		Metal Powder Application (MPA)	Hermle
		Laser deposition welding & milling (hybrid)	DMG Mori Seiki Co.
	Metal wires	Electron Beam Direct Manufacturing (EBDM)	Sciaky Inc.
Material extrusion	Thermoplastic filaments	Fused Deposition Modeling (FDM)	Stratasys
		Fused Layer Modeling (FLM)	3D Systems
			Beijing Tiertime
			Delta Micro Factory
			Fabbster

			MakerBot Industries (Stratasys since 2013)
			RepRap project (open source project)
	Thermoplastic pallets	Plastic Freeforming	Arburg
Material jetting	UV curable plastics	Multi-Jet Modeling (MJM)	3D Systems
		PolyJet Modeling (PJM)	Stratasys (Objet)
	Waxes	Thermal jetting	Solidscape
Powder bed fusion	Thermoplastics	Selective Laser Sintering (SLS)	3D Systems
		Selective Heat Sintering	Blueprinter
		Laser Sintering (LS)	EOS GmbH
	Metals	Selective Laser Melting (SLM)	SLM Solutions GmbH
		Direct Metal Laser Sintering (DMLS)	EOS GmbH
		Direct Metal Printing (DMP)	3D Systems
		LaserCUSING	Concept Laser GmbH
		Electron Beam Melting (EBM)	Arcam AB
Sheet lamination	Paper, plastics	Laminated Object Modeling (LOM)	Helisys Inc.
	Metal strips	Ultrasonic Additive Manuf. (UAM)	Fabrisonic (Soldidica)
Vat photopolymerization	Photopolymers	Stereolithography (SL)	3D Systems
		Digital Light Processing (DLP)	Envisiontec GmbH

Table II.1 Classification of additive manufacturing technologies [3]

1.1.Classification of additive manufacturing

1.1.1. Binder jetting

Binder jetting technology is characterized by ASTM standard as an additive manufacturing process in which a liquid bonding agent is selectively deposited to join powder materials. An inkjet print head selectively deposits liquid binding material onto a thin layer of powder. The powder material is spread over the entire building plate after pattern for each layer is successfully printed. The bonded green part could be infiltrated or heat treated in a separate piece of equipment depending on the material and desired properties.

The technology was developed by Emanuel Sachs and Michael Cima at Massachusetts Institute of Technology in 1993. It is also known by "Three-Dimensional Printing", although the term has expended its meaning to include more generic additive manufacturing technologies. Z Corporation, acquired by 3D Systems in 2013, was the pioneer in commercializing this technology. By using liquid binder of different colors, the technology is suited to print full color prototypes with a rather fast speed and with low power requirement. The material, on the other hand, is restricted to composite powders. ExOne applies liquid binder to glue metal powders and sand. For metal products, after the green part is created, it's sintered and infiltrated with molten bronze in a separate furnace. The printing speed and printing capacity are significantly better than other technologies, but lengthy post treatment is required.

1.1.2. Directed energy deposition

Directed energy deposition technology is characterized by ASTM standard as an additive manufacturing process in which focused thermal energy is used to fuse materials by melting as they are being deposited. Powerful thermal energy source, typically laser or electron beam, is integrated coaxially on a nozzle which is used to deliver material. Energy is directed to heat a focused region on a substrate to create a melt pool; the directed energy also melts the material being deposited to the melt pool simultaneously. Most machines are equipped with inert gas system to process metal material. The nozzle is typically mounted on a multi-axis motion system which allows material to be easily deposited at desired area. The technology is mostly applied to coat metal part surfaces and to repair damaged parts.

Laser engineered net shaping (LENS) technology is developed by Optomec under this category to process materials in an enclosed inert gas chamber. Direct metal deposition (DMD) technology developed by DM3D Technology features a coaxial inert gas shielding system integrated on depositing nozzle. Due to the similarity in motion control system, it is possible to equip existing multi-axis tooling system with material delivering nozzle to create directed energy deposition system. DMG Mori took a further step to combine directed energy deposition system with traditional CNC machining setup, creating a hybrid machine. When compared to powder bed fusion technologies, processing rate is higher for directed energy deposition but the printed parts generally have relatively poor geometric accuracy.

1.1.3. Material extrusion

Material extrusion technology is characterized by ASTM standard as an additive manufacturing process in which material is selectively dispensed through a nozzle or orifice. Material (in filament or pellet form) is usually stored in a separate spool/tank from the building chamber. During the process, material feeds through a heating zone where its temperature is elevated for it to reach flowable state. It is then deposited following the programmed path through an orifice which is mounted on a gantry system. When it cools down to the temperature of the building chamber, the extruded material bonds to the adjacent extrusion line and the printed layer underneath. Some/full environment heating is applied to ensure the bonding process and to avoid severe shrinkage during the building process.

Fused deposition modeling (FDM), trademarked by Stratasys, is a material extrusion process that applies electric heating to filament material. The technology developed by Stratasys features two materials for printing: modeling material and supporting material. The modeling material constitute the product, while the supporting material could be easily removed during post processing (e.g. dissolve in certain chemical solution). A variety of thermal plastic material is available for FDM technology, including acrylonitrile butadiene styrene (ABS) based material, nylon, polycarbonate, polyetherimide material, etc. The process accuracy is restricted by the orifice dimension, and the part suffers from shrinkage when removed from the heated building environment. When compared to conventional manufacturing methods (e.g. injection molding, extrusion, etc.), the throughput is orders of magnitude lower for all FDM machines across different scales from desktop prototyping machines to industrial manufacturing machines.

Big area additive machining is developed at Oak Ridge National Laboratory by Cincinnati Inc., aiming to print large-dimension part at a fast processing rate. An extruder is used to heat and melt materials in pellet form. It is mounted on a gantry system to deliver molten material to designated position. The machine can print carbon fiber filled ABS material at a rate up to 45 kg/hr. The addition of carbon fibers improves the strength of the built part. Accuracy and surface finish is sacrificed for using a large diameter orifice to achieve fast printing speed. As a result, heavy post processing is usually required.

1.1.4. Material jetting

Material jetting technology is characterized by ASTM standard as an additive manufacturing process in which droplets of build material are selectively deposited. During the process, a gantry system carries the inkjet printer head to desired position, liquid droplets are then dispensed onto the building platform. The droplets are hardened and solidified through cooling or UV curing. Because of their high viscosity, polymer and wax material are commonly used for this technology.

3D systems adopts the method of using multiple nozzles to print supporting material and photopolymer building material. This also increases the printing speed compared to single nozzle setups. The supporting material will be melted away during post processing. Material jetting processes is usually applied in prototyping because of its high resolution, good accuracy, and smooth surface finish.

1.1.5. Powder bed fusion

Powder bed fusion technology is characterized by ASTM standard as an additive manufacturing process in which thermal energy selectively fuses regions of a powder bed. The thermal energy applied to induce fusion between particles is usually delivered through a laser system with specific wavelength or an electron beam system. Apart from a powerful energy source, all the powder bed fusion processes consist of a powder delivery system and a mechanism to prescribe energy in designated region. In each cycle of steady building phase, a building platform is first lowered by one layer thickness, then a new layer of material is applied on the substrate plate/fused layer with the help of a coater, finally energy is directed to fuse target area on the new layer. 3D geometry can thus be produced layer by layer.

Selective laser sintering, developed at University of Texas Austin by Joseph Beaman, is the first commercialized powder bed fusion process. While the original purpose was to produce polymer products, it has extended the range of applicable material to include metals under the name of Direct metal printing. Other laser powder bed fusion technology companies also introduce brand names for their systems when they enter the business. Arcam AB applies electron beam source to selectively fuse powder material. This process is known as electron beam melting.

Currently, metal, polymer and composites are the three major material categories developed with powder bed fusion technology. Protective gas is introduced in a closed chamber when reactive powders (for example, titanium, aluminum, etc.) are processed. Since most material can be fused by applying thermal energy, a bigger variety of material can be potentially processed within these three categories. Unused powders could be recycled depending on the requirements of specific applications. However, the process has a rather low throughput, and requires heavy post processing to achieve desired geometry accuracy as well as to release residual stress.

1.1.6. Sheet lamination

Sheet lamination technology is characterized by ASTM standard as an additive manufacturing process in which sheets of material are bonded to form an object. During the process, sheet material is first positioned in place on the building platform. Adjacent layers are then bonded together using ultrasonic welding or adhesive depending on materials. To achieve the desired geometry, traditional machining is required during or after the layering process.

Ultrasonic additive manufacturing process from Solidica Inc. uses sheet metal material including aluminum, copper, stainless steel and titanium. The welding temperature is lower than the melting temperature of these metals, and this allows for internal geometries to be created. Different materials can be bonded together using this technology at rather low energy cost. Laminated Object Modeling, developed by Helisys, USA, uses adhesive to bond paper sheets material. This process is often used for aesthetic and visual prototypes.

1.1.7. Vat photopolymerization

Vat photopolymerization technology is characterized by ASTM standard as an additive manufacturing process in which liquid photopolymer in a vat is selectively cured by light-activated polymerization. Ultraviolet light is used to cure resins at specific locations within the top layer in a vat of material. The build platform is lowered one layer after curing while new layer liquid resin being added on top of the previous one.

Stereolithography (SLA) is trademarked by 3D Systems, it has a high level of accuracy and good surface finish because of its fine layer thickness. However, it often requires extra support structures compared to polymer powder bed fusion processes. After desired geometry is achieved, post curing process takes place to increase the mechanical strength of the part such that it is strong enough for structural use. The process of photopolymerization is achieved with a single laser and optics. Digital light processing technology uses a commercial projector to selectively cure a whole material area at a time. These processes, while producing good accuracy parts, suffer from low processing rate. Carbon 3D increases the processing rate of vat

photopolymerization by introducing an oxygen shield to constrain the curing process at certain depth. The process also uses a projector to cure a whole area of material at a time.

2. Scope of powder bed fusion

Through the 35 years of development, powder bed fusion process has become one of the major additive manufacturing technologies over the world. The major machine manufacturers are from the United States, Europe, China and Japan as can be seen in Figure II.1. While the technology was first developed in the United States, Europe has become the center of powder bed fusion technologies with EOS GmbH being the largest powder bed fusion manufacturer in the world. Various Chinese machine manufacturers are also catching up to take a share of the market.

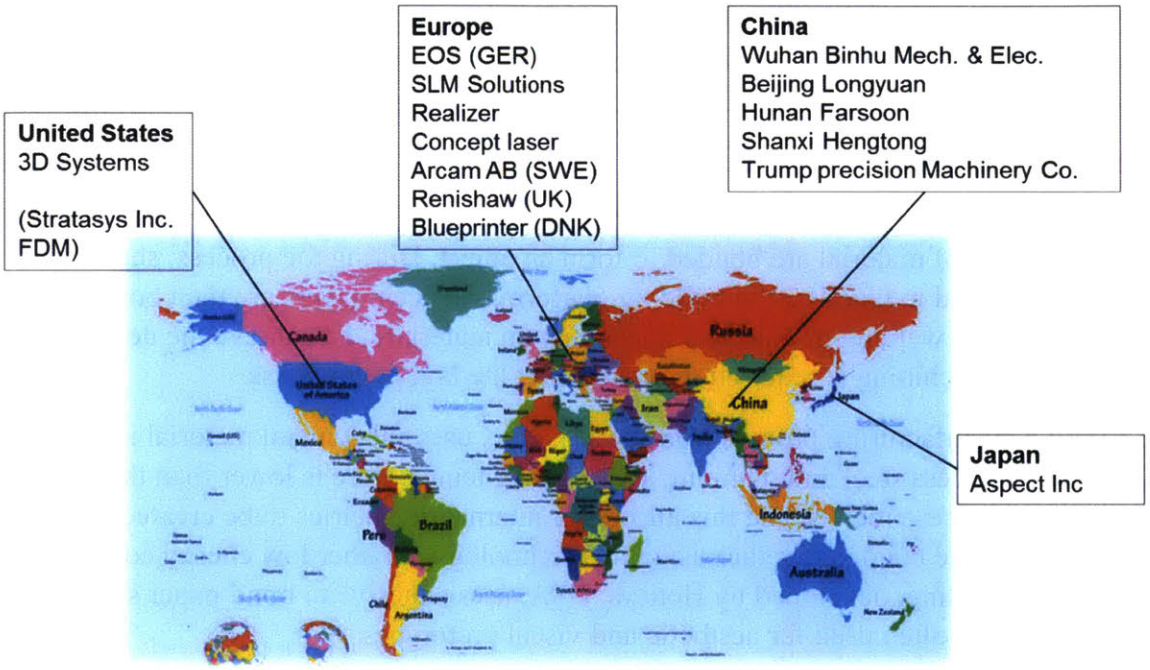

Figure II.1 Powder bed fusion machine manufacturers over the world [4]

Because of the high requirement on processing environment and the small size powders involved, parts made from powder bed fusion are built in an enclosed chamber. The maximum part geometry is therefore restricted by its chamber size. Currently the maximum chamber size metal powder bed machine in the world is the Concept Laser Xline 1000R at 120 L, while for polymer powder bed machine, it is the HRPS-VIII from Wuhan Binhu Mechanical and Electrical Company at 1000L as shown in Figure II.2. Machines from other manufacturers are equipped with a chamber size smaller than 60 L. The increasing size of the chamber also increases the cost of the systems. The price of laser source metal powder bed fusion machines approximately follows a linear trend with respect to the chamber size as shown in Figure II.3. The electron beam metal powder bed fusion machines appear to be more expensive than laser source machines with the same chamber size. For polymer powder bed fusion machines, the price also increases with the chamber size of the machines as shown in Figure II.4. An interesting observation indicates that the price for machines in China follows a different trend from other

manufacturers over the world. The polymer machines from China are generally sold at a low price compared to those from other global manufacturers with the same chamber size.

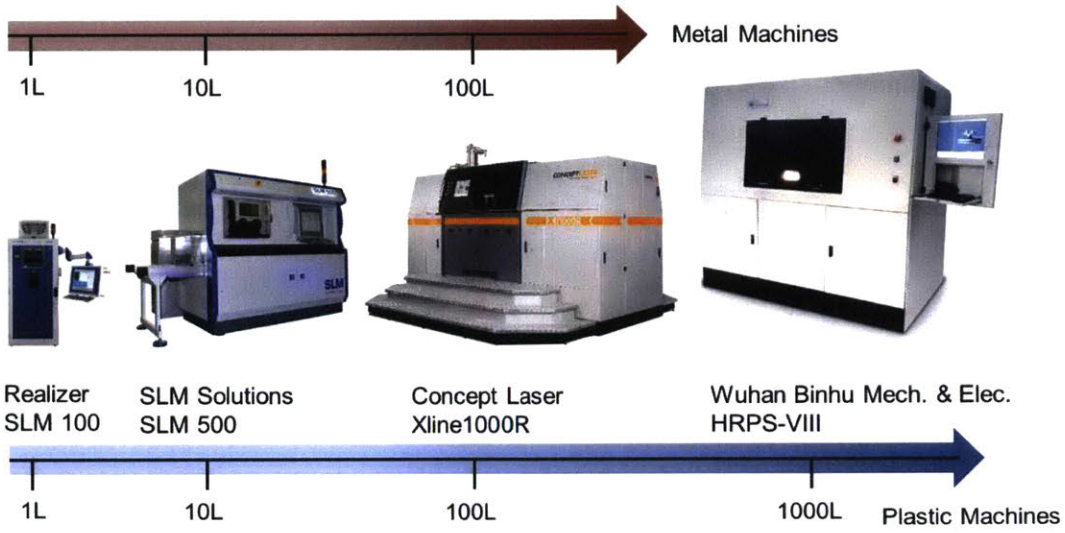

Figure II.2 Machines with different chamber sizes [4]

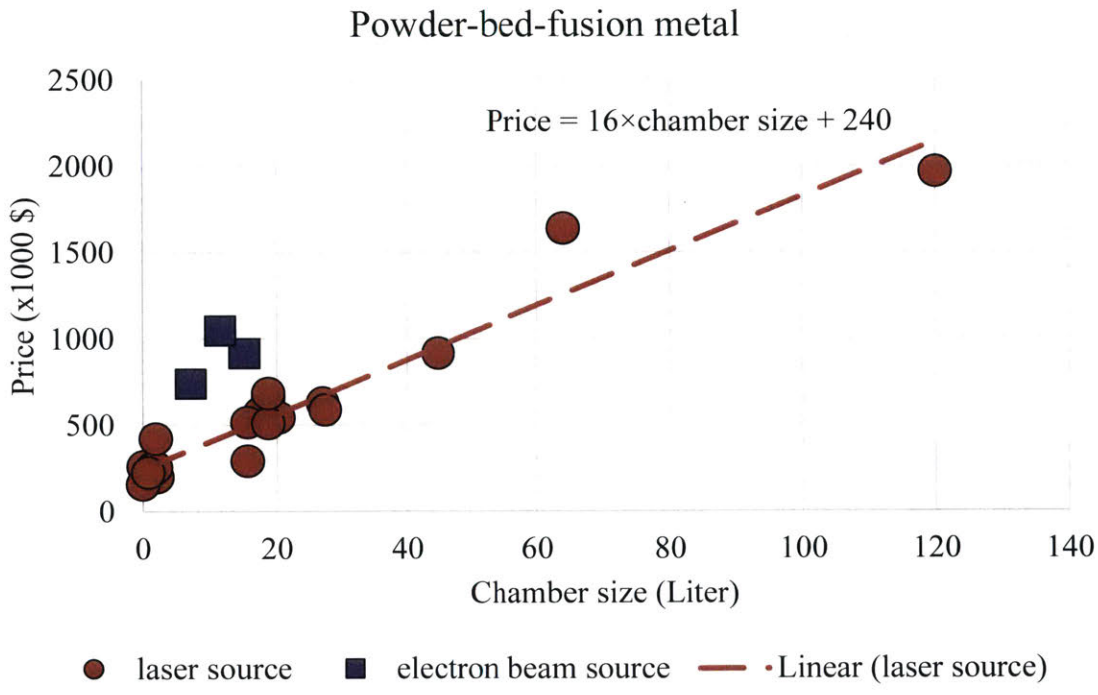

Figure II.3 Price vs chamber size for metal powder bed fusion [4]

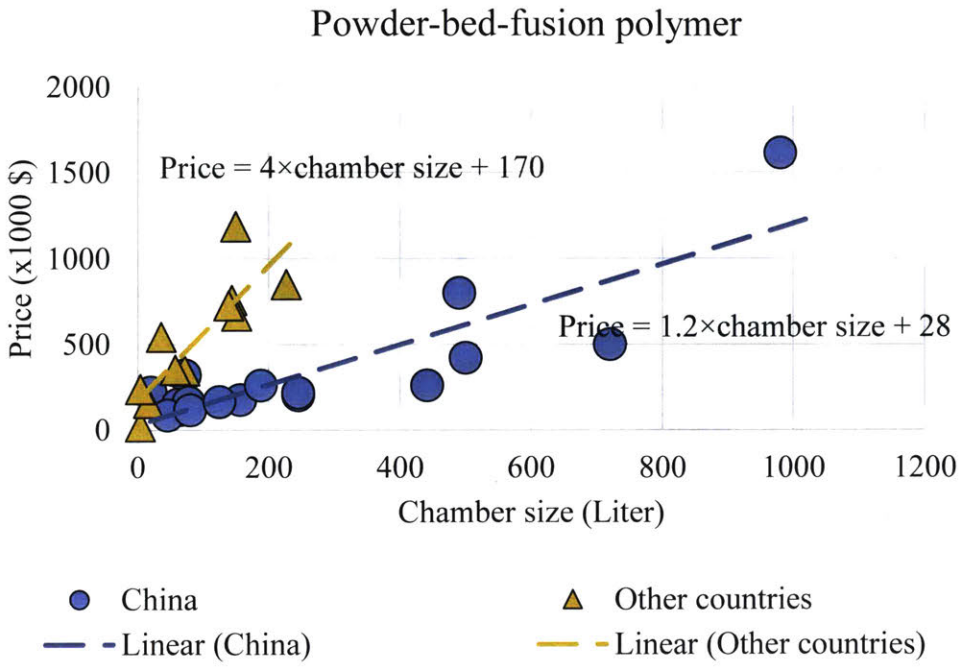

Figure II.4 Price vs chamber size for polymer powder bed fusion [4]

Metal additive technologies have been applied mostly in aerospace, tooling manufacturing and medical area because of the characteristics of the process. In particular, the process is favored when building parts with low buy to fly ratio and when complex geometry is desired. GE has announced the first 3D-printed part certified by the US Federal Aviation Administration (FAA) for a commercial jet engine. The fist-sized T25 housing for a compressor inlet temperature sensor, as shown in Figure II.5, was fabricated by GE Aviation and will be retrofitted to over 400 GE90-94B jet engines on Boeing 777 aircraft. The company aims to produce 1,000 nozzles through powder bed fusion technologies in 2015, and 40,000 annually by 2020. The nozzle is redesigned to reduce the number of individual parts from 20 to 1, this further reduces the number of brazes and welds that would have been necessary using traditional methods.

Figure II.5 3-D printing jet engine fuel nozzles by GE

Case studies in medical and dental area have been reported in which powder bed fusion would benefit the design and manufacturing phase because of the unique and complex geometries involved. Currently, additive manufacturing makes up a $780 million per year submarket within the dental industry. The technology is used for the fabrication of crowns, bridges, dental models, and even clear aligners [5].

2.1. Product quality, processing rate and cost for metal powder bed fusion technology

Metal powder bed fusion processes fuse particles via three basic consolidation mechanisms: solid-state sintering, liquid phase sintering, and full melting [6].

In solid-state sintering processes, atoms in powder particles diffuse across the boundaries to form necks between adjacent particles and eventually creating one solid piece. This process operates at a temperature much lower than the melting point of the material. Solid-state sintering applies to a wide variety of materials, especially pure metals. However, it requires long interaction time with a low-power energy source for particles to be consolidated. As a result, it became less favorable mechanism for the application of additive manufacturing.

Liquid phase sintering usually applies alloys and composites over a range of temperatures [7]. Packed particles are heated approaching the melting temperature, accelerating the diffusion between particles and forming a liquid during the sintering process. The liquid will in turn wet the solid, providing a capillary force to pull together the solid grains which further increases diffusion rates. Thus, liquid phase sintering process is several orders magnitude faster than solid-state sintering process.

In full melting processes, materials are heated to fully molten state. Near full dense objects can be produced with good mechanical properties. Due to high energy input, the process suffers from fluid behavior instability, and therefore requires careful monitoring of the processing parameters. Most industrial powder bed fusion machines are adopting full melting mechanism to satisfy the needs of high density, fine quality functional parts. Therefore, in the following sections, discussion on product quality, processing rate, energy consumption and cost will focus on full melting of metal materials.

2.1.1. Product quality

A variety of factors contributes to the product quality (geometric, mechanical) of metal powder bed fusion processes, including material properties, operating parameters, printing strategy, etc. These factors are also correlated with each other.

Material property

Extensive researches have been carried out to study and develop new materials for metal powder bed fusion. The powder material undergoes rapid heating and cooling to fuse into a solid piece. The nature of powder bed fusion technology makes the process sensitive to the properties of powder particles used in the process.

Powder metallurgy has been studied for decades, the powder fabrication approach influences the size, shape, microstructure, chemistry and cost, etc. [8] The specific material properties

determine the method to produce the corresponding powders. The four main categories of fabrication methods are mechanical, chemical, electrolytic and atomization. Powders fabricated by mechanical techniques, i.e. machining, milling, grinding, etc., are usually coarse with irregular shape and suffering from contamination. Mechanical techniques are suitable for brittle materials, and therefore not useful for most metals because of their ductility. Electrolytic fabrication is mostly used for high purity elemental materials. The powders fabricated usually have irregular porous structure with poor packing characteristics. Chemical reaction techniques can be used to fabricate almost all metals. Powders can be formed by gas-solid, liquid, or vapor phase reactions depending on the properties of material oxalates and formates. It is, however, rather difficult to control the size and shapes of the powders. Atomization techniques have developed to provide the majority of all powders over the past forty years [8]. During atomization, powders are formed from molten metal using a spray of droplets. The method is applicable to produce both elemental and pre-alloyed powders. Because of the reliability and flexibility in controlling the shape characteristics of the powders, atomization becomes favorable for technologies that have high requirements in such aspects. Three major types of atomization methods are commonly used in industry: liquid atomization, gas atomization and centrifugal atomization.

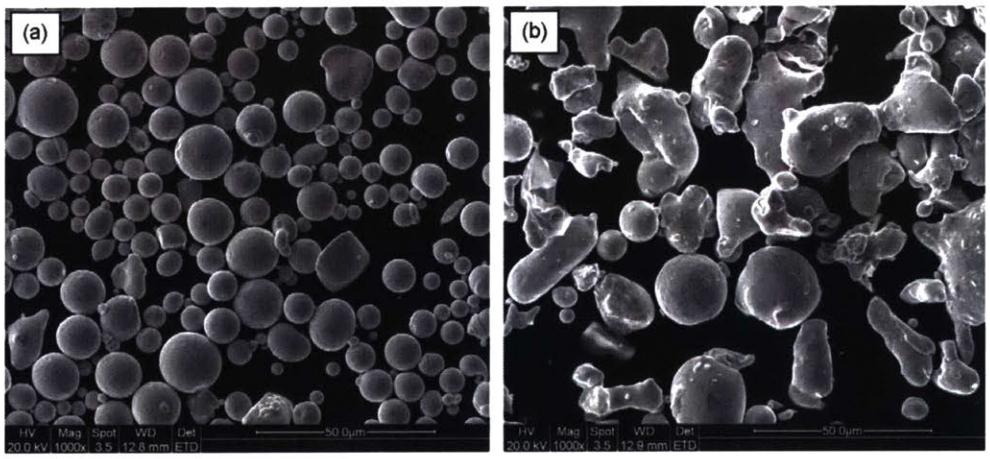

Figure II.6 SEM images showing characteristic morphologies of stainless steel powder: (a) gas atomization; (b) water atomization. [9]

Material used in powder bed fusion process are usually made from atomization because of the high requirements on powder properties. Both water atomized powders and gas atomized powders have been extensively tested. Powders fabricated through gas atomization technique are close to spherical shape, while water atomized particles have irregular shapes as shown in Figure II.6. Li et al. studied the density of laser melted tracks using powders fabricated with both gas atomization and water atomization techniques. The water atomized powders have a higher oxygen content, which limits its wetting ability during melting process. In addition, the irregular shape leads to a lower packing density. As a result, the water atomized powders produced less denser structure than air atomized powders [9], [10]. Metal powders fabricated using air atomization are preferred in powder bed fusion processes. The commercial metal material provided by EOS in the market are summarized in Table II.1.

Material Name	Ultimate Tensile Strength Min (MPa)	Ultimate Tensile Strength Max (MPa)	Tensile Modulus Max (MPa)	Elongation at Break Min (%)	Elongation at Break Max (%)	Part Density (g/cm3)
EOS Aluminum AlSi10Mg	440	480	85000	4	11	2.67
EOS CobaltChrome MP1	1050	1450		8	28	8.3
EOS CobaltChrome SP2	1350	1350	200000	3	3	8.5
EOS DirectMetal 20	400	400	80000			6.3
EOS Maraging Steel MS1	1000	1200	185	6	14	8
EOS NickelAlloy HX	680	890	215000	21	47	8.2
EOS NickelAlloy IN625	850	1040	190000	30	47	8.4
EOS NickelAlloy IN718	930	1100	180000	22	36	8.15
EOS StainlessSteel 316L	485	690	185000	25	70	7.9
EOS StainlessSteel GP1	850	1100	200000	25	40	7.8
EOS StainlessSteel PH1	1000	1200		12	21	7.8
EOS Titanium Ti64	1150	1280	120000	8	14	4.41
EOS Titanium Ti64ELI	1200	1300	128000	4	11	4.41
EOS Titanium TiCP	445	465	105000	18	12	4.5

Table II.2 Commercial metal material from EOS GmbH

The size distribution of metal powder is also important to the product quality of the powder bed fusion process. Spierings et al. 2011 studied the influence of size distribution of stainless steel (316L) powders on the product mechanical properties and surface quality [11]. Powders with three different particle size distribution were examined as shown in Figure II.7. Powder type 1 and 2 are characterized by a Gaussian like particle size distribution. Type 3 has an asymmetric distribution with an increased concentration of finer particles. The midpoint particle size of the tested powders grows from type 1 material to type 3. With the same processing parameters, finer particle granulation generally leads to better surface quality than coarser material as can be seen in Figure II.8. The surface quality, however, depends greatly on processing parameters such as layer thickness, scanning velocity and hatching distance. Spierings et al. 2011 found that high mechanical strength is reached for fine powders because they can be easily melted to achieve high density parts. They also suggested that large size particles are beneficial for higher breaking elongations.

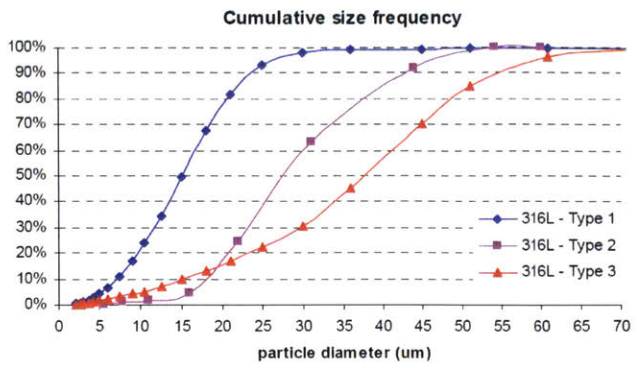

Figure II.7 Cumulative size frequencies of powder type 1, 2 and 3 [11]

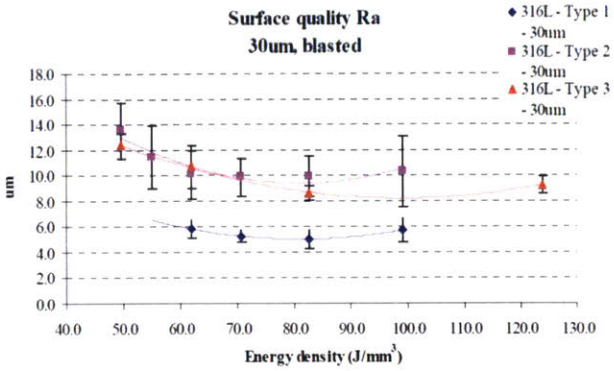

Figure II.8 Blasted scan surface quality for 30 µm layer thicknesses [11]

Processing parameters

To successfully produce a high quality part, a set of strictly selected processing parameters are required depending on the material to be processed. These parameters include laser power, scanning velocity, layer thickness, hatching distance, etc. The parameters are usually preset and embedded in the software developed for the powder bed fusion machines, and this allows the companies to sell their own powders at a higher price.

Layer thickness is correlated with the particle size and distribution of the powder material. Layer thickness determines the movement of the building platform. After scanning each layer, the platform will be lowered by the distance of a preset thickness value. Spierings et al. suggests that the layer thickness is at least 50% higher than the diameter of 90% of powders to ensure most powders can be deposited with the layer thickness setting [11]. Because of the apparent density of the powder layer and shrinkage during the fusion process, the real layer thickness is slightly higher than the preset values. The larger the apparent density is, the smaller the layer thickness deviation. Layer thickness would affect the decision on other parameters. Badrossamay et al. reported that relative density of built blocks from 316L stainless steel is independent of layer thickness at sufficient low scanning velocity as shown in Figure II.9 [12] .

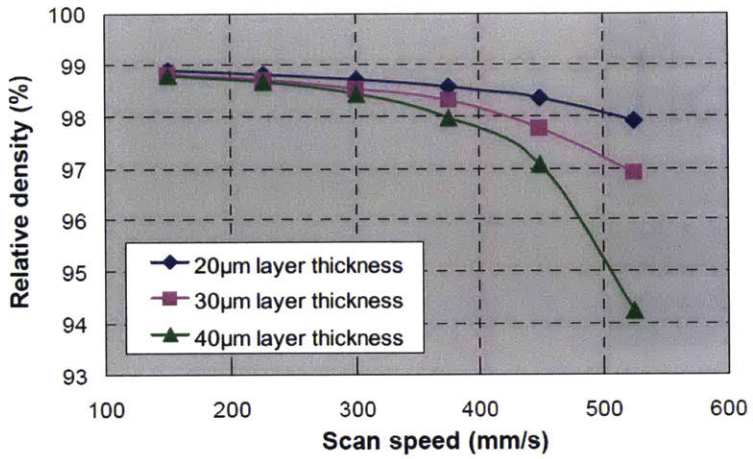

Figure II.9 Effect of scan speed on the relative density for 316 L stainless steel (16.6 μm midpoint particle size) processed on Concept Laser M3 Linear (100 W) [12]

Laser power and scanning velocity determine the processing window for a material. Laser power is the total power output of the laser unit onto the powder bed material, whereas the laser beam energy density profile is often close to a Gaussian distribution. The beam is directed by a galvanometer mirror, and characterizes the speed of laser beam moves across the powder bed. The two parameters together determine the energy incident within the laser focus diameter. In order to fully melt the material, intensive energy is to be focused to a very small-size area. For example, 3 J/mm^2 is needed within 0.5 mm^2 area to fully melt the ferrous powder inside [13]. The parameters vary with different material due to their heat capacity, latent heat of fusion, melting temperature, thermal conductivity, laser energy absorptivity, etc. This will be discussed in depth in Chapter 4.

Single tracks of melted material are usually formed to study and determine the processing window for laser power and scanning velocity. Laohaprapanon et al. determined the processing window for 316L stainless steel powder particles with average particle size of 36.6 μm as shown in Figure II.10 [14]. Typically, higher scanning speed requires higher laser power output to ensure the energy input into the material. When scanning velocity is too fast, unmelt tracks would occur because of insufficient energy. Meanwhile, when laser power is too high, balling phenomenon as well as evaporation would occur. To form a smooth melted track, the two parameters need to be carefully restricted.

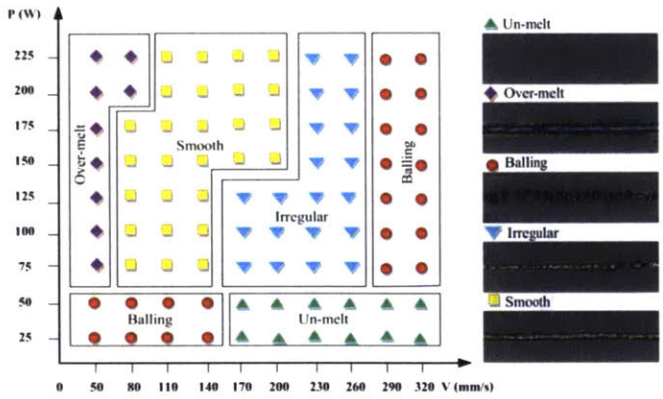

Figure II.10 Effect of laser power and scan speed on substrate of line scanning [14]

Badrossamay et al. studied the relative density, surface quality dependence on the processing parameters [12]. Their results show that for the same power settings, the relative density of the built cubes decreases significantly when layer thickness increases at high scanning velocity range. In addition, the scanning velocity range is wider for the higher power machine as can be concluded from Figure II.11 and Figure II.12. Surface roughness is not closely correlated with scanning velocity within the speed range while full melting is achieved. It would increase when scanning velocity further increases and becomes too high to ensure full melting of the powders.

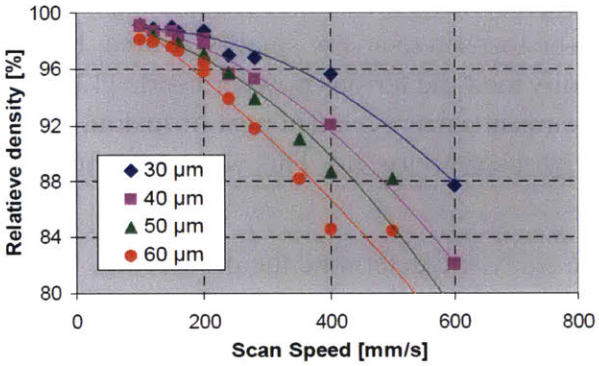

Figure II.11 Effect of scan speed and layer thickness on the relative density for maraging steel 300 at different layer thickness (16.6 µm midpoint particle size) processed on Concept Laser M3 Linear (100 W) [12]

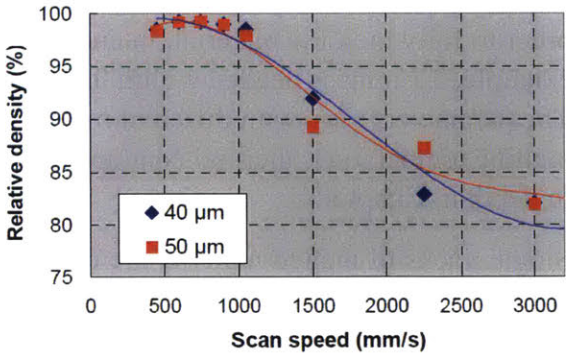

Figure II.12 Effect of scan speed and layer thickness on the relative density for maraging steel 300 at different layer thickness (16.6 µm midpoint particle size) processed on EOSINT M270 (200 W) [12]

The hatching distance is the distance between the centerlines of two adjacent scans. Depending on the size of the melt pool, the hatching distance is usually smaller than the laser spot diameter to ensure overlap between adjacent tracks. When the melt pool size is similar to the laser spot diameter, the relative density of the printed parts is almost independent of the hatching distance as shown in Figure II.13 [12]. However, when the melt pool size is smaller than the laser spot diameter for higher layer thickness, the relative density would decrease sharply with the

increasing hatching distance. Generally, scan spacing (hatching distance) needs to be similar to the melt pool size to achieve the optimum surface quality.

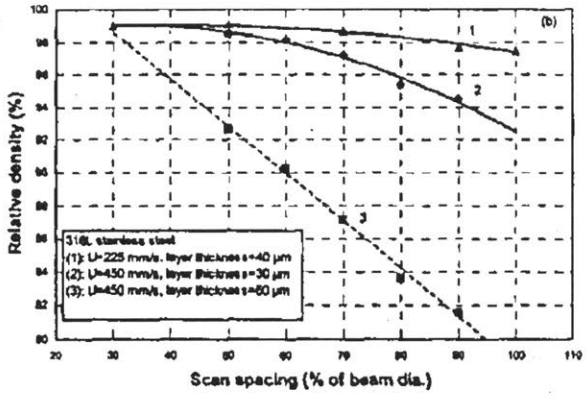

Figure II.13 Effect of relative density on scan spacing of 316L stainless steel material (16.6 μm midpoint particle size) processed on Concept Laser M3 Linear (100 W), hatching distance as a percentage of beam diameter [12]

2.1.2. Processing rate

Researchers have been dedicated to improving the processing rate of powder bed fusion processes over the past decade. With deeper understanding of the process physics as well as advances in laser technology, the processing rate have been improved by an order of magnitude for full melting of powder material. The processing rate for different metal materials, including steel, titanium alloy, aluminum, etc., are limited in the range of 0.5 to 3.5 mm^3/s around the year of 2000 [15], by which time the lasers equipped in powder bed fusion machines had no greater power than 330 W. In a typical process, the processing rate is directly proportional to the product of scanning velocity, layer thickness and laser beam diameter.

Schleifenbaum et al. reported the results of applying a higher power laser (600 W) in selective laser melting [15]. In their study, high relative density could be achieved at high layer thickness (250 μm) and beam diameter (1.05 mm) with the high power settings. To keep geometric accuracy and surface quality, a skin-core scanning strategy is developed as shown in Figure II.14. The core of the part is printed with higher layer thickness and larger beam diameter, while the skin is printed with fine settings. With this strategy, the processing rate reaches a maximum of 20 mm^3/s while maintaining high density (> 99%).

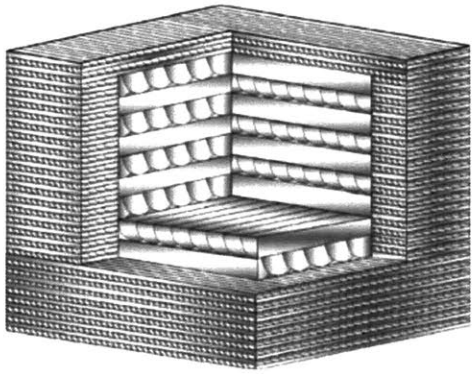

Figure II.14 Schematic representation of the skin core principle [15]

Buchbinder et al. studied the effect of applying high power laser to fuse aluminum alloy powders (AlSi10Mg) [16]. With the same layer thickness and laser diameter settings, high relative density could be reached at higher scanning velocity at higher laser power as shown in Figure II.15. The scanning velocity at 1000 W can reach approximately 2200 mm/s compared to 500 mm/s at 300 W. The high scanning velocity leads to an increase in the processing rate from 4 mm^3/s to 16 mm^3/s. Further studies demonstrate that hardness of printed specimens is not influenced by the high power, high scanning velocity settings.

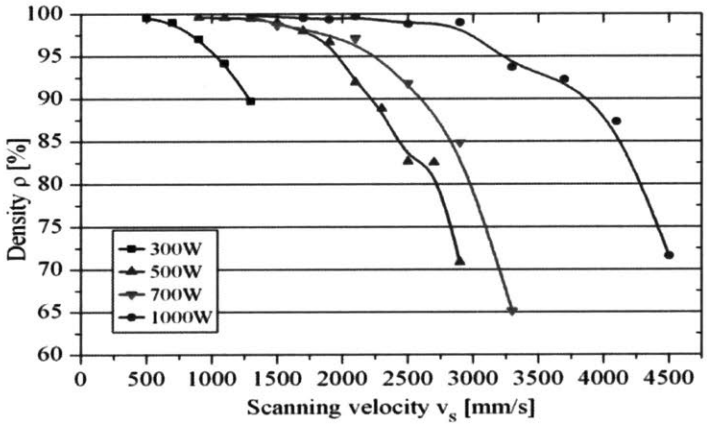

Figure II.15 Density depending on scanning velocity and laser power with layer thickness 50 μm, laser beam diameter 150 μm [16]

In general, parameter settings with high scanning velocity, hatching distance and layer thickness are enabled with the application of high power laser. The combined factors largely increase the processing rate of powder bed fusion. However, the process suffers from evaporation and melt pool instability at high power settings. Detailed discussion will be presented in Chapter 4.

2.1.3. Cost

When comparing costs of producing a same part with additive manufacturing and conventional manufacturing, there are several aspects to be considered; some are directly related to manufacturing phase while others concern the overall process chain. For additive manufacturing,

machine cost, labor cost and material cost are major direct factors affecting product cost in manufacturing phase [17].

A typical metal laser sintering/melting machine itself is around 500,000 dollars. In addition, ancillary equipment are needed before it can fully function, including nitrogen generation equipment, power converter, etc. Maintenance cost should also be considered within this part.

In additive manufacturing, material comes in different form (powder, liquid, fiber, etc.). In the manufacturing process, it contains material that ends up in the final product and wasted material. Most printed products contain support structures and loose material in the building process. Support structures can be easily categorized as waste material, however, depending on different scenario, loose material may or may not be reused in the same manufacturing cycle. Some material (reactive powders for example) needs to be stored in special environment, this will also add to the cost in material section.

When considering labor cost for additive manufacturing, job set-up, process inspection, post machining should be treated differently. It requires different knowledge and skills to operate the machine and to post machine green products. Estimation for labor cost may be very different for these two jobs. Process inspection usually takes minimal time and can often be neglected when compared to some conventional manufacturing methods.

As an illustrative example, cost analysis is performed on a research reported case on energy study of paintball gun holders by Telenko et al [18]. The part is made of Duraform PA material. It weighs 35 grams per half and fits within a box of 3.2 cm by 2.54 cm by 12.7cm. To achieve maximum build efficiency, it is assumed that 300 halves are printed per building job.

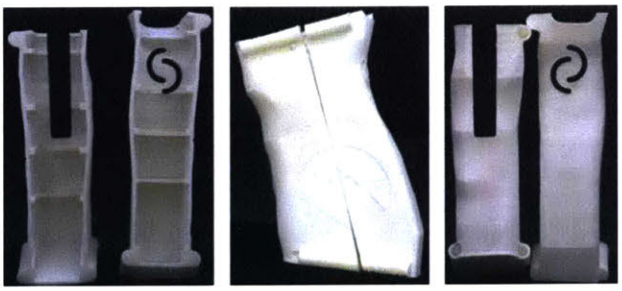

Figure II.16 Paintball gun holder [19]

The total required electricity is calculated from the electricity intensity requirement per kg material (130 MJ/kg) reported by Telenko et al [18]. Electricity cost is taken from reports on average industrial electricity cost in the United States from EIA. All the direct costs are summarized in Table II.3 below.

Manufacturing cost	**Value**	**Assumptions**
Number of parts per machine	300	
Platform build time [hr]	15	(13 hrs of build + 2 hrs warm-up)
Time consumed per part [hr]	0.05	
Electricity Costs		

Total electricity consumed [kWh]	53	
Electricity cost [$/kWh]	0.06	
Electricity cost per part [$]	0.02	
Labor costs		
Machine operator cost per hour Set-up time to control machine [$]	20	Hopkinson et al. 2003 [17]
Post machining cost per hour [$]	20	Hopkinson et al. 2003 [17]
Set-up time per build [hr]	2	Hopkinson et al. 2003 [17]
Post-processing time per build [hr]	6	Hopkinson et al. 2003 [17]
Labor cost per build [$]	160	
Labor cost per part [$]	0.53	
Material costs		
Material per part including support [kg]	0.040	(assuming 15% support)
Loose material per build (if not reused) [kg]	0	
Storage cost per kg [$]	0	
Material cost per kg [$]	130	(assumed Duraform PA)
Material cost per part [$]	5.23	
Total cost per part [$]	5.79	

Table II.3 Cost calculation in the direct manufacturing phase

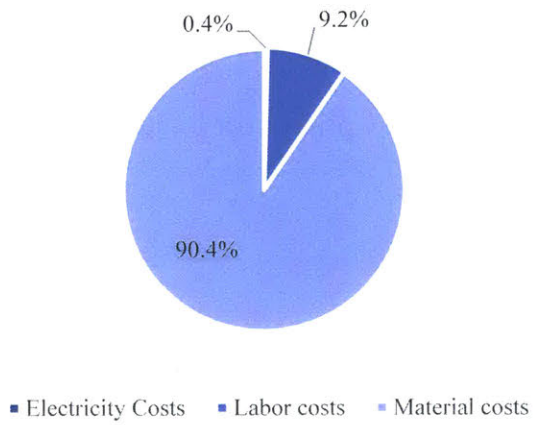

Figure II.17 Cost break down in the direct manufacturing phase

When plotted in a pie chart, it is obvious that material cost dominates the direct manufacturing phase of powder bed fusion process contributing to 90% of the total. On the other hand, electricity cost is negligible.

According to Senvol LLC, in order for products made with additive manufacturing to have cost advantage over the same parts made with conventional method, it must present one or several of the following aspects: low production volume, special feature (conformal cooling channel, lattice structure, hollow structure, etc.), short lead/developing time, high material cost, high fly-to-buy ratio, etc.

When taking indirectly related cost into consideration, machine costs, production overhead and administrative overhead should then be included to calculate the cost. These factors are also included when an additive manufacturing service company quotes its service. All the costs are summarized in Table II.4 below.

Cost factors	Value	Assumptions
Number of parts per machine	300	
Platform build time	15	(13 hrs of build + 2 hrs warm-up)
Time consumed per part [hr]	0	
Electricity		
Total electricity consumed [kWh]	53	
Electricity cost [$/kWh]	0.12	
Electricity cost per part [$]	0.02	
Labor costs		
Machine operator cost per hour Set-up time to control machine [$]	20	Hopkinson et al. 2003 [17]
Post machining cost per hour [$]	20	Hopkinson et al. 2003 [17]
Set-up time per build [hr]	2	Hopkinson et al. 2003 [17]
Post-processing time per build [hr]	6	Hopkinson et al. 2003 [17]
Labor cost per build [$]	160	
Labor cost per part [$]	0.53	
Material costs		
Material per part including support [kg]	0.04	(assuming 15% support)
Loose material per build (if not reused) [kg]	0	
Storage cost per kg [$]	0	
Material cost per kg [$]	130	(assumed Duraform PA)
Material cost per part [$]	5.23	
Equipment costs		
Machine costs [$]	245,000	3DSystems Sinterstation HIQ+HS
Equipment depreciation [$]	245,000	10 years
Maintenance cost [$]	48,500	
Software cost [$]	0	included in machine purchase
Machine operation time per year [hr]	4,016	Two shifts working days
Equipment cost per part [$]	3.65	
Production overhead		
Rent for facility and area per hour [$]	5.2	Baumers et al. 2011 [19]
Cost for light, AC, heat per hour [$]	0	included in facility rent
Non-manufacturing related labor cost [$]	0	Not accounted
Production overhead cost per part [$]	0.26	
Administrative overhead		

Hardware cost/year [$]	190	Baumers et al. 2011 [19]
Software cost/year [$]	190	Baumers et al. 2011 [19]
Consumables cost/year [$]	1270	
Administrative labor cost [$]	0	Not accounted
Administrative overhead cost per part [$]	0.02	
Total cost per part	9.72	

Table II.4 Cost break down in the whole manufacturing phase

In the whole manufacturing process, material costs still dominate at 54% of the total cost as shown in Figure II.18. Equipment cost shows to be the second largest cost at 38%. If the machine operation time is 4016 hours per year (five days per week, two shifts), equipment costs would be 3.65 dollars per part, which shows up to 38% in the figure. However, when the machine operation time is 7884 hours per year (which is 328 days three shifts), the equipment cost is reduced to 1.85 dollars per part. Equipment cost per part is sensitive to operation time. As a result, to keep equipment cost per part down, the machine operation time should be utilized to its maximum.

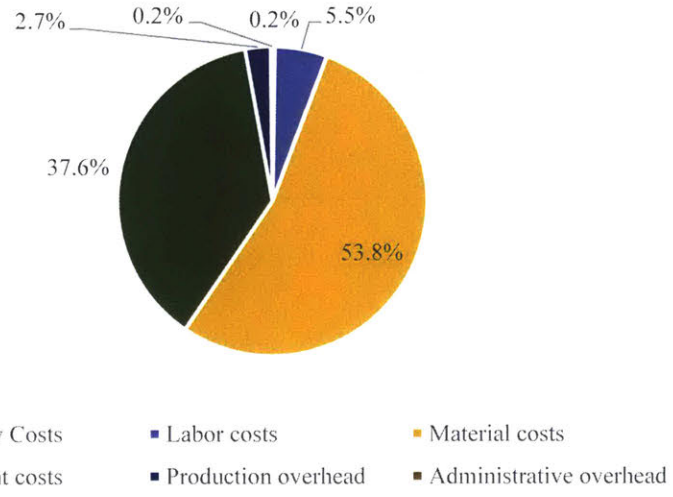

Figure II.18 Cost break down in the whole manufacturing phase

For manufacturers, to utilize maximum operating efficiency (patch density/part per build), reduce support material/structure, find lightweight solutions and operate the machine to its maximum allowable time are the four major methods to reduce cost given the current standing of technology and material market. In the future, if material cost comes down significantly (from 130$/kg), good design as well as build/patch planning will be more significant in further reducing cost.

Section costs	**Possible improvement options**
Electricity Costs	
	improve energy efficiency per kg material processed
Labor costs	
Set-up time per build	improve software, experienced engineer

Post-processing time per build	improve post-processing technics, redesign for easier post-processing
Material costs	
Material per part including support	light weight design, reduce support material, recertify and reuse loose material
Material cost per kg	market
Equipment costs	
Machine costs	market
Machine operation time per year	increase machine operation time, utilize build efficiency

Table II.5 Possible improvement on cost of additive manufacturing

III. Processing Rate Modeling for Material Extrusion

In material extrusion process, material is heated and dispensed through a nozzle/orifice. The processing rate for material extrusion deviates to two extremes for two different popular technologies in this category: fused deposition modeling (FDM) and big area additive manufacturing BAAM. FDM was developed by Stratasys, and BAAM was developed through collaboration between Oak Ridge National Laboratory and Cincinnati Inc. In both systems, material in filament/pellet form is first driven through a heating zone within which they reach desired temperature. Heat transfer in the heating zone can be crucial to the processing rate. In this chapter, two heat transfer models will be used to study the effect of heat transfer on processing rate for these two technologies respectively.

1. Heat transfer modeling

In this section, heat transfer models are developed to explore potential rate limits of material extrusion process.

1.1. Heat transfer modeling for Stratasys FDM machine

The Stratasys FDM machines are divided in three categories: idea series, design series and production series. The idea series features desktop machines with small build volume capacity and relatively low resolution. The design series and production series are designed to fit the needs of bigger build volume and high quality part. All the machines in different categories have similar extrusion apparatus. The extrusion head includes drive mechanism, liquefiers and dispensing nozzles as can be seen in Figure III.1 and Figure III.2.

The drive mechanism, often powered by dc motors, engages with prefabricated filament strand, drives the engaged filament into the liquefier, and eventually extrudes the molten material. Resistance heating is applied in the liquefier to heat the filament material to temperature with good flowability. For ABS material, the set temperature at the wall of the heating zone (liquefier) goes up to 280 °C. The molten material is then deposited through the nozzle onto a build platform. As the dispensed material cools down, it solidifies and bonds with surrounding material, internal stress can occur because of shrinkage. The build chamber is heated to just below glass transition temperature to relive the stress, as a result good accuracy part can be produced. For ABS material, the chamber is often heated to between 70 °C and 90 °C.

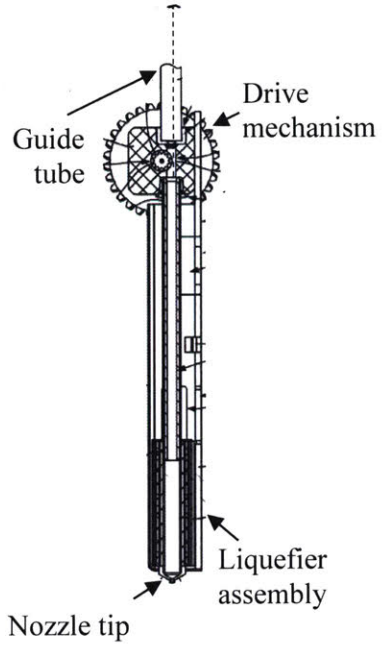

Figure III.1 1 Extrusion apparatus in Mojo machine [20]

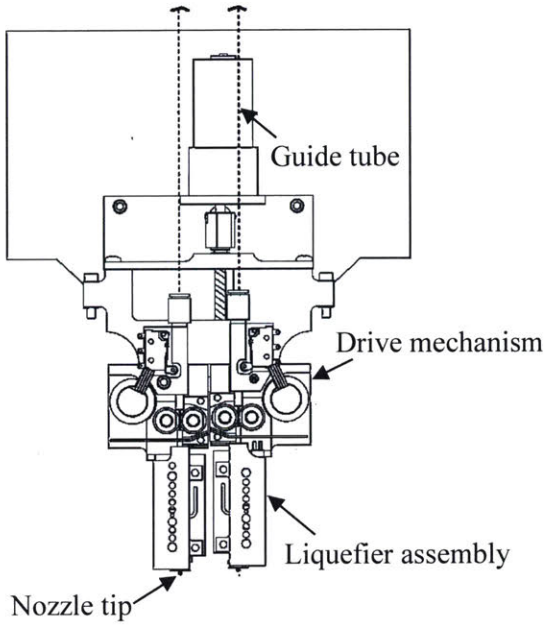

Figure III.2 Extrusion apparatus in Fortus machine [21]

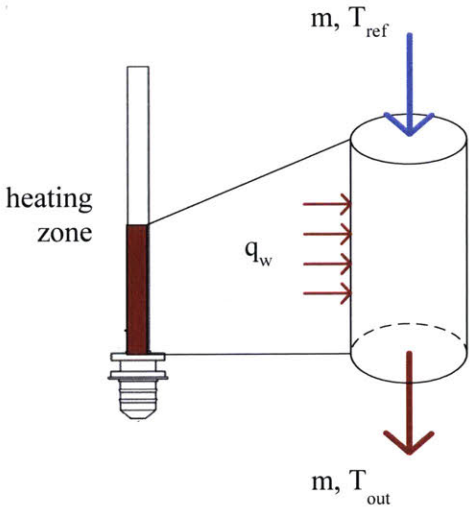

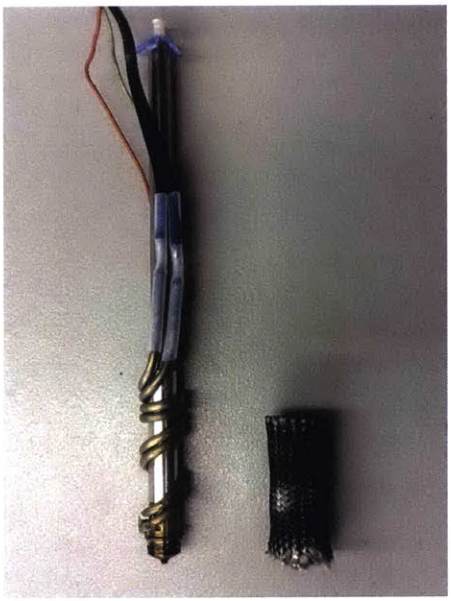

Figure III.3 Print head nozzle used in Mojo system [20]

The filament goes through a cylindrical liquefier, within which heat is applied at the wall as shown in Figure III.3. An insulator covers the heating zone to prevent heat loss to the surrounding as well as to protect other units inside the extrude head. The filament has a diameter of 1.78 mm. Material at the inlet is assumed to have uniform initial temperature at 20 °C. The filament remains rigid before it reaches glass transition temperature, above which it could be

treated as shear thinning material for which the dynamic viscosity dropping with increasing shear rate [22].

Assuming steady state is reached inside the liquefier, heat transfer within the heating zone could therefore be described with an energy balance equation as shown with energy balance equation 3.3 below, in which ρ is the density of ABS material, C_p is the heat capacity, u is the feeding speed of filament, k is the thermal conductivity, and $\mu\Phi$ denotes viscous heat dissipation.

$$\rho C_p u \frac{\partial T}{\partial z} = k\nabla^2 T + \mu\phi = k\left(\frac{\partial^2 T}{\partial r^2} + \frac{1}{r}\frac{\partial T}{\partial r} + \frac{\partial^2 T}{\partial z^2}\right) + \mu\phi \quad \text{Eq. 3.3}$$

In order to determine the importance of viscous heating in the liquefier, the Brinkman number (equation 3.4) is calculated for material entering glass transition phase. In the equation, T_w is the temperature of the wall, and T_g is the surface temperature of the feeding filament surrounded by molten material. With the parameters for ABS material listed in Table III.1, the Brinkman number is calculated to be smaller than 0.007. As a result, viscous heating is negligible compared to conductive heat transfer from the wall. The heat transfer equation could therefore be further simplified into equation 3.5.

$$Br = \frac{u^2 \mu}{k\left(T_w - T_g\right)} \quad \text{Eq. 3.4}$$

$$\rho C_p u \frac{\partial T}{\partial z} = k\left(\frac{\partial^2 T}{\partial r^2} + \frac{1}{r}\frac{\partial T}{\partial r} + \frac{\partial^2 T}{\partial z^2}\right) \quad \text{Eq. 3. 5}$$

Parameter	Value	Reference
Heat capacity C_p [J/(kg-K)]	2080	[23]
Thermal conductivity k [W/(m-K)]	0.18	[24]
Dynamic viscosity μ [Pa-s]	155 to 1550	[23]
Density [kg/m^3]	1050	[23]
Liquefier length L [mm]	20	
Filament diameter [mm]	1.78	
Inlet temperature [°C]	20	
Wall temperature [°C]	260	

Table III.1 Parameters used in heat transfer modeling for FDM machine

The model then decribes a forced flow inside a isothermal pipe with uniform initial temperature, for which the bulk temperature at the exit could be determined by equation 3.6 below. Here we neglect the effect at the outlet where liquefier narrows down to a smaller diameter nozzle. The heat transfer coefficient could be determined from the Nusselt number (or Biot number in the case where heat transfer within solid body is concerned) as illustrated in equation 3.7 [24]. Both Nusselt number and Biot number characterises the ratio of heat transfer at the surface to the heat

transfer within the fluid/solid body. Nusselt number is 3.657 for fully developed flow and slightly larger in the developing region.

$$\frac{T_b - T_{ref}}{T_w - T_{ref}} = 1 - e^{-\frac{\bar{h}}{\rho u C_p}\frac{4L}{D}} \quad \text{Eq. 3.6}$$

$$\bar{h} = \frac{\overline{Nu} \times k}{D};\ \overline{Nu} = 3.657 \quad \text{Eq. 3.7}$$

C_p - heat capacity
T_{ref} - temperature at the inlet
T_b - bulk (average) temperature at the exit
T_w - temperature on the wall at the exit
k - thermal conductivity
D - diameter of the filament
L - length of the heating zone (liquefier)
u - flow velocity
h - heat transfer coefficient

For average exit temperature of 229 °C as measured by Go et al. 2017 [25], the feeding velocity of the filament is calculated to be 3.8 mm/s, leading to a build rate of 33.6 cm^3/hr. Figure III.4 below shows the bulk temperature of the filament along the length of liquefier at different filament feeding rate. The bulk temperature of the filament approaches the wall temperature as the material travels along the liquefier. At higher build rate (i.e. higher filament feed velocity), the bulk temperature of the filament at the exit (0.02 m) would be lower due to less heating time within the liquefier. The build rate for a desired exit bulk temperature could be determined by equation 3.8 with the flow velocity derived from equation 3.6 and 3.7. Note that the build rate is independent of the diameter of filament, but proportional to the length of the liquefier. Equation 3.8 suggests the possible solutions for a higher build rate with the current apparatus are: increase the length of the liquefier (heating zone), increase the average temperature of the filament before it enters the liquefier, and use material with lower heat capacity.

$$\dot{m} = \rho\frac{\pi D^2}{4}u = \rho\frac{\pi D^2}{4} \times \left(\frac{-\frac{\bar{h}}{\rho C_p}\frac{4L}{D}}{\ln(1 - \frac{T_b - T_{ref}}{T_w - T_{ref}})} \right) = \rho\frac{\pi D^2}{4} \times \left(\frac{-\frac{\overline{Nu} \times k}{D}\frac{4L}{D}}{\rho C_p \ln(1 - \frac{T_b - T_{ref}}{T_w - T_{ref}})} \right) \quad \text{Eq. 3.8}$$

$$= \frac{\pi \overline{Nu} \times kL}{\ln(\frac{T_w - T_{ref}}{T_w - T_b})C_p} = Coeff_{FDM}(T^*)\rho\alpha L$$

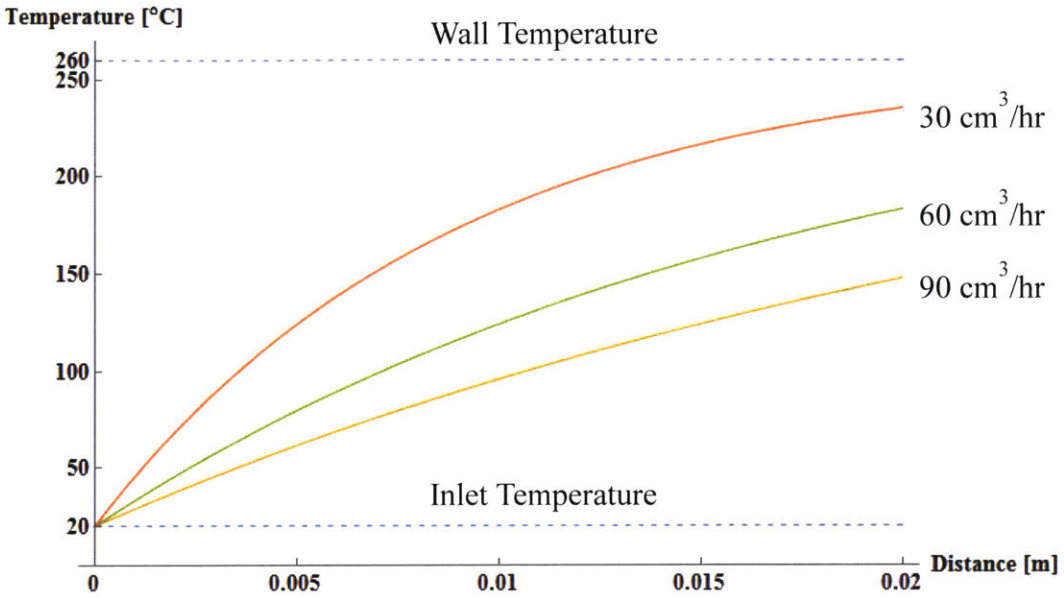

Figure III.4 Bulk temperature profile along the length of liquefier for different build rate

Manufacturer	Model	Material	Measured processing rate [cm³/h]	Ratio of measured rate to theoretical rate	Reference
Stratasys	Dimension Elite	ABS (ABSplus)	11.1	33%	Corman 2014 [3]
Stratasys	Fortus 360 MC	ABS M30	17.6	52%	Corman 2014 [3]
Stratasys	Mojo	ABS	16.2	48%	Corman 2014 [3]
Stratasys	Fortus 400 MC	ABS M30	20.9	62%	EPRI 2014 [26]
Stratasys	Fortus 900 MC	ABS M30	20.9	62%	EPRI 2014 [26]

Table III.2 Measured processing rate for FDM processes with ABS material

Corman 2014 studied the processing rate and energy consumption for three different FDM machines from Stratasys [3]. In all measurements, a NIST testing part with overall dimension of 100mm×100mm×17mm is built as shown in Figure III.5 below. The processing rate is calculated from the measurement of printed material volume and the build time. Note that, during the printing process, soluble support material was printed to enable special geometries (e.g. overhangs) as well as bonding the test part to the building substrate. Although only the volume of major printing material (~100 cm^3) is counted for the build rate, the printing time includes

dispensing support material (5 to 10 cm^3). As a result, the calculated build rate could be slightly underestimated. When compared to the theoretical extrusion rate, the rate ratio shows up from 33% to 52%. Marek Samotyj from Electric Power Research Institute, Inc. reported two cases in which they also printed the NIST testing part with Fortus 400 MC and Fortus 900 MC machines [26]. The rate ratio is at 62%.

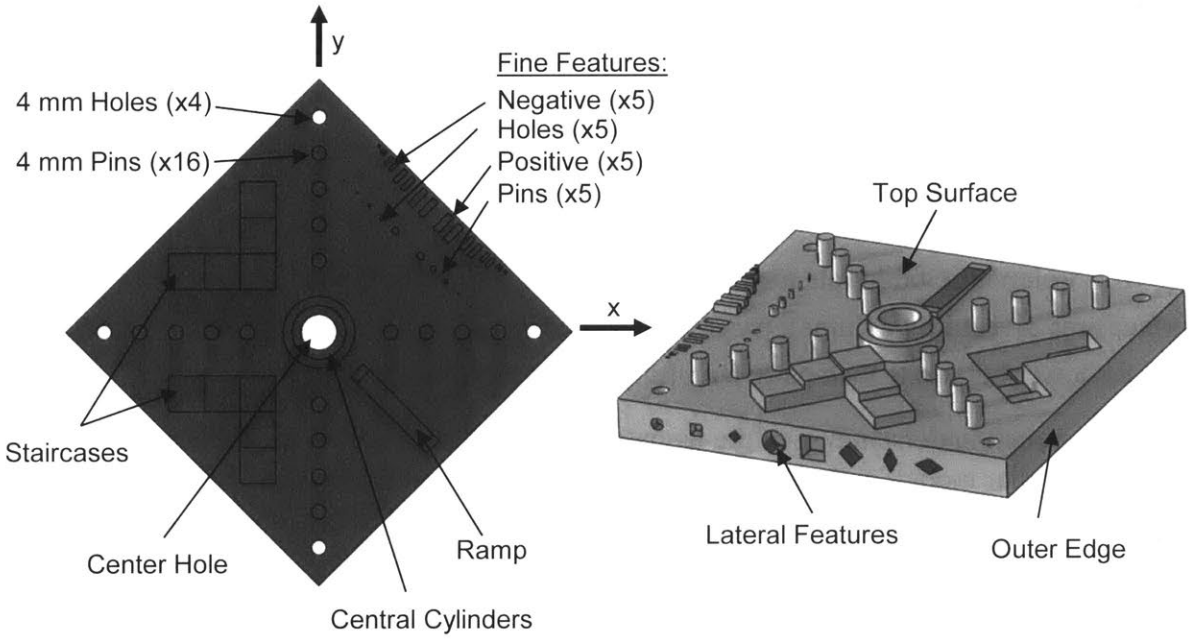

Figure III.5 NIST AM test part [3]

Neglecting heat loss from the liquefier to the surrounding, most of the energy is utilized to heat up the filament material such that it could reach desired average temperature before exiting the nozzle. The energy usage from liquefier heating would be very efficient. The rate ratio is low at 33 to 62% because of other constraints from the system. Go measured the processing rate for building rigid and hollow structures, and discovered that with the same parameter setting, the processing rate could vary by an order of 3 as shown in Figure III.6 [25]. To further quantify the effect of the overall printing strategy and constraints from mechanical system, Go performed experiments on a Mojo machine to measure the processing rate at fixed filament feeding velocity. It is found that for printing the perimeter of an object, the build rate is 11.5 cm^3/hr with filament feeding velocity of 2.4 mm/s; for filling material within the perimeter, the build rate is 20.9 cm^3/hr with filament velocity of 4.4 mm/s. The build rate for printing perimeter is slower to ensure required printing resolution. For 1.78 mm diameter filament, a constant feeding velocity of 4.4 mm/s would lead to a build rate of 39.4 cm^3/hr. The measured build rate is 53% of this constant feeding build rate in comparison. The result shows that the current build rate is restricted by the mechanical design (performance of the motion system) and printing strategy (resolution, precision, accuracy), the overall build rate for a part would be roughly half of the material extrusion rate (continuously extruding material at the nozzle). Theoretical maximum build rate is, however, determined by the heat transfer boundaries.

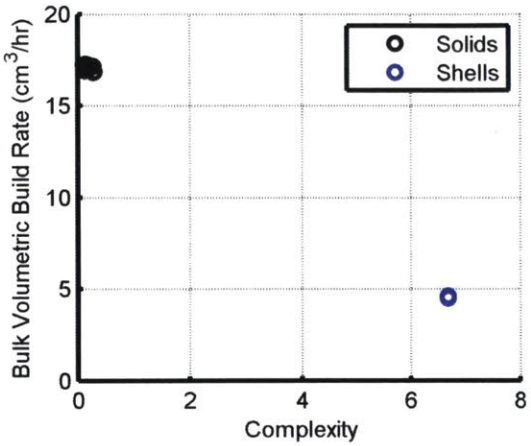

Figure III.6 Volumetric build rate measured for parts of varying complexity (complexity defined as surface area divided by volume); parts with greater surface area relative to volume (shells) have much lower build rate than parts with fully solid geometries [25]

To have a thorough understanding of the temperature distribution within the liquefier, Go 2017 developed a similar model, with which they studied pressure and temperature of the molten material inside the liquefier over a range of input filament feed rates including the scenario where the melt is not fully thermally developed before the nozzle [25]. With the same governing equation, they applied finite element analysis to determine the temperature profile at different build rate, as shown in Figure III.7. Their results shows that at slow feed rate of 30 cm^3/hr, the material at the centerline down the liquefier is heated up close to the wall temperature 260 °C. At the feed rate of 90 cm^3/hr, however, the centerline temperature is below glass transition point which will cause the rigid unmolten filament to jam at the nozzle. To reach experimentally observed average (bulk) exit temperature of 229 °C, their simulation showed that the feed rate is bounded to be under 40 cm^3/hr, which is slightly larger than the analytic results of the simplified model (33.6 cm^3/hr).

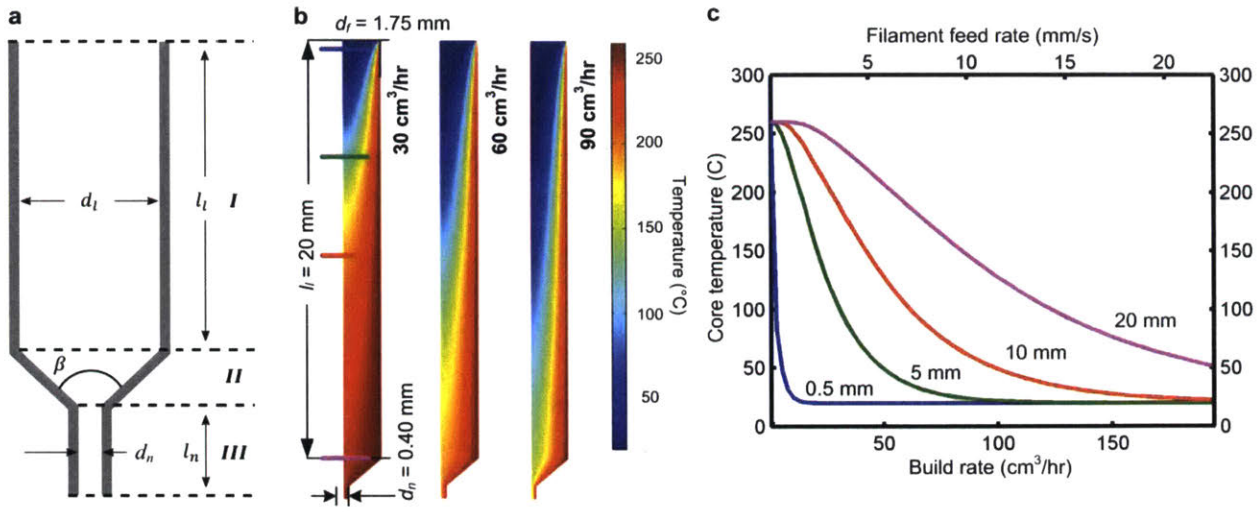

Figure III.7 Finite element analysis of heat transfer within the liquefier: (a) diagram of the three geometric regions of the liquefier: (I) heater tube, (II) constriction, and (III) nozzle; (b) temperature distribution within the liquefier at volumetric rates of 30 cm^3/hr

They also measured the extrusion force for different filament feed rate at different exit temperature as shown in Figure III.8. The sudden rise of the force indicates insufficient heat transfer which leads rigid material jam at the nozzle, and the final force drop implies the failure of the pinch wheel mechanism to grip the filament.

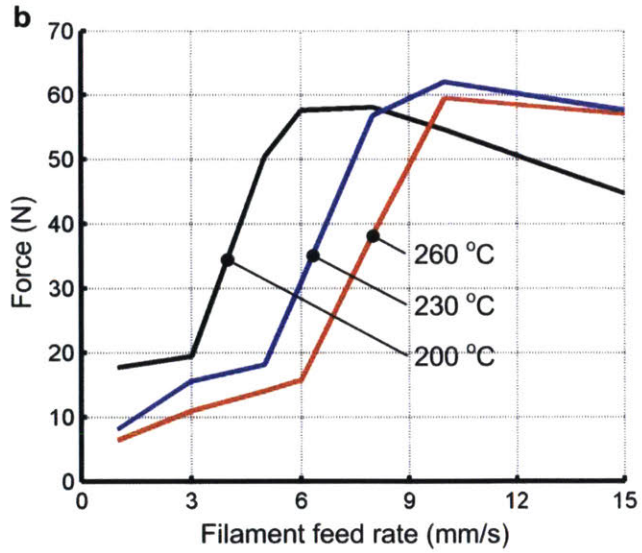

Figure III.8 Measured relationships with between filament feed rate and extrusion force at three liquefier setpoint temperatures [25]

In order to evaluate the efficiency of energy use in FDM technology, the measured energy consumption is compared to theoretical minimum energy requirement. Since ABS material is amorphous, the boundary for minimum energy required is defined such that the material is adiabatically heated to an average temperature of 229 °C from 20 °C. The model assumes no

heat loss during the filament heating at the liquefier. The adiabatic energy consumption per mass is given by equation 3.9 below, in which $\overline{C_p}$ is the average heat capacity for ABS material over the temperature range. With the parameters mentioned earlier in this section, the minimum energy consumption per mass is calculated to be 435 kJ/kg. When compared to the values measured by Corman and EPRI, the specific energy consumption ratio is rather low at 0.1% to 1%.

$$\frac{E}{m} = \overline{C_p}\left(T_{bulk} - T_{ref}\right) \quad \text{Eq. 3.9}$$

Manufacturer	Model	Material	Measured specific energy [J/kg]	Ratio of specific energy consumption	Reference
Stratasys	Dimension Elite	ABS (ABSplus)	1.7E+08	0.26%	Corman 2014
Stratasys	Fortus 360mc	ABS	2.9E+08	0.15%	Corman 2014
Stratasys	Mojo	ABS related	4.1E+07	1.05%	Corman 2014
Stratasys	Fortus 400 MC	ABS related	2.8E+08	0.16%	EPRI 2014
Stratasys	Fortus 900 MC	ABS related	4.0E+08	0.11%	EPRI 2014

Table III.3 Measured specific energy consumption for FDM processes with ABS material

According to Corman's measurement, the power consumption of the extruder are similar (around 30W) for machines with different build volume. The major energy consumption difference results from the chamber heating unit, which is also the biggest power consumption unit of the machine. During the printing process, by flowing hot air into the chamber continuously, the enclosed build chamber is kept at 95 °C to avoid warping as well as to minimize internal stress of the building part. Chamber heating takes as high as 80% of total energy consumed, while the energy consumption directly related to printing is measured to be 5% [3]. Bigger building area, hence bigger chamber, would greatly increase the energy consumption. To improve the specific energy consumption for FDM process would require better heat insulation for the chamber and possibly a more efficient way to deliver heat into the chamber.

1.2. Heat transfer modeling for big area additive machining

The BAAM machine is a new technology advertised for its high processing rate compared to most other additive technologies. Short carbon fiber filled thermoplastic material in the form of pellets is first dried, and then loaded into a traditional single screw extruder. Electric heating is applied at the wall of the barrel. Viscous heating also contributes to the melting of pellet material. The processing rate can be as high as 12.6 g/s (45.4 kg/hr) [27].

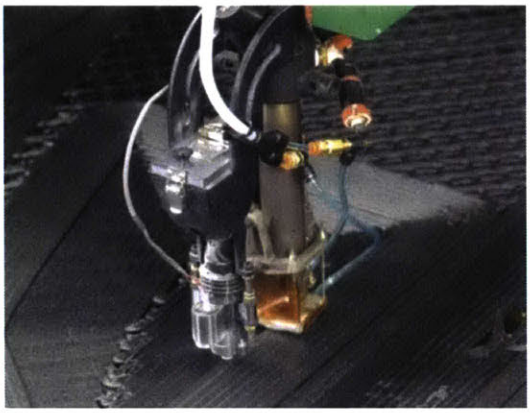

Figure III.9 Extruder used in BAAM machine

Since there is no die (significant back pressure) at the dispensing nozzle, and also for simplicity, only the screw extruder is considered in modeling the flow and heat transfer. For a single screw extruder, the output is mainly dependent on its geometries and the rotational speed.

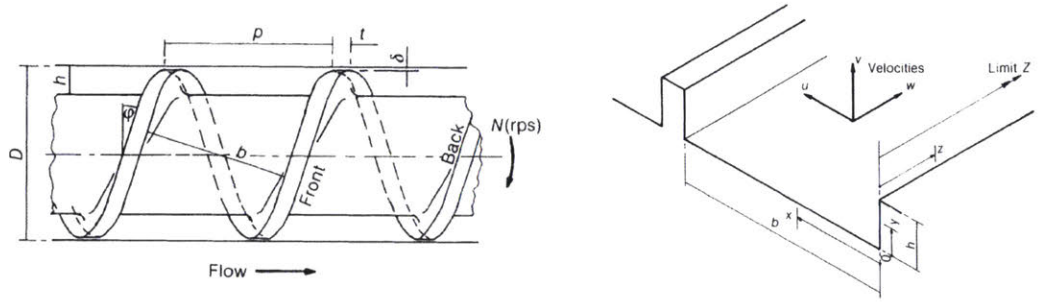

Figure III.10 Geometry of a single screw extruder and coordinates system for screw channel [28]

With the assumptions that flow within the extruder reaches steady state; the polymer adheres to the barrel and screw root surface; the channel depth is small compared to barrel diameter; no leakage flow; Newtonian fluid; isothermal flow; no curvature of the helical channel [28], flow within the extruder could be modeled as combination of drag flow and pressure flow.

The barrel velocity could be resolved in the channel coordinates as equation 3.10. In the equation, W is the velocity along the channel, U is the velocity perpendicular to the channel direction, D is the inner diameter of the barrel, N is the rotational speed of the screw, φ is the angle between flight and cross section of the screw as shown in both Figure III.10 and 3.11.

$$W = \pi DN\cos\varphi$$
$$U = \pi DN\sin\varphi \quad \text{Eq. 3.10}$$

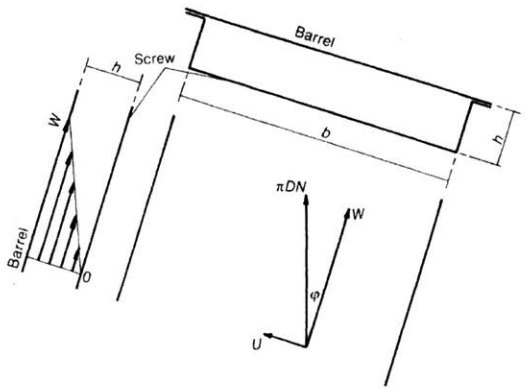

Figure III.11 Velocities in drag flow

For Newtonian fluid and simple shear scenario, the shear rate will be determined by equation 3.11 below, where h is the channel depth.

$$\dot{\gamma} = \frac{dw}{dy} = \frac{W}{h} \quad \text{Eq 3.11}$$

From momentum conservation equation (assuming infinite plate width for simplicity, i.e. axial flow velocity w is independent of x), we have:

$$0 = -\frac{1}{\rho}\frac{\partial P}{\partial z} + \mu\frac{\partial^2 w}{\partial y^2} \quad \text{Eq. 3.12}$$
$$0 = -\frac{1}{\rho}\frac{\partial P}{\partial y}$$

Solving equation 3.12 with the boundary condition that $w(y=0)=0$ and $w(y=h)=W$, the flow rate could be expressed as:

$$Q_{long} = \int_0^h wb \times dy = \int_0^h \left(\frac{W}{h}y - \frac{y}{2\mu}\frac{dP}{dz}(h-y)\right) b \times dy \quad \text{Eq. 3.13}$$
$$= \frac{Wbh}{2} - \frac{bh^3}{12\mu}\frac{dP}{dz}$$

Note that dP/dz is a constant. Since the more accurate boundary condition would also include the velocity of the flow at the flights, i.e. $w(x=0)=w(x=b)=0$, the longitudinal flow rate obtained from equation 3.13 is overestimated. The solution is revised by Rowell and Finlayson with empirical results [29], in which net flow rate down channel is given by equation 3.14. In this equation, F_d and F_p are "shape factors" for the drag flow and pressure flow respectively. Both shape factors are smaller than 1 and dependent on the value of h/b. When h/b is very

small, both factors would approach unity. Q_{drag} denotes the drag flow, while $Q_{pressure}$ denotes the pressure flow.

$$Q_{long,complete} = \frac{Wbh}{2} F_d - \frac{bh^3}{12\mu} \frac{dP}{dz} F_p = Q_{drag} - Q_{pressure} \quad \text{Eq. 3.14}$$

Similarly, transverse flow velocity profile could be determined with equation 3.15 below, where y is the dimension along the width of the channel.

$$u = \frac{U}{h} y - \frac{y}{2\mu} \frac{dP}{dx} (h - y) \quad \text{Eq. 3.15}$$

Since it is assumed that there is no leakage flow, the net transverse flow is 0. The pressure gradient could therefore be determined, which leads to the velocity profile to be:

$$u = (-2\frac{y}{h} + 3\frac{y^2}{h^2})U \quad \text{Eq. 3.16}$$

The transverse flow would therefore carry the material to the pushing flight as shown in Figure III.12 below, in this case the channel depth h would reduce to the melt film thickness δ_t.

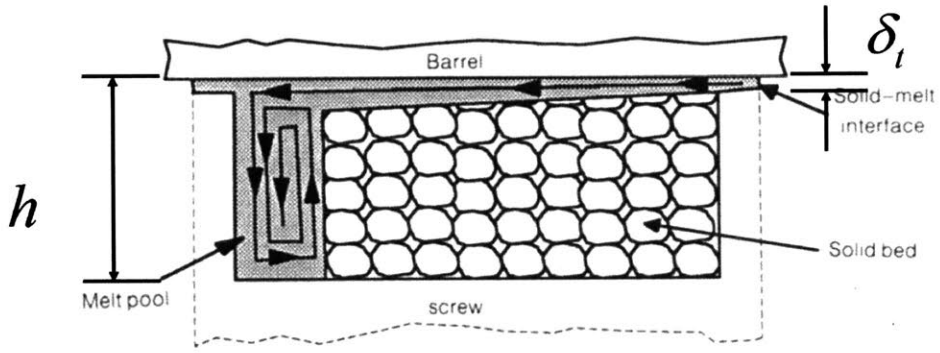

Figure III.12 Transvers flow in a single screw extruder at the melt zone [28]

Based on empirical results, a qualitative description for the melting mechanism within the extruder was proposed by Maddock 1959 [30]. Covas 1995 [28] further divided the overall process into four different zones: solid conveying zone, delay zone, melting zone, and pumping zone as shown in Figure III.13 below. In the solid conveying zone, loose polymer pellets become compacted as they progress along the channel. The delay zone refers to the region where a thin melt film is developed at the barrel material interface while the main fusion mechanism has not started. In the melt zone, solid material and melt are well segregated. Molten material is accumulated at the pushing flight. In the pumping zone, the molten material is well mixed and ready to extrude through the orifice.

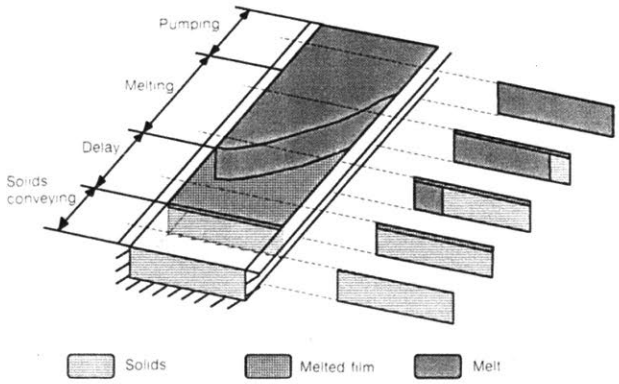

Figure III.13 Four different zones in single extruder melting polymer pellets [28]

In order to determine the limiting factors on process rate (i.e. flow rate), the phenomenon within these four zones need to be studied carefully. For example, the delay zone starts when the material becomes compacted such that heat from the high temperature barrel and friction dissipation is enough to melt the material at the barrel material interface. The melt film will first slide through the gap between the screw tip and the inner barrel wall. The mechanism depicted in Figure III.12 and 3.13 will happen when the film thickness is much greater (usually 5 to 7 times as observed in practice) than the gap dimension. The pushing flight of the screw will then scrap off the melt to form a pool of molten material. The end of the melting zone is marked by the full melting of the solid material. The pumping zone dimension determines the strain distribution within the material. The analysis will focus on the delay zone and melt zone.

In the solids conveying zone, particles (pellets) are compacted to a higher pressure than the initial pressure.

Heat transfer from the hot barrel and heat dissipation occur mostly in the delay zone and melt zone. We will follow the model developed by Tadmor and Gogos 1979 to investigate the relation between heat transfer and the processing rate (melt rate, material feeding rate) of a single screw extruder [31].

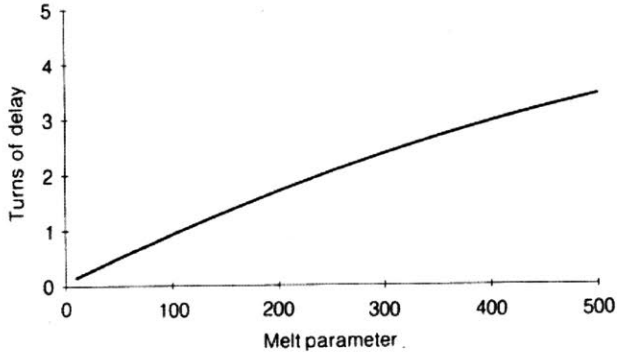

Figure III.14 Length of the delay zone in terms of melt parameter [32]

In the delay zone, the material at the inner surface of the barrel continues to melt due to frictional heat and wall heating. However, the film does not accumulate at the pushing flight. There has been no simple mathematical model to describe the delay zone. To avoid lengthy discussion, the experiment data of the delay zone length from Tadmor and Klein 1970 is shown in Figure III.14 above. The melt parameter is a dimensionless number $\zeta = \frac{Q_{lm,c}}{\rho_s b V_{sz}}$ which will be discussed in detail in the following part.

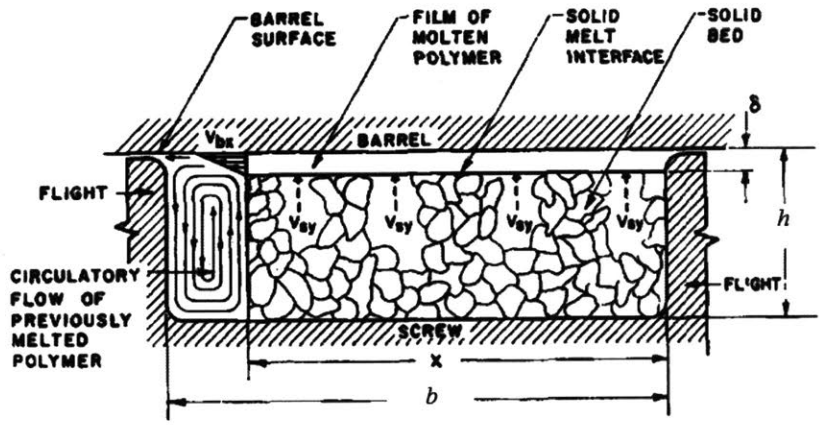

Figure III.15 Cross section view of a channel in melt zone [33]

The schematic for a typical cross section of the melting zone is shown in Figure III.15, note that for simplicity the origin of y axis is moved to the surface of barrel [33]. The figure shows typical Maddock melting mechanism. The basic assumptions include: melting reaches steady state both dynamically and thermodynamically, the solid melt interface is at the same depth in the channel (i.e. the film thickness is constant throughout the melting zone), material is assumed to be crystalized (i.e. a sharp melting point is expected), the solid bed is continuous and rigid, cross section is rectangular.

During the melting process, heat is transferred from the hot barrel through the moving film to the melt-solid interface. The barrel is assumed to be at a constant elevated temperature. Viscous heating is also generated and dissipated during the process. Heat transfer and circulation within the melt pool is neglected. Heat transfer down the channel length due to conduction and convection is also neglected. Temperature is assumed to be uniform across the width (i.e. temperature is only function of depth). It is also assumed that melting only occurs at the solid melt interface. Since material is continuously removed from the melt-solid interface, the interface is moving at a velocity of V_{sy} to keep the film thickness constant. For simplicity, the screw is assumed to be stationary, while the barrel rotates at N rpm.

To derive a mathematical model for this process, heat transfer is considered within the melt film, at the melt solid interface and within solid bed of material. Mass conservation is considered under the incompressible material assumption. Momentum conservation is considered assuming the melt is Newtonian and purely drag induced.

The heat transfer within the solid bed of material could be modeled as heat transfer through semi-infinite solid bed with equation 3.17, where ρ_s is the density of solid material, C_s is the heat capacity of solid material, k_m is the thermal conductivity of the solid material.

$$\rho_s C_s V_{sy} \frac{dT_s}{dy} = k_s \frac{d^2 T_s}{dy^2} \quad \text{Eq. 3.17}$$

Solving this equation with the boundary condition that $T_s(y=-\delta)=T_m$ and $T_s(y=-\infty)=T_r$, the temperature profile within the solid bed could be expressed with equation 3.18, where T_m is the melting temperature of the material, T_r is the reference (initial) temperature of the solid at the screw.

$$\frac{T_s - T_r}{T_m - T_r} = e^{\frac{\rho_s C_s V_{sy}}{k_s}(y+\delta)} \quad \text{Eq. 3.18}$$

Heat transfer into the solid material at the surface is then calculated to be constant:

$$q_{s,0} = k_s \left.\frac{dT_s}{dy}\right|_{y=-\delta} = \rho_s C_s V_{sy}(T_m - T_r) \quad \text{Eq. 3.19}$$

Since at the melt interface, net heat transfer is balanced with the fusion energy of the material. The energy balance equation could be written as equation 3.20, where k_m is the thermal conductivity of melt, λ is the latent heat of fusion.

$$k_m \left.\frac{dT}{dy}\right|_{y=-\delta} = k_s \left.\frac{dT_s}{dy}\right|_{y=-\delta} + \rho_s V_{sy}\lambda = \rho_s V_{sy}\left(C_s(T_m - T_r) + \lambda\right) \quad \text{Eq. 3.20}$$

The energy balance within the melt at steady state condition is given by equation 3.21, where μ is the dynamic viscosity of the melt.

$$k_m \frac{d^2 T}{dy^2} + \mu\left(\frac{dv}{dy}\right)^2 = 0 \quad \text{Eq. 3.21}$$

For Newtonian drag flow $v = (1+\frac{y}{\delta})\Delta V$, where $\Delta V = \sqrt{(W - V_{sz})^2 + U^2}$ is the velocity difference between the barrel (V_b) and the solid melt surface (V_{sz}). The boundary conditions are $T(y=0)=T_b$ and $T(y=-\delta)=T_m$, where T_b is the temperature of the heated barrel. The temperature within the melt is then solved as equation 3.22.

$$\frac{T - T_b}{T_b - T_m} = \frac{1}{2}\frac{\mu \Delta V^2}{k_m}\frac{y^2}{\delta^2} + \frac{1}{2}\frac{\mu \Delta V^2}{k_m}\frac{y}{\delta} + \frac{y}{\delta} \quad \text{Eq. 3.22}$$

The temperature profile within the solid bed and melt film could be constructed as shown in Figure III.16.

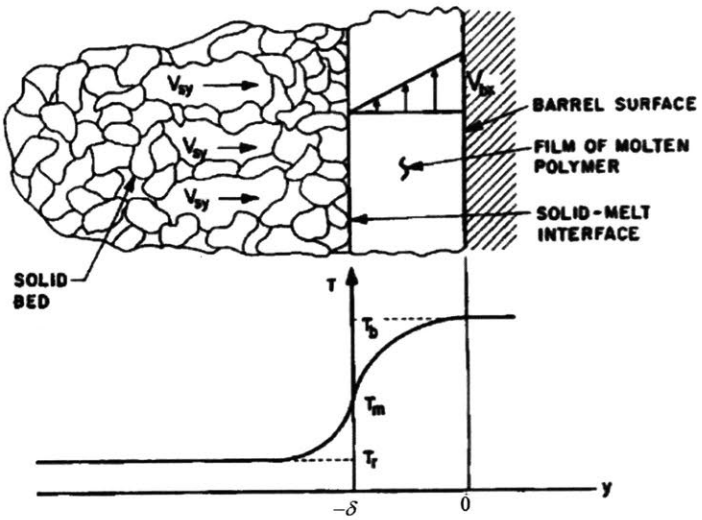

Figure III.16 Temperature profile within the solid bed and melt film [33]

Substitute equation 3.22 into equation 3.20, we get an energy balance rate equation with heat transfer from the barrel and viscous heating increasing the energy of the material:

$$\frac{k_m(T_b - T_m)}{\delta} + \frac{1}{2}\frac{\mu \Delta V^2}{\delta} = \rho_s V_{sy}\left(C_s(T_m - T_r) + \lambda\right) \quad \text{Eq. 3.23}$$

From mass conservation, the melting rate at the solid melt interface is equivalent to the transverse flow rate which accumulates the melt in a pool. In equation 3.24, X denotes the width of unmolten solid bed.

$$V_{sy} X \rho_s = \frac{1}{2} U \delta \rho_m \quad \text{Eq. 3.24}$$

Combining equation 3.26 and 3.24, we obtain the melt layer thickness to be:

$$\delta = \sqrt{\frac{\left(k_m(T_b - T_m) + \frac{1}{2}\mu \Delta V^2\right) X}{\frac{1}{2}\rho_m U\left(C_s(T_m - T_r) + \lambda\right)}} \quad \text{Eq. 3.25}$$

The flow rate per length of the channel could therefore be determined as:

$$Q_{lm} = \frac{1}{2} U \delta \rho_m = \sqrt{\frac{\rho_m U\left(k_m(T_b - T_m) + \frac{1}{2}\mu \Delta V^2\right) X}{2\left(C_s(T_m - T_r) + \lambda\right)}} \quad \text{Eq. 3.26}$$

Tadmor and Gogos 1975 argues that since the melt thickness is assumed to be constant, the melt material at surface could be viewed as teleported into the pool at average temperature through the melt thickness. Therefore, equation 3.20 should be modified into:

$$\frac{k_m(T_b - T_m)}{\delta} + \frac{1}{2}\frac{\mu\Delta V^2}{\delta} = \rho_s V_{sy}\left(C_s(T_m - T_r) + \lambda + C_m(\bar{T} - T_m)\right) \quad \text{Eq. 3.27}$$

The mean temperature is determined by equation 3.31 below, where $Br = \frac{\mu\Delta V^2}{k_m(T_m - T_b)}$ is the Brinkman number.

$$\frac{1}{2}U\bar{T}\delta = \int_{-\delta}^{0} TU(1+\frac{y}{\delta})\times dy$$
$$\bar{T} = T_m + (T_b - T_m)\left(\frac{2}{3} + \frac{Br}{12}\right) \quad \text{Eq. 3.28}$$

The corrected melt rate per unit length would be:

$$Q_{lm,c} = \sqrt{\frac{\rho_m U\left(k_m(T_b - T_m) + \frac{1}{2}\mu\Delta V^2\right)X}{2\left(C_s(T_m - T_r) + \lambda + C_m(T_b - T_m)\left(\frac{2}{3} + \frac{Br}{12}\right)\right)}} \quad \text{Eq. 3.29}$$

For a constant depth channel, we have

$$Q_{lm,c}dz = \rho_s h V_{sz} dX \quad \text{Eq. 3.30}$$

Integrating equation 3.30 from the start of the melting zone, the width of the solid material down the melting zone at length z is then expressed in equation 3.31 below.

$$X = b\left(1 - \frac{z}{2h\rho_s V_{sz}\sqrt{b}} \times \sqrt{\frac{\rho_m U\left(k_m(T_b - T_m) + \frac{1}{2}\mu\Delta V^2\right)}{2\left(C_s(T_m - T_r) + \lambda + C_m(T_b - T_m)\left(\frac{2}{3} + \frac{Br}{12}\right)\right)}}\right)^2 \quad \text{Eq. 3.31}$$

The length of the melting zone is determined taking the width of unmolten solid bed to be 0.

$$Z_{melting} = \frac{2h\rho_s V_{sz}\sqrt{b}}{\sqrt{\frac{\rho_m U\left(k_m(T_b - T_m) + \frac{1}{2}\mu\Delta V^2\right)}{2\left(C_s(T_m - T_r) + \lambda + C_m(T_b - T_m)\left(\frac{2}{3} + \frac{Br}{12}\right)\right)}}} \quad \text{Eq. 3.32}$$

In this equation, the velocity of the solid bed could be determined considering the mass flow rate $\dot{M} = V_{sz} bh\rho_s$ at the beginning of melting zone by assuming the solid material is rigid. The mass flow rate could therefore be determined by equation 3.33.

$$\dot{M} = \frac{Z_{melting}}{2}\sqrt{\frac{\rho_m U\left(k_m(T_b - T_m)\left(1+\frac{1}{2}Br\right)\right)b}{2\left(C_s(T_m - T_r)+\lambda+C_m(T_b - T_m)\left(\frac{2}{3}+\frac{Br}{12}\right)\right)}} = Z_{melting}\times\frac{1}{2}Q_{lm,c}\Big|_{X=W \text{ or } z=0} \quad \text{Eq. 3.33}$$

This model indicates that the mass rate is the product of the per unit length melt rate at the beginning of the melt zone and melting zone length. From the expression of the per unit length mass flow rate, we can conclude that the melt rate is determined by the channel width, heat transfer from the barrel wall, viscous dissipation and the enthalpy change of the material. The residence time could be calculated as in equation 3.34. It can be seen that the residence time is proportional to the square root of transvers flow travel time as well as the square root of characteristic time in depth direction. This is different from the heat transfer in the FDM process where the residence time is only proportional to the characteristic time in radial direction.

$$t_{residence} = \frac{2h\rho_s\sqrt{b}}{\sqrt{\frac{\rho_m U\left(k_m(T_b - T_m)+\frac{1}{2}\mu\Delta V^2\right)}{2\left(C_s(T_m - T_r)+\lambda+C_m(T_b - T_m)\left(\frac{2}{3}+\frac{Br}{12}\right)\right)}}}$$

$$= \left(\sqrt{\frac{b}{U}}\times\sqrt{\frac{h^2}{\frac{k_m}{\rho_m C_m}}}\right)\times\frac{2\sqrt{2}}{\sqrt{\frac{(1+\frac{1}{2}Br)}{\frac{C_s(T_m - T_r)}{C_m(T_b - T_m)}+\frac{\lambda}{C_m(T_b - T_m)}+\left(\frac{2}{3}+\frac{Br}{12}\right)}\times\frac{\rho_m^{\,2}}{\rho_s^{\,2}}}} \quad \text{Eq. 3.34}$$

$$= t_0 \times Coeff_{BAAM}{}^{-1}\left(Br, T^*, \frac{\lambda}{C_m(T_b - T_m)}, \frac{\rho_m}{\rho_s}\right)$$

The mass flow rate could then be expressed substituting equation 3.34 into $\dot{M} = V_{sz} bh\rho_s$:

$$\dot{M}_{BAAM} = \rho_s\frac{Z_{melting}}{t_{residence}}\times hb = \rho_s Z_{melting}\sqrt{Ub\alpha}\times Coeff_{BAAM}\left(Br, T^*, \frac{\lambda}{C_m(T_b - T_m)}, \frac{\rho_m}{\rho_s}\right) \quad \text{Eq. 3.35}$$

$$\dot{M}_{FDM} = \rho_s\alpha L\times Coeff_{FDM}(T^*)$$

Some simple observation from the equation would instruct us about the possible routes to increase the throughput of a single extruder. These routes include increasing the rotational speed

of the screw, increase the channel width, and increase the overall length of the extruder such that the length of the melting zone could be increased. Note that these methods will also affect the coefficient in the equation. For example, the Brinkman number is determined by the relative velocity of the barrel surface to the solid surface, and is therefore influenced by the rotational speed of the screw. The model described in this section is based on simple boundary conditions in order to get analytic solutions. There are other important factors which might greatly affect the results, such as non-Newtonian fluid properties, different melting mechanism, pressurized extruder, complex screw geometries (tapered screw, two-step screw), etc. Also note that axial screw length is determined by the different requirements posed by the four different zones on the separate zone length.

The model described by equation 3.35 is then used to estimate the process rate of BAAM machine. Since no data is available on the geometry of BAAM extruder, the dimensions used will be crude estimates from a video [34]. The parameters used in estimation is summarized in Table III.4 assuming square-pitch extruder. Since it is rather hard to determine the axial length of melting zone without knowing the requirements and boundary conditions in all four different zones, the axial length of the melting zone will be taken as 1/2 (i.e. 10 turns) according to empirical results from other researchers [35]. The mass rate is calculated to be:

$$\dot{M}_{BAAM} = \rho_s Z_{melting} \sqrt{Ub\alpha} \times Coeff_{BAAM}\left(Br, T^*, \frac{\lambda}{C_m(T_b - T_m)}, \frac{\rho_m}{\rho_s}\right) \quad \text{Eq. 3.36}$$

$$= 0.053 \times Coeff_{BAAM}\ {}^{kg}/_{s} = 190 \times Coeff_{BAAM}\ {}^{kg}/_{hr}$$

The coefficient is estimated to be around 0.84 for the given parameters. As a result, the estimated mass rate is 0.045 kg/s, which is 160 kg/hr. The measured rate is 28% of the modeled rate. Apart from the errors caused by the inaccuracy of the parameters used, the other potential causes for the low percentage are inefficiency in build paths and print strategy, constraints from the capability of the mechanical gantry system, the constraints from other working zones that are not included in this model.

Parameter	Value	Reference
Heat capacity C_p [J/(kg-K)]	2080	[23]
Thermal conductivity k [W/(m-K)]	0.18	[24]
Density [kg/m^3]	1050	[23]
Dynamic viscosity μ [Pa-s]	155 to 1550	[23]
Screw axial length [m]	0.6	[34]
L/D	20	[34]
Channel width [m]	0.028	[34]
Rotational speed [rpm]	40	[35]
Helix angle [degree]	17.7	[36]

Table III.4 Parameters used in heat transfer modeling for FDM machine with ABS material

From an energy perspective view, viscous heating in BAAM machine is substantial as the Brinkman number is 200, which is much greater than one. It also suggests that at higher throughput, viscous heating will become more and more dominating. As a result, mechanical power of the extruder needs to be accounted in addition to barrel heating when considering the energy use efficiency for BAAM machine. For the proposed model, material is heated from the intial temperature at the start of the melting zone to the temperature $\overline{T}(Br, T_b, T_m)$ which is greater than melting temperature. As mentioned in the previous section, heating the filament material in FDM process is very efficient due to the adiabatic assumption. In the proposed model for BAAM extruder, heating is also very efficient even though heat is transfered into the screw shaft through the solid bed. This is due to the low thermal conductivity of the solid material. The heat tranfer into the shaft is determined by equation 3.37. It becomes neglegible when estimated with the parameters in Table III.4.

$$q_{shaft} = k_s \left.\frac{dT_s}{dy}\right|_{y=-h} = \rho_s C_s V_{sy}(T_m - T_r) e^{\frac{\rho_s C_s V_{sy}}{k_s}(-h+\delta)} = e^{\frac{\rho_s C_s V_{sy}}{k_s}(-h+\delta)} q_{s,0} \quad \text{Eq. 3.37}$$

In real case scenario, heat transfer from melt pool to the pushing flight and screw shaft could be substantial before the shaft is heated up to similar temperature because of the high thermal conductivity of the shaft material. The melting zone, if well insulated, could be very efficient in energy utilization.

2. Conclusion

To study the processing rate of material extrusion process, heat transfer model is developed. It is found out that, heat transfer is a major limiting factor on the processing rate in FDM machine. As a result, FDM machine equipped with the same extruder head have similar limited processing rate $\dot{M}_{FDM} = \rho_s \alpha L \times Coeff(T^*)$, which is mainly constrained by the length of the liquefier and the thermal diffusivity with the current setup. BAAM machine is equipped with a traditional screw extruder. Heat transfer also limits the processing rate to be $\dot{M}_{BAAM} = \rho_s Z_{melting} \sqrt{Ub\alpha} \times Coeff\left(Br, T^*, \frac{\lambda}{C_m(T_b - T_m)}, \frac{\rho_m}{\rho_s}\right)$. The processing rate is prescribed by the helical length of the melting zone, the transverse flow velocity at the barrel, the width of the channel, and thermal diffusivity. According to the model, the process rate for BAAM machine is estimated to be 160 kg/hr, while for FDM process it is 0.035 kg/hr.

IV. Processing Rate Modeling for Selective Laser Melting

To understand the phenomenon during laser beam melting powder material is crucial to improve processing rate, energy consumption, and part quality. Conducting experiments on selective laser sintering/melting systems, on the other hand, can be expensive and time consuming. Due to the short-time intensive heat transfer at the laser-powder interface, no direct observation is available to reveal thermal and fluidic behavior. Researchers have studied and built different theoretic models to understand phenomenon at different stages during selective laser melting powder materials.

In this chapter, existing models will first be reviewed. Three different models will then be presented to study the heat transfer phenomenon and processing limitations during the selective laser melting process.

1. Literature review

Processing rate of selective laser melting is closely related to energy transfer within the system. When laser beam scans over and melts designated region on the powder bed, highly concentrated energy is first transmitted from laser beam to powders; the absorbed energy is further transferred within the powder layer via different modes of heat transfer. The thermal history of the process also influences the melt pool behavior, part quality, etc. Researchers have studied heat transfer during the process to gain insight in the physical effects occurred.

Elsen et al. [37] applied a moving plane heat source model developed by Carslaw and Jaeger [38] to study heat transfer and temperature distribution in the process. In their analytic model, they focus on the conductive heat transfer and the heat source is assumed to have uniform power distribution. Temperature integrated bulk material properties are used throughout the numerical evaluation, physical property change of the material and fluid behavior occurred during phase change are not incorporated. The analytic solution demonstrates the general effect of different parameters on temperature field such as laser spot size, scanning speed, energy density.

Gusarov et al. [39] modeled the laser energy source with a one-dimensional volumetric heating model, in which laser light penetration in the powder bed is considered. The proposed numerical model considers the drastic change in material property during phase change, different average bulk values are used within solid and liquid phases. Effects from evaporation are not incorporated. The simulation results show that the melt pool size tends to increase with decreasing scanning velocity and with smaller beam spot diameter. The paper also shows that intensive evaporation occurs at low scanning velocity.

Verhaeghe et al. [40] investigated in the effect of evaporation and the effect of different substrate structure. They found that specific enthalpy changes significantly during evaporation. The numerical model applies similar boundary conditions as in Gusarov et al. 2007, the heat source is assumed to be stationary for simplicity. To contrast a dense metal substrate from deep powder bed, they applied volumetric heating models with different absorptivity via varying the optical thickness. For dense metal substrate, the optical thickness is taken to be infinity, this results a 20% loss of incoming laser energy to the substrate. The simulation results predict a smaller molten region compared to previous models. In fact, the predictions appeared to be smaller than experimental results.

Zhang and other authors [41]–[43] proposed models that takes into account of fluid flow driven by capillarity and gravity forces. In the model, they consider a mixture of two powders with significantly different melting points. The model tracks the melt front velocity using Darcy's law or Navier-stokes equation. The numerical simulation results matches the fusion boundary with experiments results. The modeled heat affection zone also shows similar geometry compared to empirical result.

These models highlighted crucial factors in modeling the energy and mass transfer phenomenon during selective laser melting including: laser material interaction, laser light penetration in porous material, material property with respect to temperature and phase change, conductive heat transfer, capillarity, shrinkage, etc.

2. Process description

Starting from the laser beam interacting the powder layer surface, the non-reflected collimated laser beam either gets absorbed by the lose powder or scatters into the powder layer. Since the porosity can be up to 50%, scattering and absorption increase the effective absorptivity to around 70% (for ferrous material), it will however drop to around 40% after the top layer is molten.

The thermal conductivity of loose powder are usually very low because of the low thermal conductivity of pores. As laser energy is being absorbed, the surface will first reach melting temperature where absorption is at its highest for typical metals used in powder bed fusion processes (aluminum, ferrous material, etc.).

Once the top surface is molten, capillary pressure attracts the liquid metal which fills the pores underneath it. The liquid metal then transfers heat to immersed particles. Due to a large increase in thermal conductivity, heat transfers faster from the surface to bottom. The imbibition also helps the immersed particles to get more exposed to the laser beam.

The surface layer may be vaporized because of the high energy intensity it is subjected to. The vapor will cause a recoil pressure to act on the melt pool, which will spread the molten material along the thickness as well as radially.

3. Laser systems in selective laser sintering/melting

A suitable laser system is key to the success of selective laser sintering/melting process. Intensive energy (3 J/mm^2) is to be deposited to a very small-size area (0.5 mm^2) during SLS/SLM process [13]. The nature of the process, therefore, demands the laser system to output high power with very good beam quality.

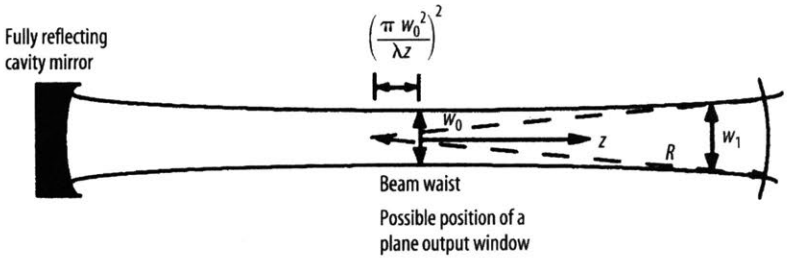

Figure IV.1 Scheme of beam quality

As shown in Figure IV.1 above, laser beam quality is characterized by beam waist w (radius of the narrowest point of laser beam) and divergence angle θ. An unmodified laser beam diverges by diffraction from the beam waist at an increasing rate. M^2 factor, or an average quality factor for laser beam, is defined as the ratio of the actual beam divergence divided by the divergence from an ideal-case Gaussian laser beam with the same initial waist radius. M^2 is independent of wavelength, but generally bigger at high laser power due to thermal effects.

$$M^2 = \frac{\theta_{act}}{\theta_{Gauss}} \quad \text{Eq. 4.1}$$

$$BPP = \theta \times r \quad \text{Eq. 4.2}$$

Beam parameter product (BPP) is the product of the divergence angle and beam waist. M^2 factor, therefore, can also be calculated as the ratio of BPP of an actual beam to that of an ideal Gaussian beam at the same wavelength. Gaussian beam has the lowest beam parameter product, which is:

$$BPP_{Gauss} = \frac{\lambda}{\pi} \quad \text{Eq. 4.3}$$

To satisfy the needs of selective laser sintering/melting, it is desired that laser system has low beam parameter product and M^2 factor values. Among the four major types of industrial lasers, CO_2 laser and solid state laser have lower beam parameter product compared to diode and excimer laser systems as can be seen in Figure IV.2 below.

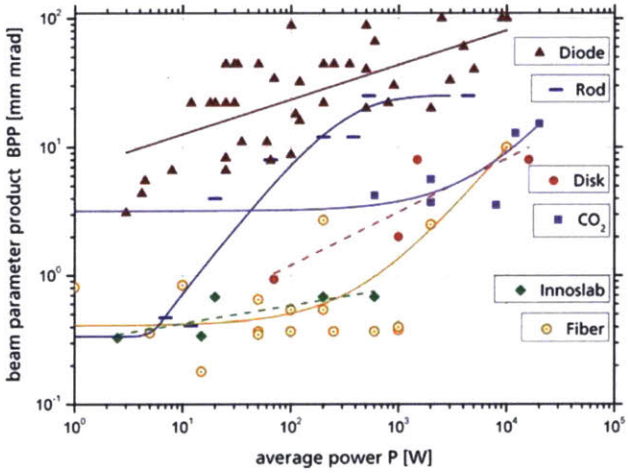

Figure IV.2 Beam parameter product for different lasers at different output power

Since the M^2 factor is sensitive to temperature of the active medium, different layer construction methods lead to different M^2 factors with different heat removal rate. For CO_2 laser system, good beam quality can be achieved with axial flow setup or diffusion-cooled setup. M^2 for diffusion cooling slab laser can be smaller than 1.1 for power up to 5 kW. For solid state laser system, fiber laser is preferred since the geometry of fiber leads to huge fraction of surface to volume from which heat can be removed. M^2 for a typical fiber laser can be smaller than 1.5 for power

up to 3 kW [44]. As shown in Table IV.1 below, most commercial selective laser sintering/melting manufacturers adopt CO_2 laser and Ytterbium fiber laser systems.

Manufacturer	Machine	Material	Laser Type	Laser Power [W]
EOS	M270	metal	Yb-fiber laser	200
	M280			200/400
	M290			400
	M400			1000
	P110	plastic	CO_2	50
	P396			70
	P760			2x50
	P800			2x50
SLM Solutions	SLM 125 HL	metal	YLR fiber laser	100/200
	SLM 280			400/1000
	SLM 500			2x400/2x1000
3D Systems	ProX 500	plastic	CO_2	100
	sPRo 60 SD			30
	sPRo 60 SD Base			30
	sPRo 60 SD HD-HS			70
	sPRo 140 Base			70
	sPRo 140 HS			200
	sPRo 230 Base			70
	sPRo 230 HS			200
	ProX 100	metal	Yb fiber laser	50
	ProX 200			300
	ProX 300			500

Table IV.1 Lasers used in some powder bed fusion systems (collected from online spec sheets)

4. Conductive heat transfer modeling

4.1.Physical properties

4.1.1 laser absorptivity

Radiation is the major way to transfer energy from laser to material. The ratio of absorbed energy from the incident energy is defined as absorptivity. For opaque materials, most metals for example, transmissivity is considered to be negligible and incident radiation energy is either reflected or absorbed. Many factors including laser wavelength, material temperature, and surface condition would affect absorptivity of a particular metal material of interest.

The absorptivity for an opaque solid at normal incidence as depicted in Figure IV.3 is given by Fresnel's equations [45], where n and k are the refraction index and extinction coefficient respectively. For most conductive material like metals, a free electron model by Drude is proven to be good approximation to obtain optical properties and to further calculate the absorptivity at infrared region [46]. According to Drude theory, the optical constants n and k can be approximated through Hagen-ruben relationship when angular frequency is much smaller than plasma frequency, where ω is angular frequency of the incident light, σ is the static conductivity of material, ε_0 is vacuum permittivity [45]. The absorptivity can be, therefore, expressed as equation 4.4, where ρ is static electric resistance of material, and λ is the wavelength of the incident light. The absorptivity is smaller when incident light is at longer wavelength. Experimental data has proven Hagen-ruben relationship to be a close fit at wavelength region greater than 1 micron, the as shown in Figure IV.4.

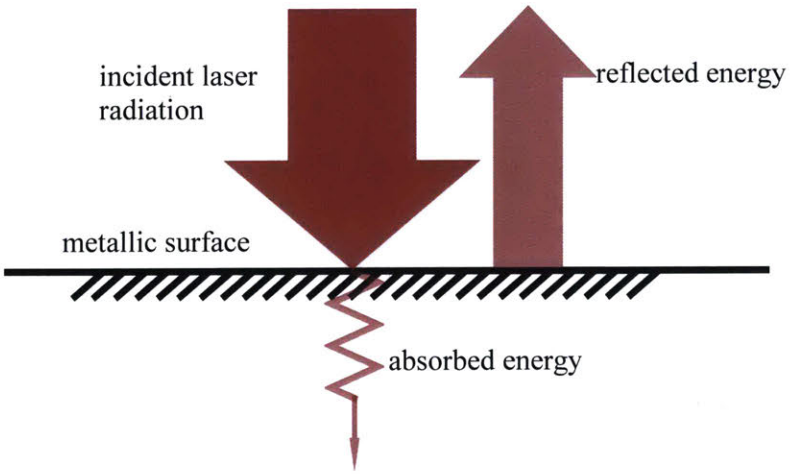

Figure IV.3 Normal incidence on an opaque solid

$$A = 1 - R = 1 - \frac{(1-n)^2 + k^2}{(1+n)^2 + k^2}$$

$$n \approx k = \sqrt{\frac{\sigma}{2\omega\varepsilon_0}} \qquad \text{Eq. 4.4}$$

$$A \approx 2\sqrt{\frac{2\omega\varepsilon_0}{\sigma}} = 365.15\sqrt{\frac{\rho}{\lambda}}$$

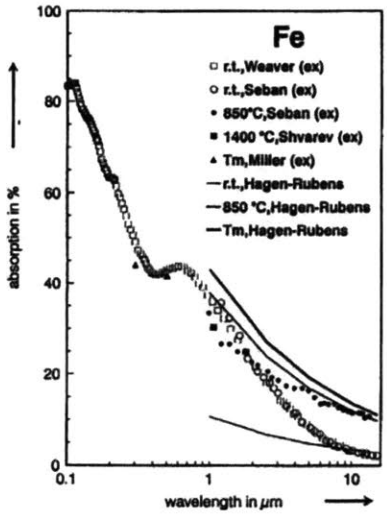

Figure IV.4 Absorptivity of iron as a function of wavelength [47]

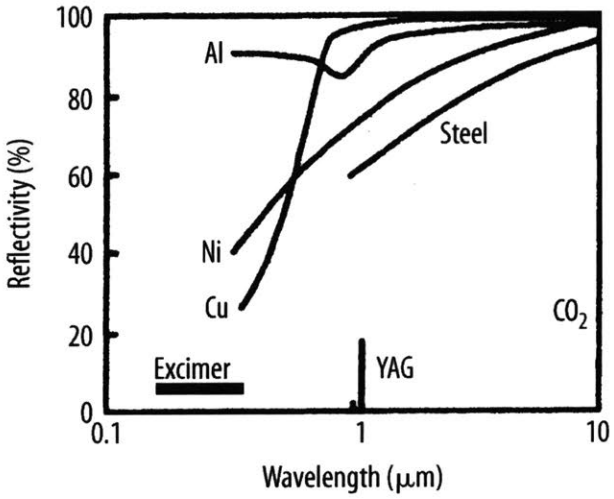

Figure IV.5 Reflectivity of a number of metals as a function of wavelength [48]

Generally at shorter wavelength, reflectivity of metal material decreases and absorptivity is larger than at longer wavelength, as shown in Figure IV.5 above. To achieve better energy absorption, metal selective laser melting application is usually equipped with laser system of 1.06 um wavelength.

The optical properties of metals is dependent on temperature, and this leads to a variation of absorptivity at different temperature. When interband contribution is negligible, the Drude model predicts an increase in absorptivity for metals at higher temperature since both static electric conductivity and relaxation time decreases with temperature. As can be seen in Figure IV.6 [49] and Figure IV.7 [50], most metals including transition metals have an increasing absorptivity with temperature. Note that Arnold obtained absorptivity for metals in Figure IV.7 by applying Drude theory with empirical optical properties. The absorptivity values have been proven in good agreement with experimental results. At a shorter wavelength, on the other hand, interband transitions has a significant effect on the absorptivity for transition metals (e.g., Fe, Co, Ni, Ti, Zr, etc.), and will result in an opposite trend where absorptivity decreases with temperature [51]. Seibold et al. showed with experiments the intrinsic decreasing trend of absorptivity for iron and low-carbon steel at near infrared wavelength, as shown in Figure IV.8 [52]. The absorptivity

would increase when the surface reaches melting temperature and the molten pool begins to spread from the heating center.

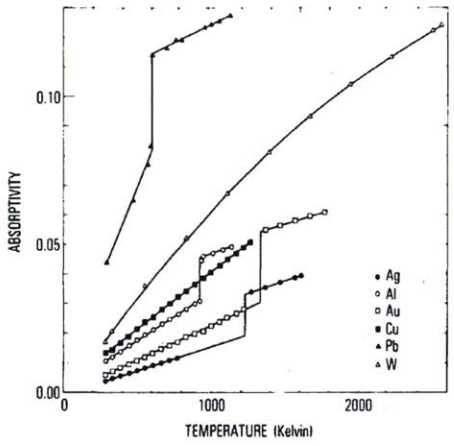

Figure IV.6 Increase in absorptivity of pure metals below and above the melting temperature for radiation with a wavelength of 10.6 μm [49]

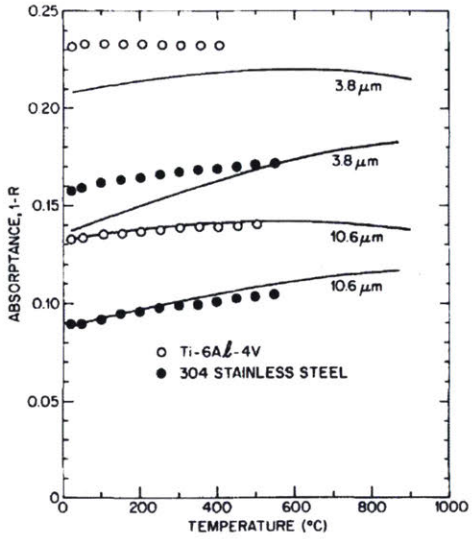

Figure IV.7 Temperature-dependent absorptivity for 304 steel and Ti6Al4V at 10.6 μm [49]

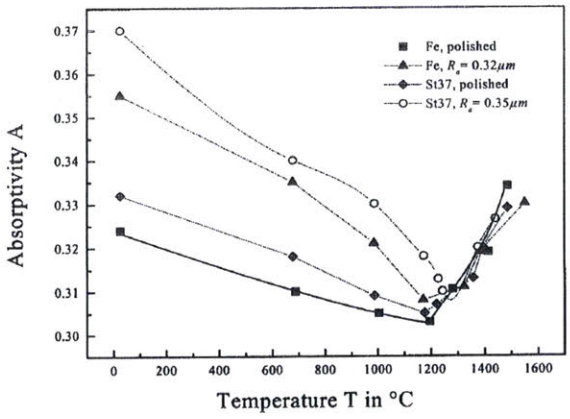

Figure IV.8 Temperature dependent absorptivity for iron and low carbon steel at 1.06 μm [52]

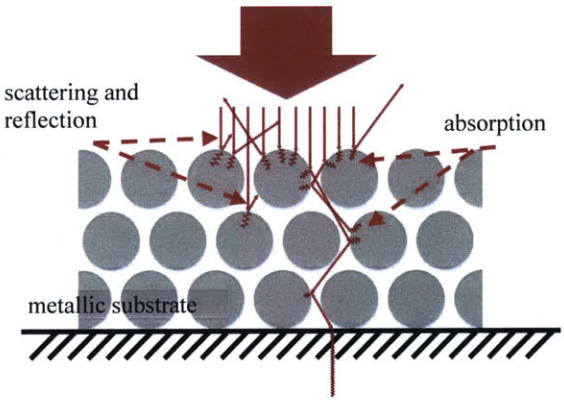

Figure IV.9 Scheme of laser beam penetrate through powder bed

In selective laser melting/sintering process, laser beam scans over a thin layer of powder bed deposited on substrate/sintered layer as shown in Figure IV.9. In industry practice, the new powder layer is usually 1-5 times as thick as average powder diameter (~25 μm) to ensure high resolution [53], [54]. The powders are usually loosely packed after recoating to avoid damage to

the previously built layer, the porosity can be as high as 40 percent [6]. Laser beam penetrates into the powder layer through multiple reflection on particle surface. Energy is carried beneath the surface, resulting in better absorption compared to dense material. Tolochko et al. measured reflection of normal incident laser beam on deep powder bed at room temperature [55]. The experimental results shows that absorptivity of metal powder is larger than that of dense material at both 10.6 μm and 1.06 μm.

The intensity of laser light travelling through a media can be derived according to Beer-lambert law, where I stands for transmitted laser intensity, I_s is the laser intensity absorbed by and transmitted through surface, β is extinction coefficient, z is depth within media.

$$I(z) = I_s e^{-\beta z} \quad \text{Eq. 4.5}$$

Extinction coefficient takes into account both absorption and scattering, and is assumed to be constant throughout the thickness. Rombouts et al. measured laser transmission intensity for loosely packed stainless steel powders with 0.54 μm wavelength laser, normalized transmittance decays exponentially with penetration thickness as shown in Figure IV.10 [56]. Stainless steel particles used in the experiment have a mean particle diameter of 57 μm. The extinction coefficient estimated from the regression is 51 mm^{-1}. Mcvey et al. also estimated extinction coefficient for iron particles through measurement from transmissive experiments. In their experiment, iron particles of different sizes were used with Nd:YAG laser at 1.06 μm. The results showed a good exponential fit for larger particle size (>100 μm), giving the average extinction coefficient to be 9.1 mm^{-1}. The experiments also showed that extinction coefficient tends to increase with decreasing particle size.

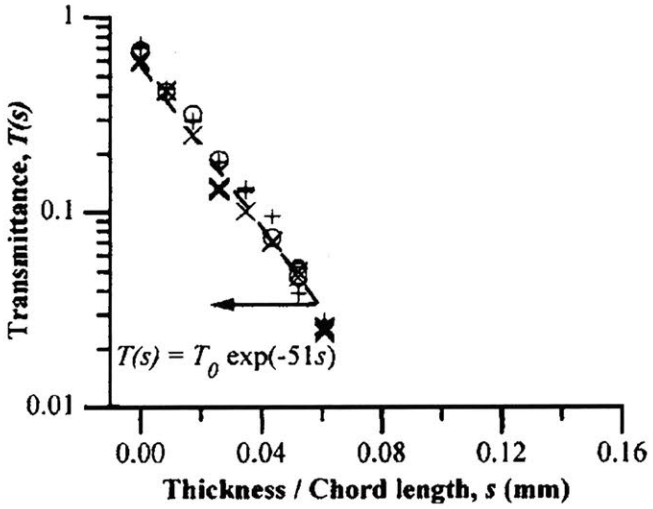

Figure IV.10 Normalized transmittance for stainless steel powders decays exponentially with penetration thickness, circles and crosses represent slightly different porosity

Assuming all the scattered energy is absorbed at the same depth within the powder bed for simplicity, the absorbed energy at different depth can be expressed as:

$$dE_{absorb}(z) = \beta I_s e^{-\beta z} dz \quad \text{Eq. 4.6}$$

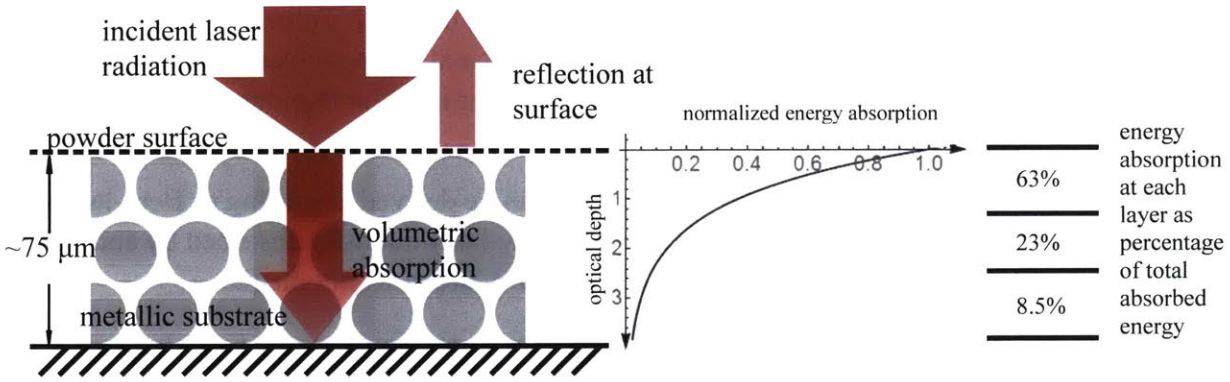

Figure IV.11 Volumetric heat absorption in powder bed (optical depth = β×z)

The absorbed energy decays exponentially through the layer thickness as suggested by equation 4.6. In typical selective laser melting process, mean particle size is around 20 to 25 μm and layer thickness is around 50 to 75 μm as shown in Figure IV.11. Due to volumetric heating, 63% energy is absorbed in surface layer and 5.5% energy reaches the bottom substrate.

4.1.2 thermal conductivity

After laser energy is absorbed through the powder layer, heat is transferred from irradiated particles to adjacent particles/substrate primarily through conduction before melting/consolidation occurs. According to Fourier's law, thermal conductivity of the powder bed is crucial in determining heat diffusion in this process. In material with larger thermal conductivity, heat can be directed to low temperature particles more quickly and avoid overheating at the surface.

The principal heat carriers in metals are electrons and lattice waves. Lattice thermal conductivity of metals is comparable to insulators of similar elastic properties. Generally in highly conducting (electrically) metals, heat conduction is dominated by free electrons. Due to the presence of free electrons, metals are usually good heat conductors (~10 to ~100 W/mK). Based on experiment measurements, Touloukian et al. proposed correlation for calculating metal thermal conductivity at different temperature. Although heat conductivity varies with increasing temperature, it generally remains at the same order [57].

Heat conductivity in powder bed with high porosity is substantially different from dense material. The existence of low thermal conductivity pores, usually air/inert gas (~0.01 W/mK), lowers the effective conductivity of the mixture. In powder bed, the effective thermal conductivity mainly depends on porosity, contact thermal conductivity and conductivity of gas phase when ratios of thermal conductivity of solid phase to gas phase is high ($k_s/k_g > 1000$).

Luikov et al. reported the effective thermal conductivity for powder steel lies within the range of 0.43 to 0.60 W/mK, while steel has thermal conductivity of 45 W/mK [58]. Gusarov et al. studied the effect of Knudsen number in modeling the thermal conductivity, results are shown in Figure IV.12. For ferrous material and copper powder bed material, the effective thermal

conductivity is within one order of magnitude compared to air, and much smaller than that of bulk material [59]. Alkahari et al. measured the thermal conductivity in powder bed using pulsed laser to deliver energy to material contained in a cylindrical vessel. Their results showed that thermal conductivity of steel powders increases with larger powder size and decreasing porosity [60]. The measured conductivity ranges from 0.07 to 0.22 W/mK.

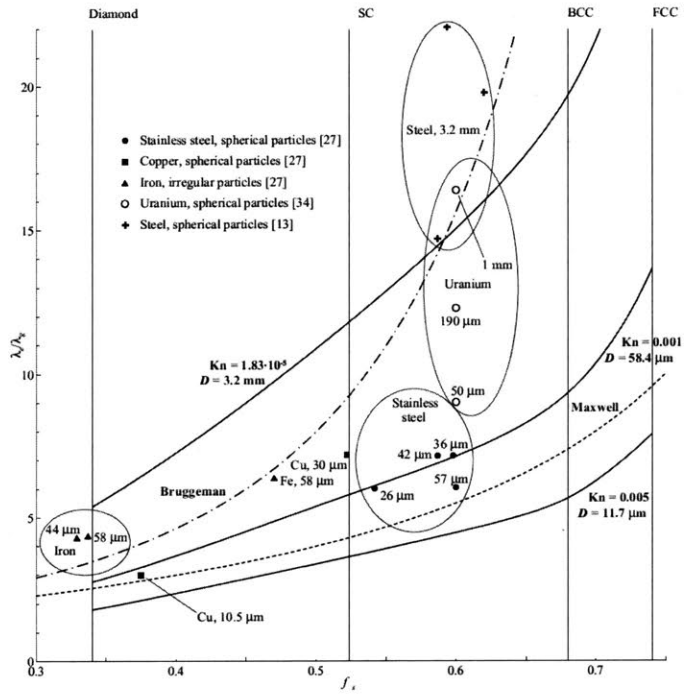

Figure IV.12 Effective thermal conductivity λe of powder and packed beds in air at the normal conditions versus the volume fraction of solid fs

4.2.Fluid behavior

During the melting process, after the surface layer is melted, the molten material will fill in the pores underneath due to capillary pressure as shown in Figure IV.13. Liquid phase metal transfers heat to the immersed particles. At the same time, as the molten material fills in the pores, the particles would be more directly exposed to laser radiation. These phenomenon help transfer heat to the bottom of the powder layer to be melted.

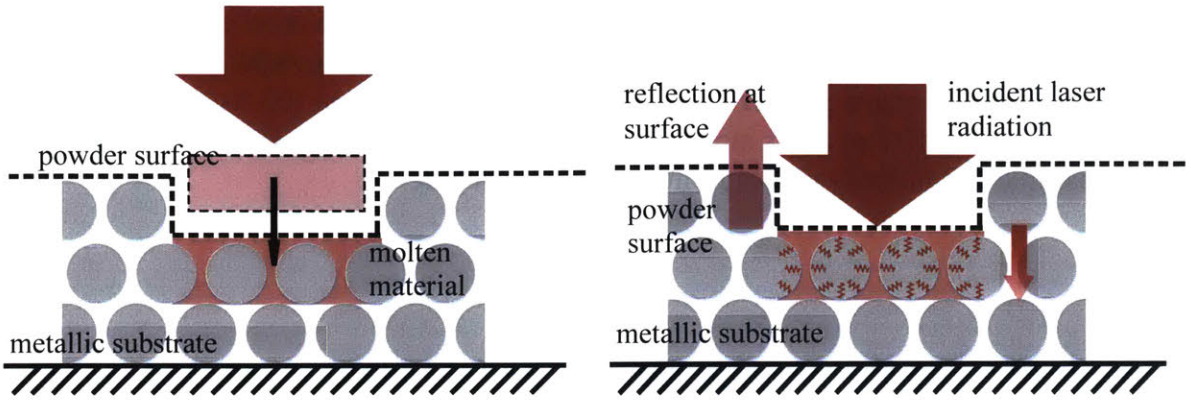

Figure IV.13 Molten material filling due to capillary pressure

To quantify the imbibition phenomenon, the capillary time scale is examined following the analytic method introduced by Pak and Plumb [61]. According to Darcy's law, the imbibition speed of liquid metal is defined by equation 4.7 for unsaturated flow, where K is permeability, μ is dynamic viscosity, p is pressure, ρ is the density of liquid:

$$u = -\frac{K}{\mu}\left(\frac{\partial p}{\partial x} + \rho g\right) \quad \text{Eq. 4.7}$$

The pressure gradient can be determined by equation 4.8. The meniscus of the top surface is flatter and has a bigger curvature compared to the bottle surface when the molten material starts to fill in the pores. Capillary pressure on the top surface can therefore be neglected. The pressure gradient diminishes when the molten material fully wets the next layer as shown in Figure IV.14.

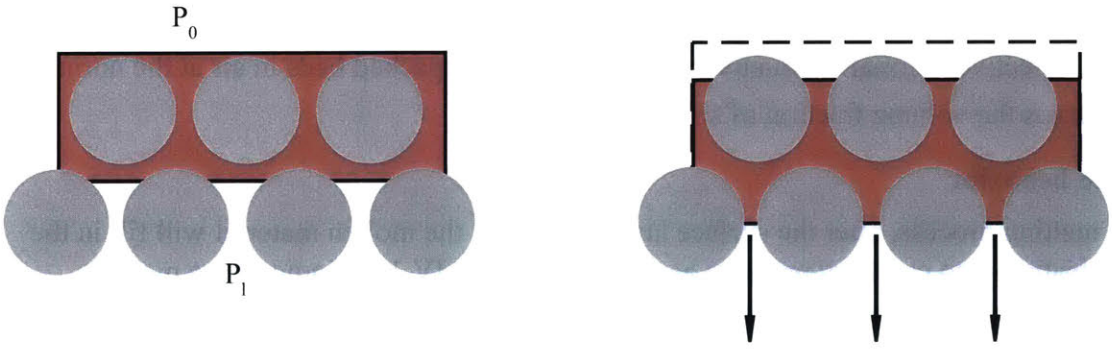

Figure IV.14 Pressure gradient of molten powder bed

$$\frac{\partial p}{\partial x} = \frac{p_0 - p_l}{d} = -\frac{p_l}{d} \quad \text{Eq. 4.8}$$

The permeability K can be obtained from the Carman-Kozeny equation modeling the porous solid as a bundle of capillary tubes, where d is the particle size and ε is the porosity.

$$K = \frac{d^2 \varepsilon^3}{180(1-\varepsilon)^2} \quad \text{Eq. 4.9}$$

The capillary pressure p is obtained from Leverett function which is assumed to depend on saturation only, where σ is the surface tension, S is normalized saturation and a = 0.38, b = 0.014, and c = -0.27 determined by Hofmann and Barleon [62]:

$$p = J\sigma\sqrt{\frac{\varepsilon}{K}} \quad \text{Eq. 4.10}$$

$$J = a(S+b)^c$$

The time scale can therefore be calculated as:

$$t = \frac{d}{u} = \frac{d}{\frac{K}{\mu}(\frac{p}{d}+\rho g)} \quad \text{Eq. 4.11}$$

The estimated time for penetration with 50% porosity and 50 μm mean particle size is then on the order of 0.01 ms [63], [64]. The penetration time is negligible when comparing to exposure time (~1 ms for 200 μm diameter, 0.1 m/s scanning speed) during which laser travels a full focus spot diameter. Fast penetration is significant in carrying heat from the surface into to the powder layer.

4.3. Adiabatic model

When laser beam scans over powder print bed, energy is transferred from laser to powder through heat radiation. During this process, the absorptivity of metal powder material (with respect to certain wave length radiation) determines the ratio of energy absorbed from the incident radiation, while the rest is either reflected or transmitted. The absorbed energy is then transferred within the powder bed by conduction and wetting of the melted material. To predict the theoretic rate limit of metal powder bed fusion process, heat transfer is assumed to be uniform and adiabatic within the melt region.

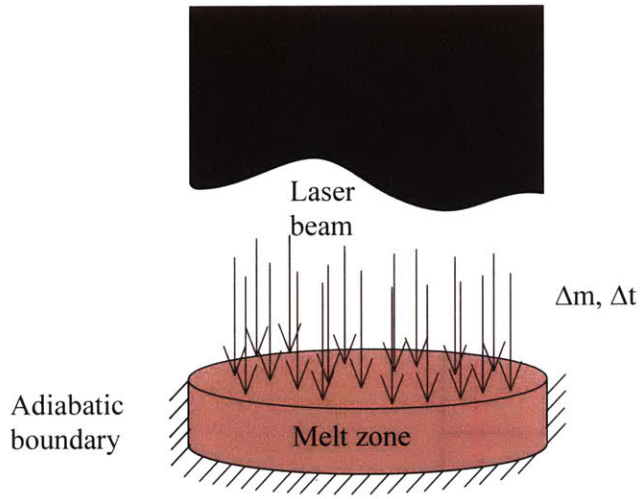

Figure IV.15 Schematic of adiabatic model

Through energy balance between released energy from laser and absorbed energy within the powder material, equation 4.12 is derived and given below.

$$\Delta m\ C(T_{melt} - T_{initial}) + \gamma_{latent} = \eta P \Delta t \quad \text{Eq. 4.12}$$

Δm	- material processed
C	- heat capacity
T_{melt}	- phase change temp.
$T_{initial}$	- initial temperature
γ	- latent heat
η	- radiation absorptivity
P	- laser power
Δt	- heat transfer time scale

The left hand side of the equation denotes the minimum energy required to raise the temperature of the powder material and melt the material, and the right hand side of the equation denotes the energy deposited from laser to the melt region within heat transfer time scale Δt. Rearranging the equation, material process rate can be expressed independent of any relative geometry.

$$\left(\frac{dm}{dt}\right)_{adiabatic} = \frac{\eta P}{C(T_{melt} - T_{initial}) + \gamma_{latent}} \quad \text{Eq. 4.13}$$

The material process rate is directly proportional to laser power and inversely related to the temperature gap between phase change temperature and initial temperature.

To reach the theoretic maximum material process rate (i.e. adiabatic maximum fusion rate), energy received within the material needs to be used efficiently such that the affected material is heated to just fully melt. For simulation, material absorptivity is obtained from Tolochko et al. 2000 [55], thermodynamic properties for steel are obtained from bulk material property sheet.

Parameter	**Value**	**Reference**
Heat capacity [J/(kg-^{0}C]	510	[65]
Melting temperature [^{0}C]	1430	[65]
Plate temperature [^{0}C]	100 - 300	[66]
Latent heat [J/kg]	273,000	[67]
Laser material absorption rate	0.64	[55]

Table IV.2 Bulk parameters for steel SS 316L used in modeling

Various researchers reported processing rate in their studies to identify optimum operating parameters for powder bed fusion as well as to determine the mechanical properties of the printed parts. Processing rates directly reported and calculated from research data are collected in Table IV.3. In the selected cases, all the printed parts/samples have a high relative density (close to or greater than 99%) compared to bulk material. In the first three cases, functional parts were printed, and processing rate is calculated dividing the printed mass to build time. In other cases, cubic and pillar specimen were printed. When not directly reported, processing rate is calculated multiplying the layer depth, scanning speed and hatching distance.

University of Leuven conducted multiple experiments studying the processing rate and part quality of selective laser melting over the past decade. Kruth et al. [68] reported cases building a same test sample with ferrous material (stainless steel) on four SLM machines from different manufacturers in 2005, including EOS, Concept Laser, Trumph and MCP-HEK . Two of the tested machines operate with laser power of 200W, while the other two operate with 100W lasers. The test sample, shown in Figure IV.16, has the dimension of $50\times50\times9$ mm^3. The processing rate is then calculated by dividing the part volume by the reported production time. The rate ratio for all four tests are around 9% in regardless of the different laser power and machines involved. In a paper published in 2010, Kruth et al. [69] reported building high density stainless steel part with different scanning speed on Concept Laser M3 Linear machine. Laser power of 105W is deposited to scan the powder bed at different scanning speeds for different layer thicknesses. The efficiency rate for the maximum processing rate is 23%.

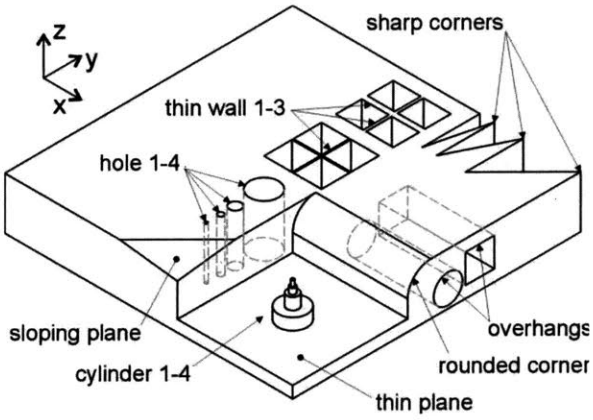

Figure IV.16 Benchmark model built and tested in KU Leuven [68]

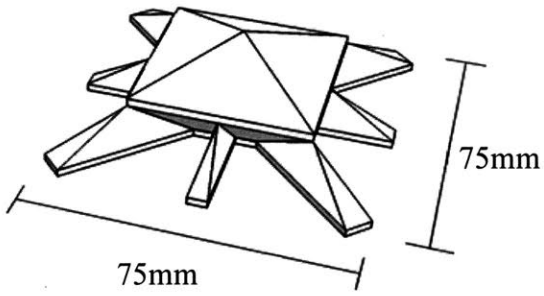

Figure IV.17 Test model built at Loughborough University [66]

In 2010, Baumers et al. [66] studied the energy consumption of building a test part shown in Figure IV.17. The experiments were done on an MTT SLM 250 machine with laser power of 200W. A single test part and six test parts were built in separate experiments to study the influence of the build volume. The processing rate is calculated dividing the part volume by reported production time. The average processing rate ratio is 12%.

Liu et al. 2011 [70] from Loughborough University studied relationship between particle size distribution and process parameter optimization. In the experiments, test specimens were built on a SLM-Realizer 100 machine equipped with a 50W laser. Processing rate was calculated by

multiplying the scanning speed with hatching distance and layer thickness. The processing rate ratio ranges from 10% to 19% depending on different scanning speed and hatching distance parameters.

Yasa et al. conducted research to investigate the influence of laser remelt on density, surface quality and microstructure of selective laser melting steel 316L powders in 2011 [71]. The experiments were carried out on a Concept Laser M3 machine, with a scanning speed of 380 mm/s, laser power of 105W and hatching distance of 125 μm. The processing rate is therefore calculated to be 4.1 cm^3/hr, resulting the processing rate ratio to be 14%.

In a study to increase processing rate of selective laser melting, Schleifenbaum et al. 2011 [16] built and tested with a customized SLM machine equipped with a 1000 W laser. They applied skin-core scanning strategy to maintain geometric accuracy and good surface finish while improving the processing rate. The core of the built part is scanned at a higher speed with laser power of 1000 W, resulting in a processing rate of 16.8 cm^3/hr. The skin, on the other hand, is scanned at a relatively low speed with laser power of 350W. The processing rate for the skin is 3.0 cm^3/hr. The rate efficiency for skin scanning is therefore lower than all other reported cases.

In a study to determine process parameters that generates high density parts, Kamath et al. designed experiments to print 10mm×10mm×7mm pillar with varying power and scanning velocity [72]. Their study shows that high density parts could be produced with higher power (250 to 400W) over a range of scanning velocity. The processing rate is calculated to be 12.9 to 23 cm^3/hr, leading to a rate ratio of 19% to 23%

Sun et al. also studied the possibility of improving build rates with higher laser power for selective laser melting stainless steel 316L powder [73]. In their study, a SLM 250HL machine is used as the platform. The machine is equipped with a 400 W laser. In the experiment, laser power is fixed at 380 W with a beam diameter around 80 μm; powder layer thickness was also fixed at 50 μm; scanning velocity and hatching space are varied to determine the optimum settings. Processing rate is then calculated to be 13.5 cm^3/hr, which leads to a rate ratio of 12%.

	Machine	Material	P (W)	Measured rate (ccm/ hr)	Rate ratio	Density Ratio (vs bulk material)	Reference
Functional Parts (calculation includes recoating time)	AM 250	SAE 316L	200	7.0	12%	N\A	Baumers et al. 2010
	Trumph (not specified)	SS 316	200	5.0	9%	98.7%	Kruth et al. 2005
	MCP-HEK (not specified)	SS 316	100	2.6	9%	99.1%	Kruth et al. 2005
Pillars, cubes, specimen (data chosen to ensure >99% printed	Modifed Trumaform LF250	Steel 1.2343,1.2709,1.4404	1000	60.5	21%	> 99%	Schleifenbaum et al. 2011 and Bremen, Meiners, and Diatlov 2012
	Concpet Laser M2	SS 316L	250 - 400	12.9 - 23.0	19 - 23%	99.13 - 99.41%	Kamath et al. 2014

density, calculation includes hatching distance, powder depth and scanning velocity)	SLM 250 HL	SS 316L	380	13.5	12%	99.1 - 99.2%	Sun et al. 2016
	Modifed Trumaform LF250	Steel 1.2343,1.2709,1.4404	300	10.8	13%	> 99%	Schleifenbaum et al. 2011 and Bremen, Meiners, and Diatlov 2012
	Concept Laser M3	SS 316L	105	6.8	23%	98%	Kruth et al. 2010a
	Concept Laser M3	SS 316L	100	5.2	18%	98.80%	Kruth et al . 2012
	Customed SLM machine	SS 316L	105	4.1	14%	> 99%	Yasa et al. 2011
	SLM-Realizer 100	SS 316L	50	1.4 - 2.9	10 - 19%	99.45 - 99.93%	Liu et al. 2011

Table IV.3 Processing rate measured by different researches (or calculated from research data) and corresponding rate ratio efficiency when divided by adiabatic processing rate

To compare process rate reported from research and the adiabatic maximum fusion rate, the rate ratio is plotted against laser power in the relative cases for stainless steel powder as shown in Figure IV.18. With machines from different manufacturers, the ratio is on average 15% regardless of laser power. Figure IV.18 shows that there has been no clear improvement in process efficiency over the last ten years. In general, processing rate ratio in cases with functional part printed is lower than in cases where simple specimen were printed. This is because of the different calculation methods mentioned above. The processing rate for printing test specimens were calculated neglecting powder recoating, machine warming up phases due to lack of information. It is therefore higher than the processing rate calculated for functional parts which takes these two factors into account.

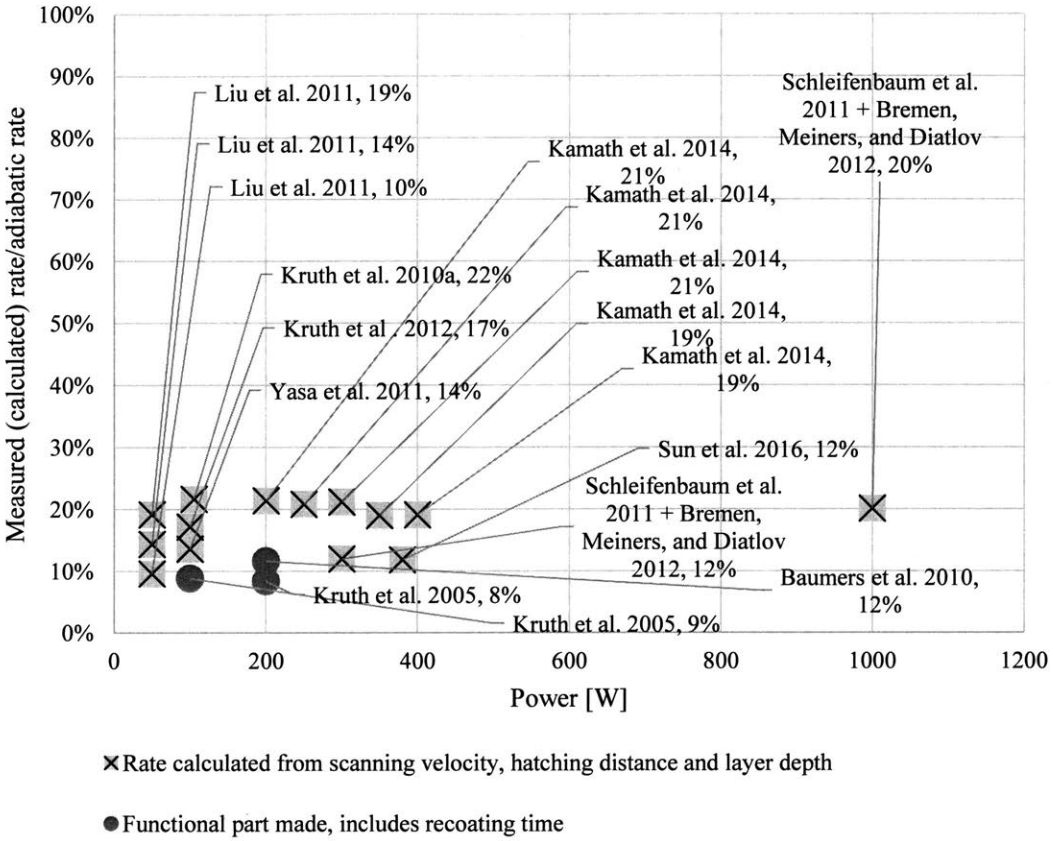

Figure IV.18 Ratio of actual rate limits over adiabatic rate limits vs laser power (SS 316L)

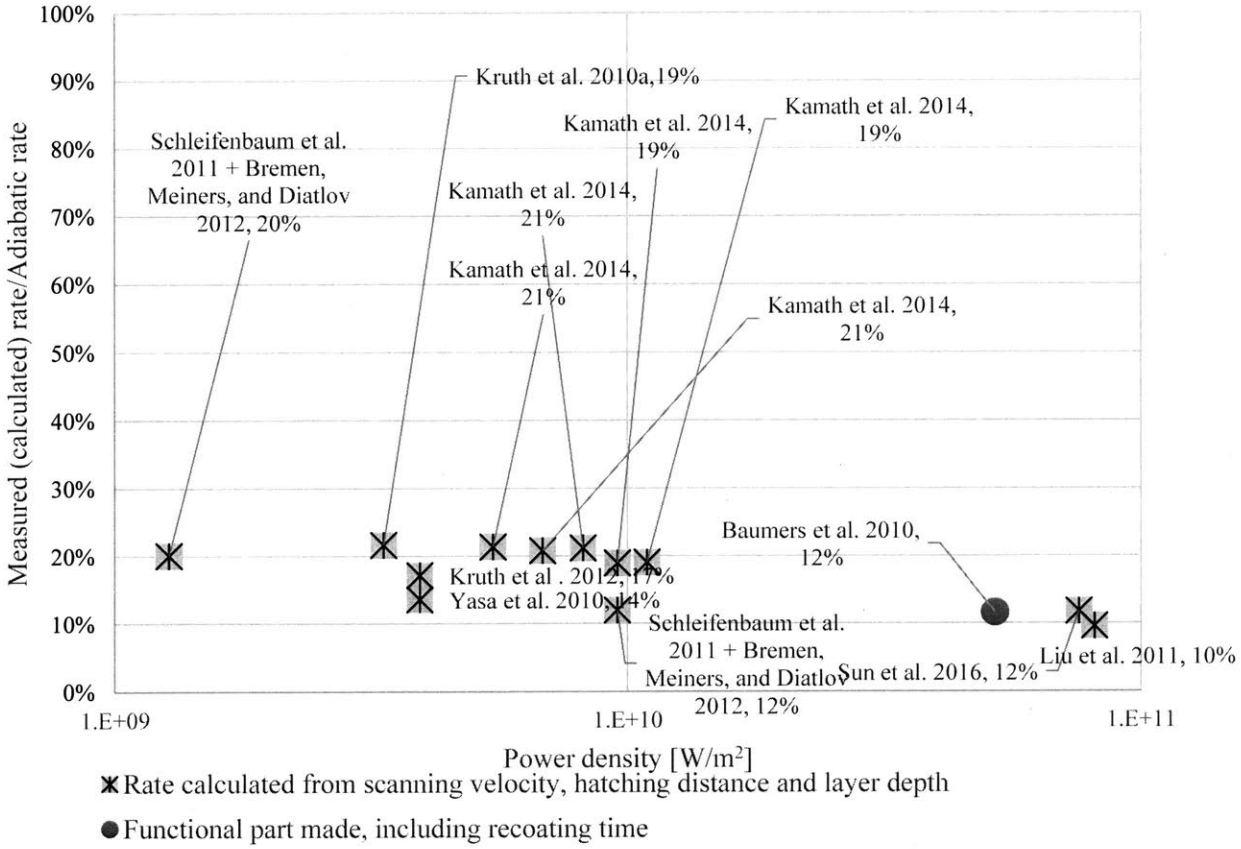

Figure IV.19 Ratio of actual rate limits over adiabatic rate limits vs laser power density (SS 316L)

When plotted against power density as shown in Figure IV.19, the ratio of measured rate divided by the adiabatic rate shows a clear drop at higher power densities. Note that, in the case of applying 1000W laser reported by Schleifenbaum et al. 2011, the laser power density appears to be on the lower end among all the cases reviewed here. At higher laser power density, evaporation occurs at the melt pool surface more easily, and this could restrict the processing window and at the same time lower the energy efficiency.

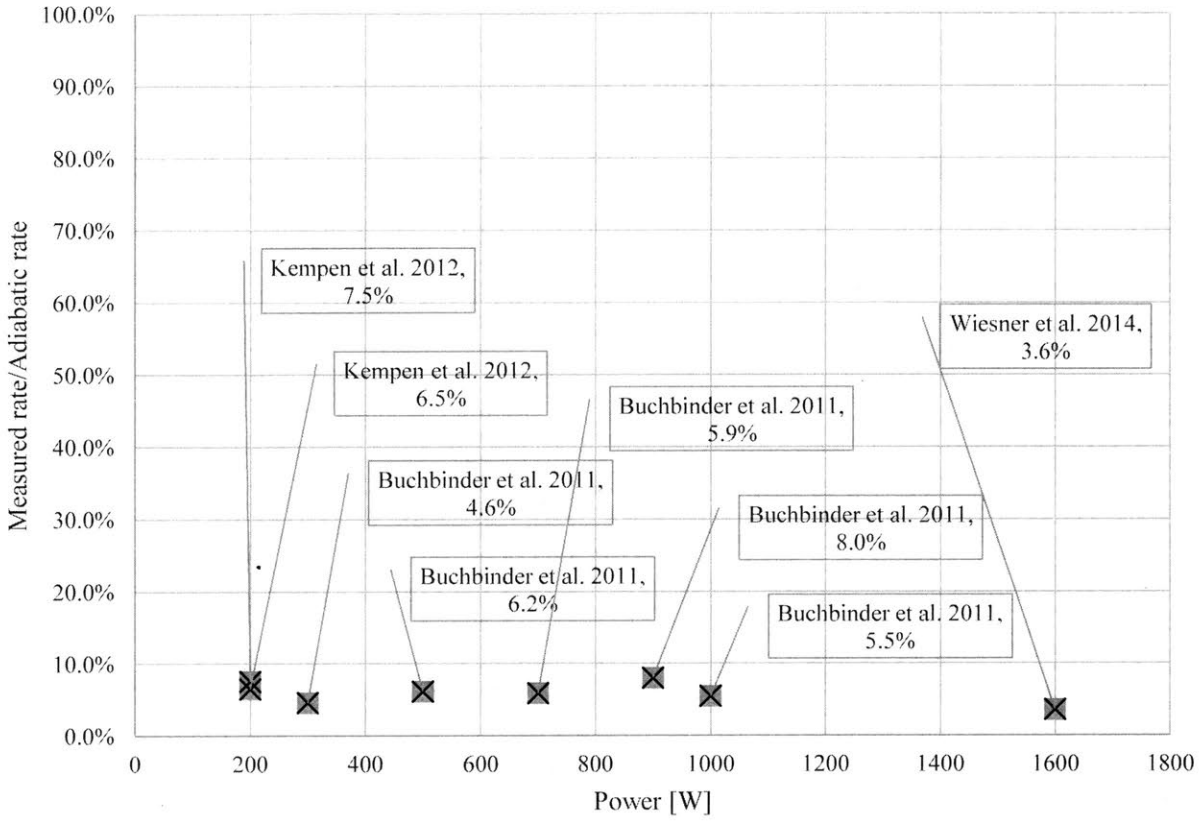

Figure IV.20 Ratio of actual rate limits over adiabatic rate limits vs laser power (AlSi10Mg)

Kempen et al. 2012 studied the mechanical properties of selective laser melting AlSi10Mg powder [74]. In their research, a 200W Concept Laser M1 machine was used to print the aluminum alloy powder at 1400 mm/s and 1200 mm/s scanning velocity. The density of the printed parts were measured to be 98.5%. Buchbinder et al. 2011 reported their study on applying high power laser to print AlSi10Mg powder [16]. In their study, laser power was varied from 300W to 1000W. With fast scanning velocity and suitable hatching distance, the density of the printed specimen could be kept over 99% over the range of power. Wiesner et al. 2014 reported a case in which four 400W lasers were used to print AlSi10Mg powder at the same time [75]. The measured rates were plotted against adiabatic rate which is calculated with parameters listed in Table IV.4. The ratio is lower at around 5% compared to 15% for stainless steel SS316L powders. One possible cause is the high reflectivity of aluminum at molten state. Although the absorptivity for aluminum powder could be as high as 62% [76], once the surface is molten, the absorptivity could drop drastically, which would increase the required energy to ensure fully melting the powder layer.

Parameter	Value	Reference
Heat capacity [J/(kg-^{0}C]	963	[57]
Melting temperature [^{0}C]	613	[57]
Plate temperature [^{0}C]	100 - 300	[66]
Latent heat [J/kg]	389,000	[57]
Laser material absorption rate	0.62	[76]

Table IV.4 Bulk parameters for AlSi10Mg used in modeling

To understand the causes of this low ratio (around 15%), an investigation beyond adiabatic modeling is needed. While melting the material, heat also dissipates to adjacent material as well as the surroundings, which is not captured by equation 4.13. In addition, scanning parameters (speed, hatching distance, powder layer thickness, etc.) are constrained in order to have good mechanical properties (density, strength, etc.) and desired microstructure.

4.4. One-dimension constant heat flux model

Modeling the melting phenomenon to study the heat transfer can be complex. It is often difficult to obtain analytical solutions, therefore researchers have applied numerical methods to simulate the processes. To understand the significance of physical property variation and scanning parameters in heat transfer, however, simple models with analytic solutions can be helpful.

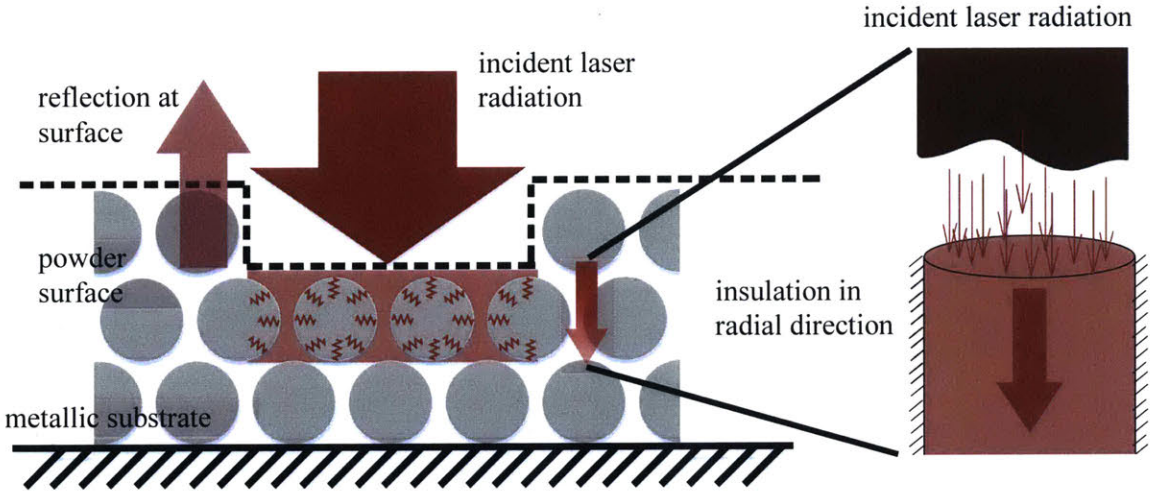

Figure IV.21 Schematic of one-dimension constant heat flux model

A one-dimension constant heat flux model is shown in Figure IV.21. The model consists of three stages: volumetric heating, capillary penetration, and one-dimension heat transfer. In the first stage, 64% of incident laser energy is absorbed within the powder bed. The received energy

decays exponentially with thickness. Before the powders are melted, the effective thermal conductivity is around 0.4 W/mK. Since the thermal conductivity of bulk material is two orders of magnitude larger, the volumetric heating stage can be viewed as adiabatic. At power above 50 W, the powder surface would reach melting temperature within very short time (0.01 ms) compared to laser scanning time (1 ms). After the surface layer is molten, the process enters the second stage in which the molten material fills in the pores in the layer underneath due to capillary pressure. In the third stage, 40% of incident laser energy is absorbed at the surface. The absorbed heat is then assumed to transfer in and only in depth direction, which is governed by Fourier's law. The second and third stages will loop until the bottom layer is reached.

$$\rho C \frac{\partial T}{\partial t} = k\nabla^2 T = k\frac{\partial^2 T}{\partial z^2} \quad \text{Eq. 4.14}$$

To model the heat transfer, laser beam energy is assumed to be uniformly applied at the top surface of the designated region at constant power. Heat transfer to material outside the laser focused zone is neglected due to low thermal conductivity. Since radial heat transfer is not interested in this model, the powder liquid mixture is treated with uniform property. All the powder material is assumed to be at uniform average initial temperature. With these boundary condition, the temperature field in the material can be solved.

$$\Delta T(z,t) = \frac{\eta P}{Ak}\left(\sqrt{\frac{4\alpha t}{\pi}} e^{-\frac{z^2}{4\alpha t}} - z\,Erfc\left(\frac{|z|}{\sqrt{4\alpha t}}\right)\right) \quad \text{Eq. 4.15}$$

k - thermal conductivity
A - laser focus spot
α - thermal diffusivity
Erfc - Complimentary error function
η - radiation absorptivity
P - laser power
t - time elapsed since heat flux applied

The physical properties used in the modeling are taken from bulk material properties for stainless steel 316L, latent heat is coupled into heat capacity by averaging over the temperature difference.

Parameter	Value	Reference
Heat capacity [J/(kg-^{0}C]	510	[65]
Melting temperature [^{0}C]	1430	[65]
Thermal conductivity [W/(m-^{0}C)]	20	[65]
Latent heat [J/kg]	273000	[65]
Laser material absorption rate	0.4	[55]
Layer thickness [μm]	50	
Laser focus spot diameter [μm]	200	

Table IV.5 Stainless steel 316L parameters used in modeling

The processing window for selective laser melting in the model is such that the temperature of bottom surface is higher than melting temperature and the temperature of top surface is higher than melting temperature but lower than vaporization temperature. The results are shown in Figure IV.22 below. Velocity is calculated dividing the diameter of laser focus by elapsed time to reach a target temperature. The plot is divided into five different regions:

I: laser is moving too fast, all the material remains solid phase

II: laser is moving too fast, top layer material melted, bottom layer remains solid

III: process window where all the material are melt with no vaporization

IV: laser moves slow with given power, the top surface material starts vaporization while the bottom surface is melted

V: laser moves slow with given power, the top surface starts vaporization before bottom surface starts melting

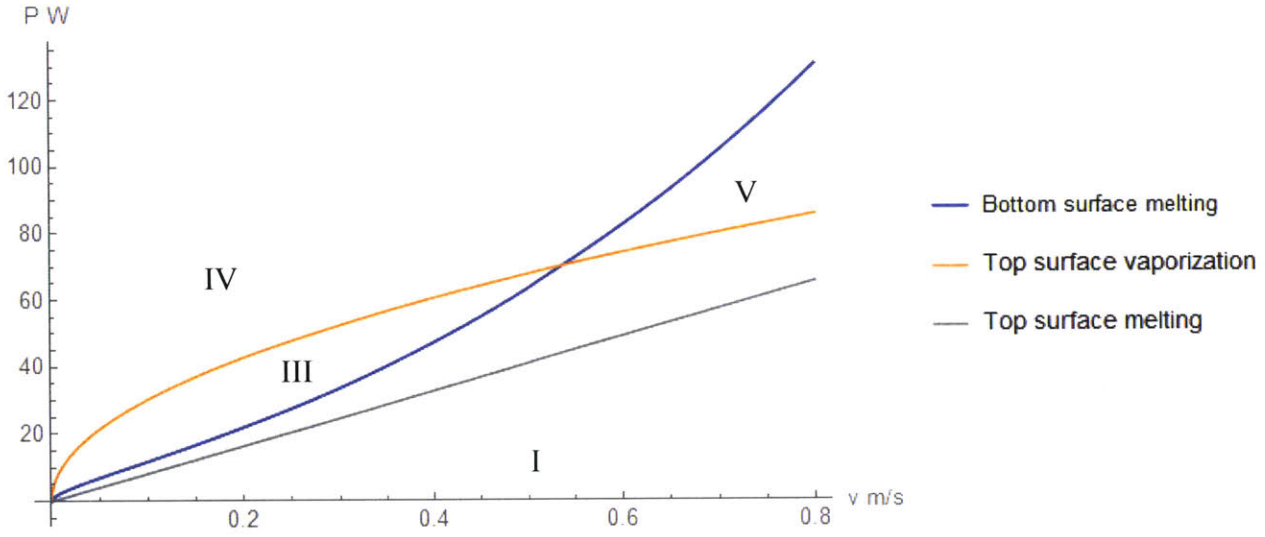

Figure IV.22 Processing window for one-dimension heat transfer

To achieve the fastest processing rate, parameters needs to be optimized such that the bottom surface is just molten. Due to the heat transfer mechanism, the surface material is heated over melting temperature when the bottom surface melts. As a result excessive heat is absorbed in stage three during the process compared to the theoretic adiabatic limit. Taking into account the absorbed energy in the first stage, the adjusted processing window can be calculated with equation 4.16, where ΔE is the absorbed energy in the first stage. The result is plotted together with adiabatic limit in Figure IV.23. The extra energy needed due to heat transfer is highlighted with shadow.

$$P_{adj} = P + \frac{\Delta E}{t} \quad \text{Eq. 4.16}$$

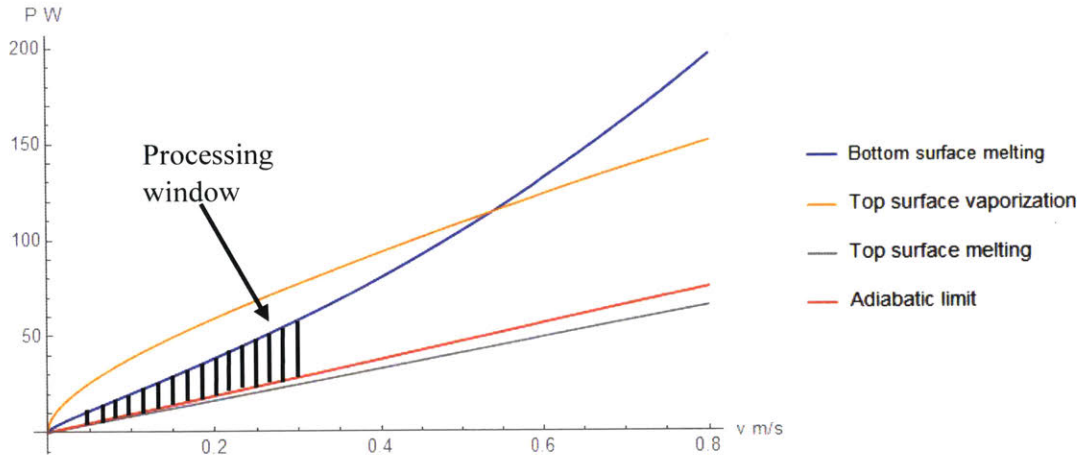

Figure IV.23 Adjusted processing window for one-dimension modeling of selective laser melting

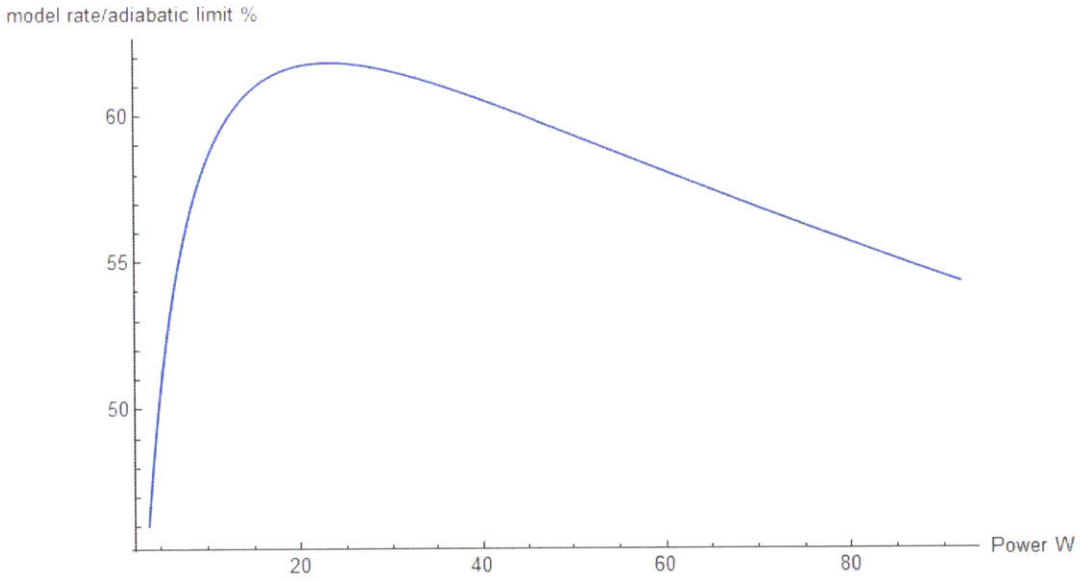

Figure IV.24 Ratio of fastest one-dimensional heat transfer model rate limits over adiabatic rate limits vs laser power

The ratio of fastest one-dimensional heat transfer model rate limits over adiabatic rate limits is plotted against incident power in Figure IV.24. The rate efficiency is related to overheating, which is directly related to the temperature difference between top and bottom surface. Generally, higher laser power leads to larger temperature difference for the same heating time. Longer heating time, i.e. slower scanning speed, on the other hand, leads to smaller temperature difference for the same laser power. At low power and low scanning velocity, temperature difference mainly depends on laser power since the heat transfer rate beneath the surface tends to stabilize towards the wall heat flux after a long time. At higher power and high scanning velocity, temperature difference depends on velocity because heat transfer rate decreases beneath

the surface before reaching steady state. As a result, process efficiency increases at low power range, and decrease at high power range.

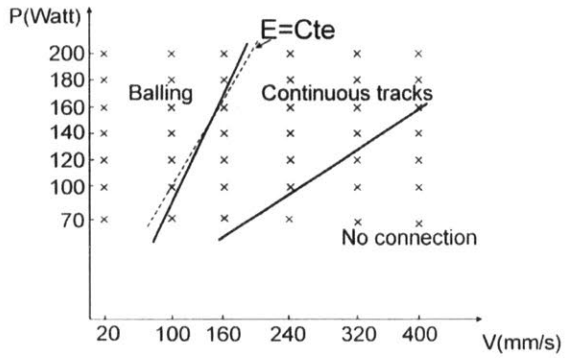

Figure IV.25 Experimental processing window for ferrous material [53]

The processing window from the model is narrower compared to experimental research studies (Figure IV.25). One potential cause is parameter settings including layer depth, focus diameter, etc. For example, the processing window grows narrower with increasing layer thickness since it takes longer for heat to penetrate deeper as Figure IV.23 shows. On the other hand, laser beam energy density profile is not uniform, but often close to a Gaussian distribution. Heat transfer in radial direction would cause large temperature gradient, which will in turn limit the processing rate. Since the bottom substrate and adjacent track are usually processed, the heat loss to the surrounding material can be substantial. The heat affected zone therefore can be quite large despite that the melt pool size is relatively small [77].

4.5. Three-dimension constant heat flux model

4.5.1 stationary constant heat flux heat transfer model

To study the effect of radial heat transfer during the process, a three-dimensional heat transfer model is proposed. Similar to section 4.4, the process can be divided in three sub stages, i.e. volumetric heating, capillary penetration, and three-dimensional heat transfer. The model will focus on the third stage for simplicity. A stationary constant heat flux heat transfer model is first considered. The laser heating is modeled as a constant uniform plane heating source as shown in the schematic. The powder surface is assumed to be adiabatic with no heat transfer to the environment above it.

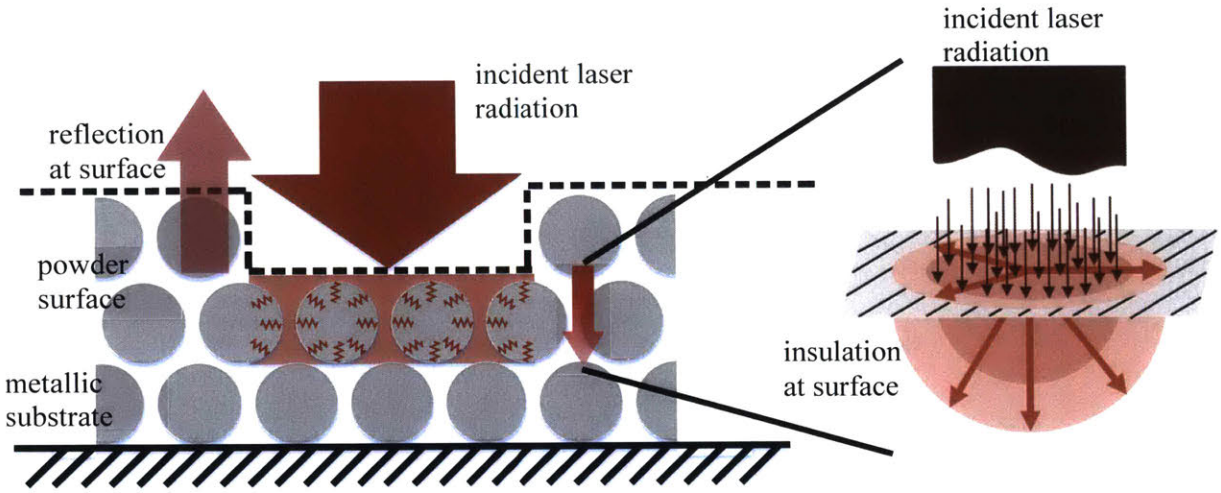

Figure IV.26 Schematic of stationary three-dimensional constant heat flux model

The model for plane heat source can be integrated from point heat source solution of the heat equation (Green's function) in the semi-infinite solid. G(x,y,z,t) represents the temperature response of an instantaneous point heat source at time t.

$$G(x,y,z,t)=\frac{1}{(4\pi\alpha t)^{3/2}}e^{-\frac{x^2+y^2+z^2}{4\alpha t}} \quad \text{Eq. 4.17}$$

The temperature field at any point for a continuous plane heat source can be obtained through the integration shown below. Function F denotes the initial temperature field, which in our case is uniform.

$$\Delta T_{continue}(x,y,z,t)=\int dt\iint_A G(x-x',y-y',t)F(x,y,z,0)dA'$$

$$\Delta T_{continue}(x,y,z,t)=\int dt\iint_A \frac{1}{(4\pi\alpha t)^{3/2}}e^{-\frac{(x-x')^2+(y-y')^2+z^2}{4\alpha t}}dx'dy' \quad \text{Eq. 4.18}$$

The above integration does not have an analytic solution, but can be simplified to:

$$\Delta T_{continue}(x,y,z,t)=\frac{\eta P}{4\pi Ak}\iint_A \frac{1-Erf(\frac{R}{\sqrt{4\alpha t}})}{R}dA' \quad \text{Eq. 4.19}$$

$$R=\sqrt{(x-x')^2+(y-x')^2+z^2}$$

k	- thermal conductivity
C	- heat capacity
α	- thermal diffusivity
Erfc	- complimentary error function
η	- radiation absorptivity

P - laser power
t - time elapsed since heat flux applied

Same parameters in one-dimensional heat transfer modeling are used in the numerical simulation. The processing window for selective laser melting in the model is determined such that the highest temperature of bottom surface is higher than melting temperature and the highest temperature of top surface is higher than melting temperature but lower than vaporization temperature. This ensures interlayer bonding as the substrate is partially re-melted. The minimum power requirement, however, could be underestimated since only the highest temperature point (center) is considered. The results are shown in Figure IV.27 below. Velocity is calculated dividing the diameter of laser focus by elapsed time to reach a target temperature.

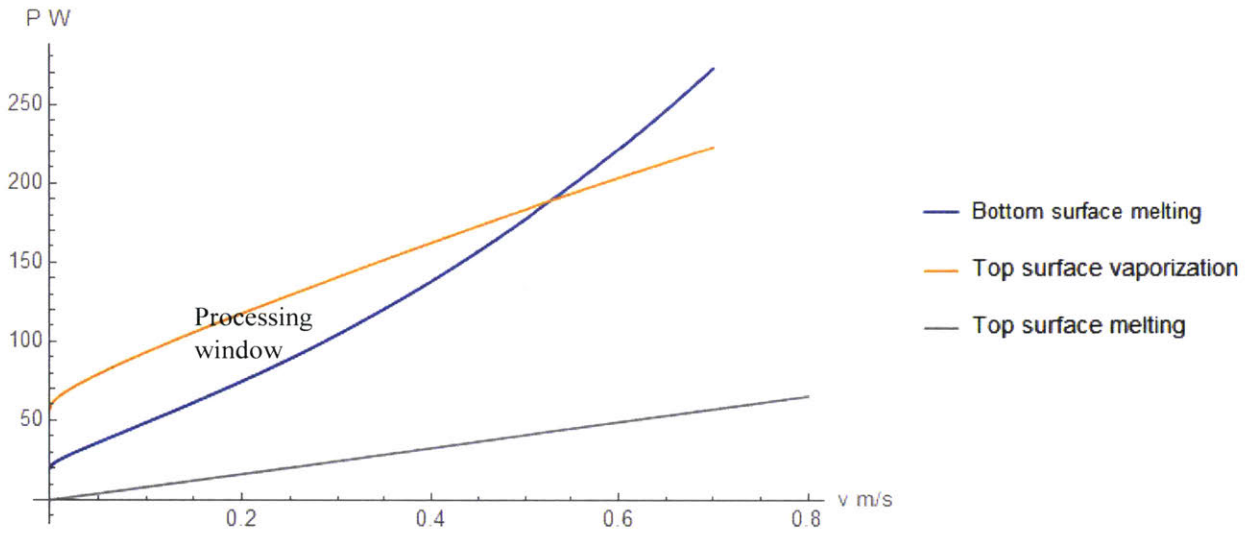

Figure IV.27 Processing window for three-dimension heat transfer

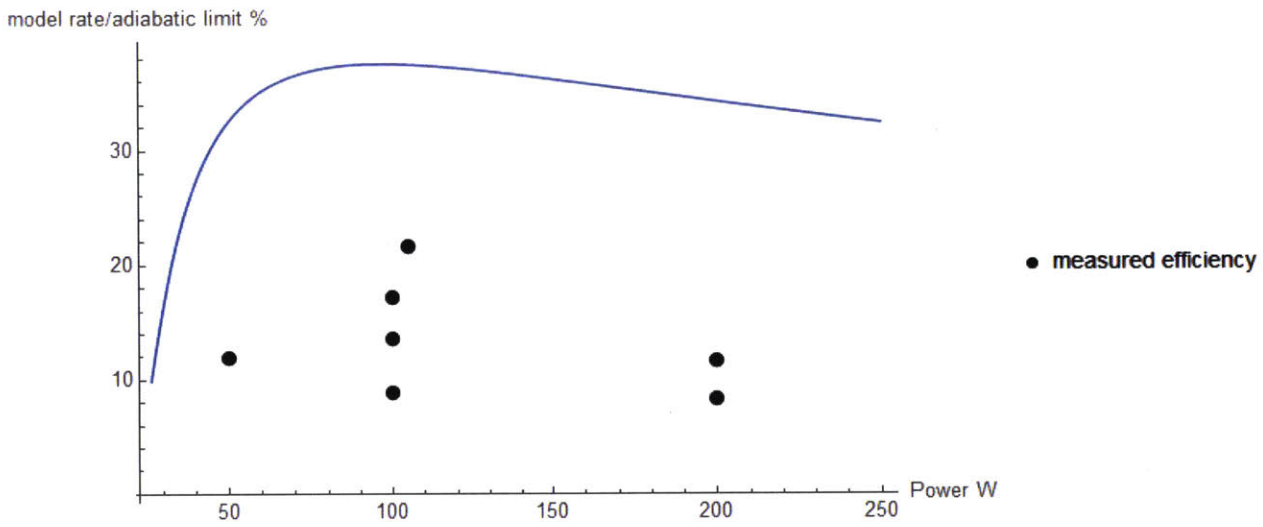

Figure IV.28 Ratio of fastest three-dimensional heat transfer model rate limits over adiabatic rate limits vs laser power

Compared to the results of one-dimensional heat transfer model, higher energy is required to process material at the same rate. To achieve the fastest processing rate, power and velocity needs to be optimized to follow the bottom melting curve in Figure IV.28. The shape of the efficiency plot is similar to that from one-dimensional heat transfer model. The magnitude of efficiency is smaller than what's predicted the previous model.

In this model, heat transfer is assumed to be isotropic in all directions (including radial direction) within the powder layer. In practice, however, powders exist in front of and on one side of the scanning direction. Heat transfer is negligible in these two directions due to the low thermal conductivity. As a result, laser power requirement is overestimated, efficiency is underestimated in this model. The plot shows, if anything, heat conduction is one of the limiting factors for processing rate improvement. This is because there are other factors limiting the efficiency, which are not covered in this model.

4.5.2 moving constant heat flux heat transfer model

During selective laser melting process, laser beam is constantly moving while delivering energy to the powders. A moving constant heat flux heat transfer model will better capture the phenomenon. Previous analysis is done with stationary models because of its simplicity in determining the position of the maximum temperature. The laser heating is modeled as a moving uniform plane heating source with a constant speed. The powder surface is assumed to be adiabatic.

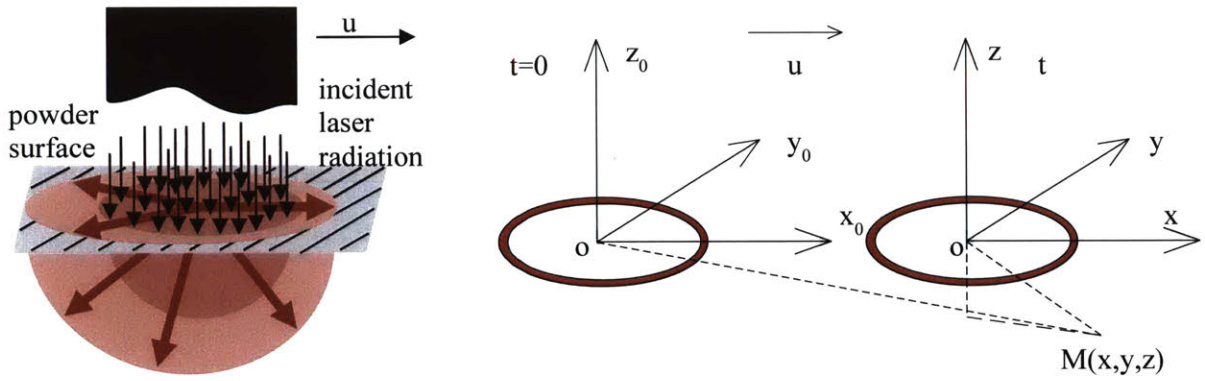

Figure IV.29 Schematic of moving three-dimensional constant heat flux model

Carslaw and Jaeger [38] solved the heat equation for a moving point heat source. In the solution equation, τ is the elapsed time since the initiation of the heat source, u is the speed of the heat source. The solution gives the temperature of a point M within the moving coordinates, taking into account all the heat transfer elapsed in time τ.

$$G_{moving}(x,y,z,\tau)=\frac{1}{(4\pi\alpha\tau)^{3/2}}e^{-\frac{(x+u\tau)^2+y^2+z^2}{4\alpha\tau}} \quad \text{Eq. 4.20}$$

To obtain the temperature field of a plane source in the moving coordinates, equation 4.20 is integrated over a circular area as shown in equation 4.21. Function F denotes the temperature field when the heat source starts moving, which in our case is uniform.

$$\Delta T(x,y,z,t)=\int d\tau\iint_A G_{moving}(x-x',y-y',\tau)F(x,y,z,0)dA'$$

$$\Delta T(x,y,z,t)=\int d\tau\iint_A \frac{1}{(4\pi\alpha\tau)^{3/2}}e^{-\frac{(x+u\tau)^2+y^2+z^2}{4\alpha\tau}}dx'dy' \quad \text{Eq. 4.21}$$

It can be shown that the integration can be simplified into:

$$\Delta T(x,y,z,t)=\frac{\eta P}{8\pi Ak}\iint_A \frac{e^{-\frac{u}{2\alpha}(x-x')}}{R}\left(e^{\frac{Ru}{2\alpha}}Erfc\left(\frac{R}{\sqrt{4\alpha t}}+\frac{u\sqrt{t}}{\sqrt{4\alpha}}\right)+e^{-\frac{Ru}{2\alpha}}Erfc\left(\frac{R}{\sqrt{4\alpha t}}-\frac{u\sqrt{t}}{\sqrt{4\alpha}}\right)\right)dA' \quad \text{Eq. 4.22}$$

$$R=\sqrt{(x-x')^2+(y-x')^2+z^2}$$

k	- thermal conductivity
A	- heat capacity
α	- thermal diffusivity
Erfc	- complimentary error function
η	- radiation absorptivity
P	- laser power
t	- time elapsed since heat flux applied

The temperature field will approach steady state as elapsed time becomes longer. Taking t as infinity, the equation can be further simplified into equation 4.23, although there is no analytic solution.

$$\Delta T(x,y,z,t) = \frac{\eta P}{4\pi Ak}\iint_A \frac{e^{-\frac{u}{2\alpha}(x-x'+R)}}{R}dA' \quad \text{Eq. 4.23}$$

$$R = \sqrt{(x-x')^2+(y-x')^2+z^2}$$

Same parameters in one-dimensional heat transfer modeling are used in the numerical simulation. For 120W laser power at scanning speed of 0.2 m/s, the temperature profile on the top surface is shown in Figure IV.30. The temperature field is symmetric about x axis. The maximum temperature on the surface is shifted towards the tail of laser melting track. It is usually close to the edge of the laser spot on the x axis.

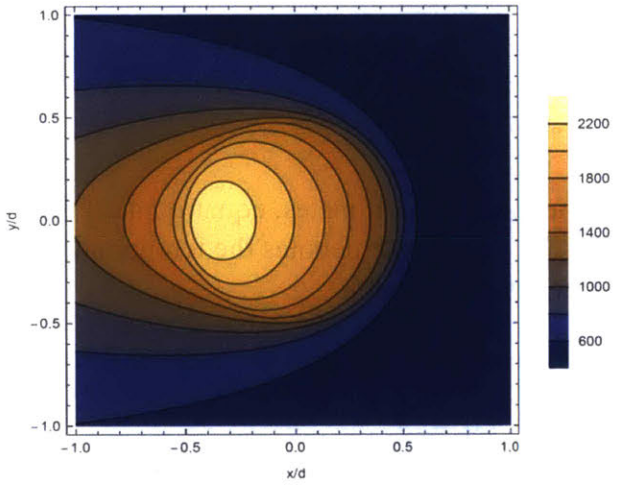

Figure IV.30 Isothermals at surface at power of 120W and scanning velocity of 0.2 m/s, d is the laser spot diameter

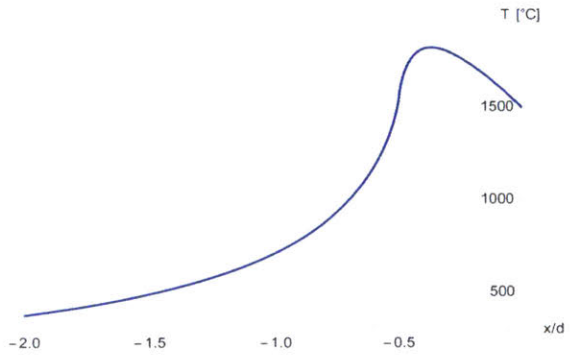

Figure IV.31 Temperature field along x axis at top surface for moving heat source at power of 100W and scanning velocity of 0.2 m/s, d is the laser spot diameter

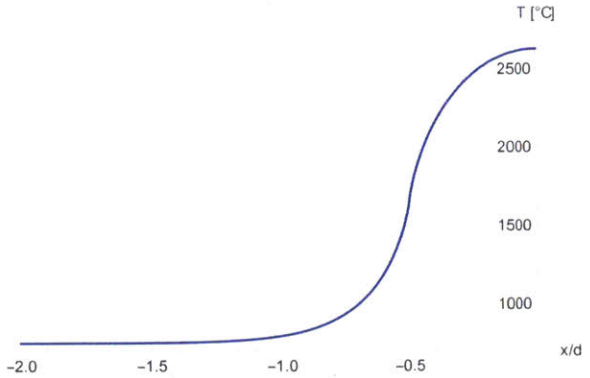

Figure IV.32 Temperature field along x axis at top surface for stationary heat source at power of 100W and scanning velocity of 0.2 m/s, d is the laser spot diameter

The maximum temperature on the top surface from the moving heat source model is slightly smaller than that from the stationary heat source model as can be seen from comparison of Figure IV.31 and Figure IV.32. The moving heat source model will therefore have a lower processing efficiency than stationary heat source model when compared to the adiabatic limit.

5. Additional limiting factors

The models discussed in the previous section shows that heat transfer is one of the major limitations to the current processing rate. Excessive energy deposited into the melt pool induces great temperature gradient. A gradient in surface tension develops due to the temperature dependence of the surface tension. It is observed that, a convective flow called Marangoni flow occurs in the melt pool, which induces thermal instability [78]. The dimensionless Marangoni number Ma is defined by equation 4.24, in which $\frac{d\gamma}{dT}$ is the surface tension gradient, $\frac{dT}{dx}$ is the temperature gradient, L is the characteristic length of molten pool, μ is the viscosity and α is the thermal diffusivity.

$$Ma = \frac{d\gamma}{dT}\frac{dT}{dx}\frac{L}{2\alpha\mu} \quad \text{Eq.4.24}$$

Marangoni number could be regarded surface tension forces divided by viscous forces. When the Marangoni number is sufficiently large, convection within the melt pool will induce instability which in turn affect the mechanical property of the printed part [79]. As described in the previous section, the temperature at the center of the melt pool is much higher than at the perimeter. Depending on surface tension gradient with respect to temperature, the direction of fluid movement could be determined as shown in Figure IV.33.

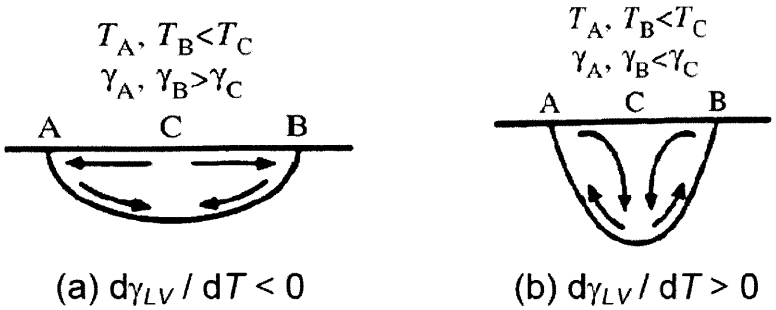

Figure IV.33 Schematic presentation of Marangoni convection in a melt due to the presence of a surface tension gradient [79]

Another main limiting factor on processing rate is the phenomenon of evaporation, especially for high power density situations. As illustrated in Figure IV.27, at higher power density (200W, 200μm diameter) the top surface of the melt pool would start evaporating before the melt pool reaches the bottom of the layer being printed. Evaporation increases the possibility of voids in the consolidated material, and it in turn reduces the density of the printed parts. Another effect of evaporation is the generation of recoil pressure onto the melt pool. The recoil pressure would cause melt pool movement in both depth and radial direction. The movement in the depth direction could enhance the melting with deeper melt pool penetration. However, it is also very likely that the movement forms melt pool instability [80]. The density and chemical composition could therefore be influenced. In addition, the formation of vapor on top of the melt pool would affect the absorption of laser energy by the melt pool. To further study the phenomenon during laser melting metal powder material, evaporation and Marangoni convection needs to be concerned during modeling such that the model would be more accurate.

V. Energy Consumption of Additive Manufacturing (powder bed fusion)

While additive manufacturing technology has been developed over the years, powder bed fusion is the closest to be applied to industrial manufacturing practice. Powder bed fusion process stands out among all the additive manufacturing technologies because its ability to produce functional parts with unique geometry with acceptable precision and accuracy prior to post processing. Electricity consumption during the build phase is reported to be on the order of 100 MJ/kg for metal powder bed fusion processes [76] [26]. Telenko et al. reported the electricity consumption for powder bed fusion process with nylon powders to be on the same order as metal processes [18].

The lifecycle energy consumption for products made with metal powder bed fusion process consists of energy consumed during five different phases: material production, manufacturing, transport, use phase and end of life. This chapter will focus on energy consumption in material production and manufacturing phases which directly relates to the production.

1. Energy consumption during material production

As mentioned in section 2.1.1., the powder material used in metal powder bed fusion processes are usually fabricated through gas or water atomization method which has been around for more than 40 years. During the process, metal feedstock is first melted and then forced through a nozzle where high velocity air, N_2, He or Ar gas impinges onto the flowing melt and breaks it up into droplets. The energy consumption of material production can therefore be divided in two parts: energy to melt raw material, energy to break down molten stream and to form particles.

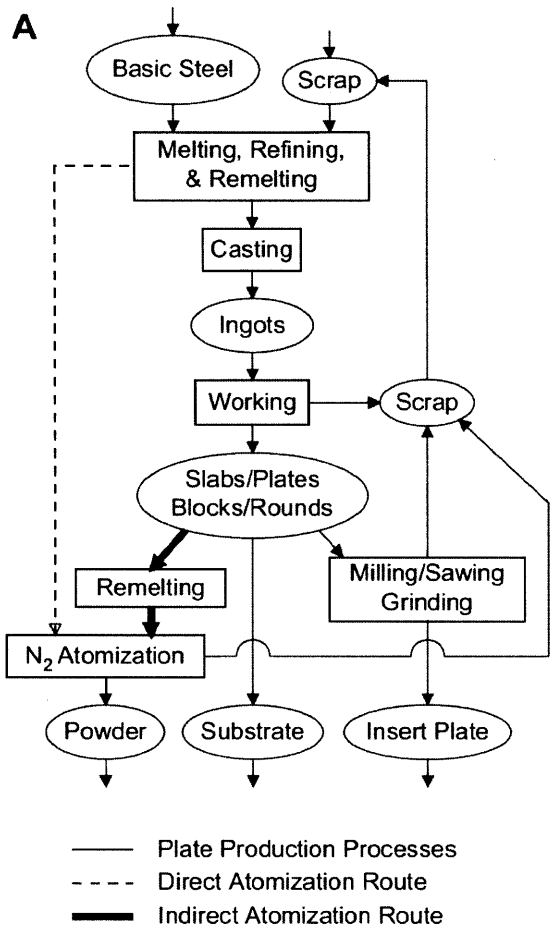

Figure V.1 Raw material production processes for powder fabrication [81]

Depending on the raw material used during the atomization process, the powders can either be produced directly from molten material, or indirectly from melting commercial metal plates/slabs. The difference of these two methods is shown in the flow chart in Figure V.1. The indirect method would therefore consume more energy than the direct method. Apart from the melting operations, the energy consumption for atomizing molten tool steel has been estimated to be on the order of 1 MJ/kg [82]. The total energy consumption for tool steel is reported to be 16 MJ/kg for direct atomization, and 27 MJ/kg for indirect atomization respectively [81] as can be seen in Figure V.2. The energy consumption for atomizing molten material consists of 4 to 6% of the total process energy consumption.

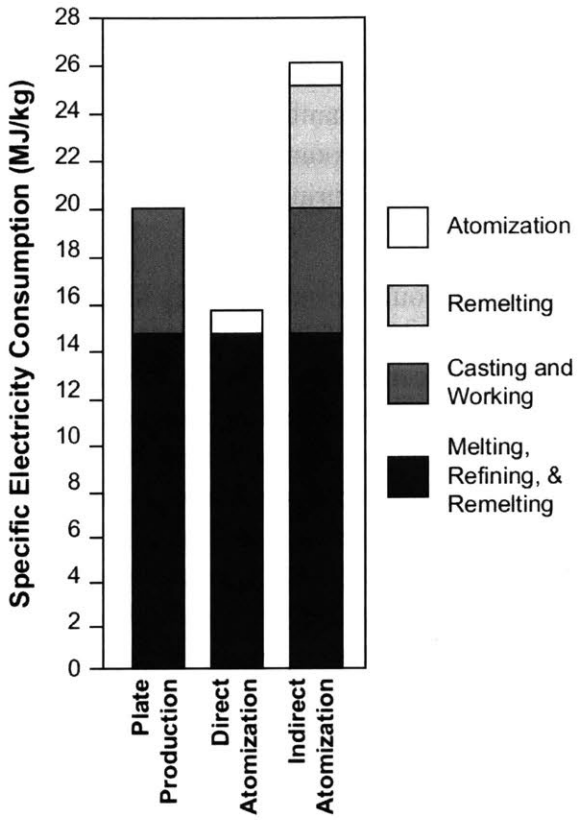

Figure V.2 Specific Energy Consumption of material production pathways [81]

Morrow et al. 2006 considered the energy consumption directly related to the gas atomization process for making tool steel powders (~ 20 MJ/kg). The energy required is one order smaller than the energy consumption in metal powder bed fusion processes (~ 200 MJ/kg).When considering a bigger boundary, the embodied energy of material and consumables during the gas atomization process could be substantial. For example the embodied energy of iron is estimated to be around 25 MJ/kg, but the embodied energy of aluminum is around 210 MJ/kg which is comparable to the energy consump tion in the metal powder bed fusion process [83]. Moreover, to maintain the inert gas atmosphere and high speed gas stream, large amount of inert gas is needed during the process. Take argon as an example, although lacking data on its embodied energy, estimates could be made with the production energy of argon through cryogenic distillation which is reported to be 5.4 MJ/kg [84] [65]. Neikov et al. reported the gas flow rate of 0.6 m^3/kg metal processed in atomization of Nickel alloy [86]. As a result, estimated production energy of argon used during the atomization process is calculated to be 5.8 MJ/kg metal powder produced. In addition, the gas to melt mass ratio for gas atomization process varies according to different material type and size requirement. Depending on different material, the significance of energy consumed during material production could appear to be substantial when considering the overall energy consumption.

2. Energy consumption during manufacturing

A metal powder bed fusion process typically experiences three different stages: preheating, building and cooling down. Depending on the material, the building chamber is either kept at an elevated temperature (~250 °C, e.g. AlSi10Mg), or slightly above the room temperature (~50 °C, e.g. SS 316L). This would in turn determine the energy consumption during the preheating stage and throughout the building stage.

During the building stage, energy consumption of the machine could be substantially higher than the preheating stage. Kellens et al. measured the energy consumption of eight different subsystems to analyze the building stage Concept Laser M3 Linear machine [87]. These eight subsystems include: laser unit (including the laser cooling unit), powder dosage chamber, building platform, coater, XY circulation unit, cabinet cooling and the computer unit. As shown in Figure V.3, the power consumption peaks around 3.5 kW during recoating where a sweeping blade delivers a new layer of powder on top of the built layer. The laser unit took on average 2.4 kW in order to maintain its output power at 100 W, which is the most power consuming unit using 68% of the total machine tool power. The laser power consumption remains stable during the recoating mode and varies slightly in the exposure mode. A substantial amount energy in the laser unit is consumed in its cooling unit. The next highest power consuming unit is the cabinet cooling unit taking less than 400 W.

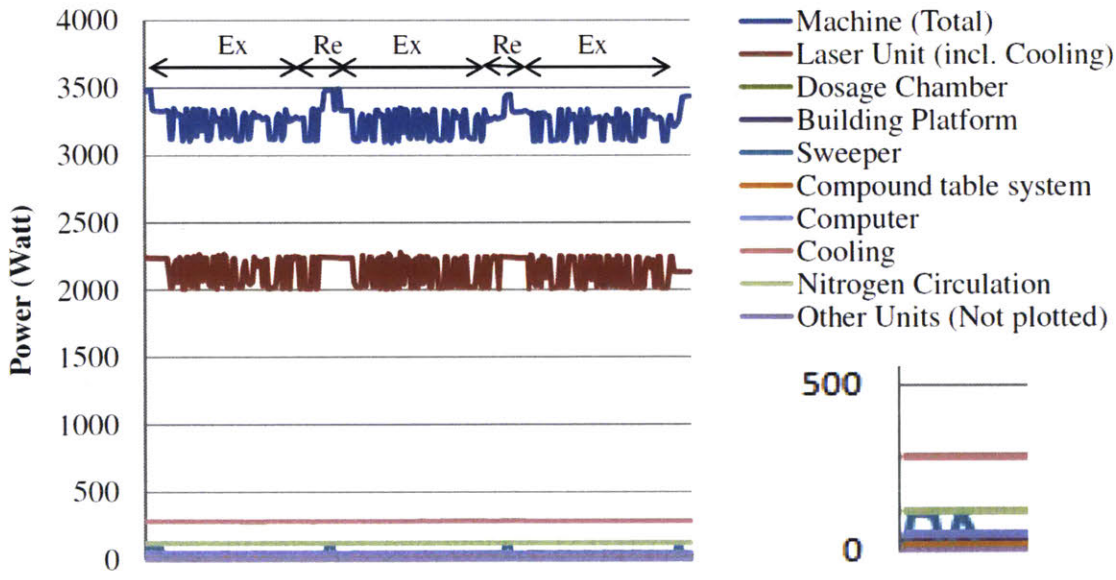

Figure V.3 Power levels during productive modes of Concept Laser M3 Linear machine [87]

While studying the energy consumption of each subsystem helps identify the critical energy consuming unit, an energy model describing the nature of the process is crucial to better understand the energy consumption pattern of the whole process. The model developed by Baumers et al. breaks down the energy investment during the productive modes of the process into two major categories: time dependent base energy consumption and geometry dependent

energy consumption (Equation 5.1). The equation could be explained in greater detail with knowledge of the energy consumption pattern of individual subsystems.

$$E = E_{exposure} \times (V_{part} + V_{support}) + E_{layer} \times N_{layer} + \dot{E}_{base} \times (t_{exposure} + t_{recoating}) \quad \text{Eq. 5.1}$$

$E_{exposure}$ depicts the energy directly related to fusing the selected powder material. The laser unit is operating at a relatively stable high power level all through the productive modes. Theoretically, it is expected that the laser system operates at a higher energy level in the exposure mode. On the contrary, the laser power consumption is higher during the recoating process. It is therefore difficult to separate the material fusion energy from laser unit energy consumption due to this complex nature of the laser system in this particular case (Concept Laser M3 Linear machine). E_{layer} is the energy for the sweeper to deposit a new layer of powder onto the previous layers, which is mainly consumed by electric motors. The recoating energy could be predetermined by the geometry, desired orientation and layer thickness of the part. The size, distribution, shape and flowability of the powder to be used may also be important to theoretically model the energy consumption of recoating. E_{base} is the energy of the rest of the operating systems during exposure and recoating modes, including: base energy consumption of the laser unit (with cooling), nitrogen circulation system, computer system, etc.

Energy consumption and processing rate of a technology plays an important role in determining its industrial applications. Gutowski et al. have plotted the processing rate and electrical power requirements of different manufacturing processes [88]. Most manufacturing processes today operate on power ranging from 5 to 50 kW. The processing rates as well as the specific energy required for each process could vary by orders of magnitude. Powder bed fusion technology is plotted together with other conventional processes in a log-log plot as shown in Figure V.4. In the plot, the two diagonals represent the power rating of a process at 50 kW and 5 kW respectively. The two horizontal lines represent reference for physical constants. The upper line is the energy required to vaporize aluminum, which is about 10 MJ/kg; while the lower line represents the energy required to melt aluminum/iron, which is around 1 MJ/kg. It is observed that the conventional technologies, i.e. machining, injection molding, smelting, etc., fall within the two horizontal lines; while more advanced technologies including oxidation, electric discharge machining are on the left corner of the plot demonstrating for high energy requirement and low throughput.

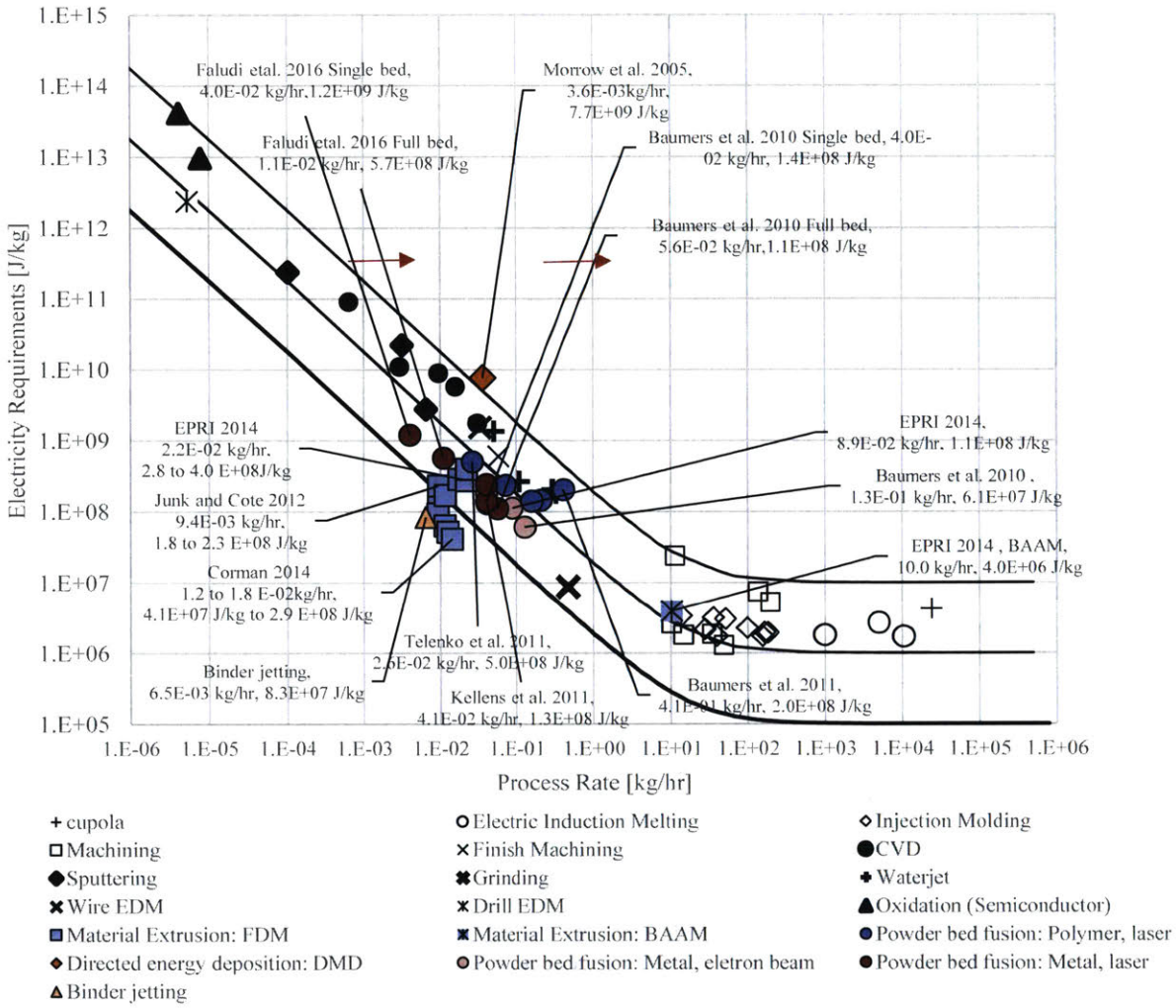

Figure V.4 Electricity requirements as a function of the research reported processing rate (red data points represent metal additive manufacturing processes, blue data points represent polymer additive manufacturing processes), red arrows showing the energy consumption difference between full bed and single bed print utilization

Various researchers looked into energy consumption as an environmental performance for additive manufacturing processes. The collected data on specific energy consumption and process rate are listed in Table V.1 below. To take a deeper look, these data are also plotted on Figure V.4.

Technology	Manufacturer	Model	Material	Process Rate (kg/h)	Electricity Requirements (J/kg)	Reference
Material Extrusion: FDM	Stratasys	Dimension SST 1200es	ABS	9.4E-03	1.8E+08	Junk and Cote 2012
Material Extrusion: FDM	Stratasys	Dimension SST 1200es	ABS	9.4E-03	2.3E+08	Junk and Cote 2012

Material Extrusion: FDM	Stratasys	MOJO	ABS	9.3E-03	9.4E+07	Meatured by Jiang and Corman 2014
Material Extrusion: FDM	Stratasys	MOJO	ABS	1.1E-02	6.4E+07	Meatured by Jiang and Corman 2014
Material Extrusion: FDM	Stratasys	MOJO	ABS	1.3E-02	5.2E+07	Meatured by Jiang and Corman 2014
Material Extrusion: FDM	Stratasys	FDM 1650	ABS	3.8E-03	1.2E+09	Luo et al. 1999
Material Extrusion: FDM	Stratasys	FDM 2000	ABS	1.9E-02	4.1E+08	Luo et al. 1999
Material Extrusion: FDM	Stratasys	FDM 8000	ABS	9.5E-02	8.3E+07	Luo et al. 1999
Material Extrusion: FDM	Stratasys	FDM Quantum	ABS	6.7E-02	5.9E+08	Luo et al. 1999
Material Extrusion: FDM	Stratasys	Mojo	ABS (ABSplus)	1.4E-02	4.1E+07	Corman 2014
Material Extrusion: FDM	Stratasys	Dimension Elite	ABS	1.2E-02	1.7E+08	Corman 2014
Material Extrusion: FDM	Stratasys	Fortus 360 MC	ABS	1.8E-02	2.9E+08	Corman 2014
Material Extrusion: FDM	Stratasys	Fortus 400 MC	ABS M30	2.2E-02	2.8E+08	EPRI 2014
Material Extrusion: FDM	Stratasys	Fortus 900 MC	ABS M30	2.2E-02	4.0E+08	EPRI 2014
Material Extrusion:BAAM	Cincinnati	BAAM	ABS with Carbon fibers	1.0E+01	4.0E+06	EPRI 2014
Stereolithography	3D Systems	SLA 250	SLA 5170 Epoxy resin	3.7E-02	1.2E+08	Luo et al. 1999
Stereolithography	3D Systems	SLA 3000	SLA 5170 Epoxy resin	7.3E-02	1.5E+08	Luo et al. 1999
Stereolithography	3D Systems	SLA 5000	SLA 5170 Epoxy resin	1.4E-01	7.5E+07	Luo et al. 1999
SLS	3D Systems	Spro 60 HD HS	Polymide	2.6E-02	5.0E+08	EPRI 2014
Powder bed fusion: SLS	DTM Corporation	Model 2000	polymer	4.2E-01	1.4E+08	Luo et al. 1999
Powder bed fusion: SLS	DTM Corporation	Model 2500	polymer	4.2E-01	1.1E+08	Luo et al. 1999
Powder bed fusion: SLS	3D Systems	HiQ+HS	Nylon	1.4E+00	5.2E+07	Sreenivasan 2009
Powder bed fusion: SLS	3D Systems	HiQ+HS	Nylon	4.1E-01	1.3E+08	Telenko et al. 2011
Powder bed fusion: SLS	3D Systems	HiQ+HS	Nylon	7.2E-02	2.0E+08	Baumers et al. 2011
Powder bed fusion: SLS	EOS	EOSINT P 390	Nylon	4.1E-02	2.4E+08	Baumers et al. 2011
Powder bed fusion: SLS	EOS	EOSINT P760	PA 3200	2.1E-01	1.3E+08	Kellens et al. 2011
Powder bed fusion: SLS	EOS	EOSINT P760	PA 2200	1.6E-01	1.5E+08	Kellens et al. 2011

Powder bed fusion: SLS	EOS	EOSINT P760	PA 2200	1.8E-01	1.4E+08	Kellens et al. 2011
Binder jetting (Print only)	Exone	M-lab	Metal	6.5E-03	8.3E+07	EPRI 2014
Directed energy depostion: DMD	Customized	N/A	Tool Steel H13	3.6E-05	7.7E+09	Morrow et al. 2005
Powder bed fusion: SLM	Renishaw	AM 250	Aluminum Alloy	4.0E-03	5.7E+08	Faludi etal. 2016 Full bed
Powder bed fusion: SLM	Renishaw	AM 250	Aluminum Alloy	1.1E-02	1.2E+09	Faludi etal. 2016 Single bed
Powder bed fusion: SLM	MTT UK, 09	SLM 250	Steel 316L	5.6E-02	1.1E+08	Baumers et al. 2010 Full bed
Powder bed fusion: SLM	MTT UK, 09	SLM 250	Steel 316L	4.0E-02	1.4E+08	Baumers et al. 2010 Single bed
Powder bed fusion: DMLS	EOS	EOSINT M270	Steel	4.0E-02	2.4E+08	Baumers et al. 2012
Powder bed fusion: EBM	Arcam Ab, 10	Arcam A1	Titanium, Ti-6Al-4V	1.3E-01	6.1E+07	Baumers et al. 2010 Full bed
Powder bed fusion: EBM	Arcam Ab, 10	Arcam A1	Titanium, Ti-6Al-4V	4.0E-02	1.8E+08	Baumers et al. 2010 Single bed
Powder bed fusion: EBM	Arcam	Q10	Titanium, Ti-6Al-4V	8.9E-02	1.1E+08	EPRI 2014

Table V.1 Table of collected data on process rate and electricity requirement for differnet additive manufacturing processes, shaded data are not plotted in Figure V.4

Luo et al. 1999 was among the first researchers to direct their interest on environmental performance analysis for additive manufacturing processes [89]. In their paper, polymer powder bed fusion (SLS), material extrusion (FDM), stereolithography (SL) processes were studied. The process rate was calculated by multiplying printing velocity with track width and depth using parameters collected from spec sheet. The specific energy consumption was then determined with listed power of the machines. These calculations, however, could be off for a magnitude of order when compared to measured results. As a result, these data are not included in Figure V.4.

Morrow et al. 2006 reported the specific energy consumption and process rate for using directed energy deposition technology (DMD) [81]. With their customized DMD machine, the energy directly associated with material deposition and laser heating was measured to be 7708 MJ/kg (the energy for powder production is not included for this value.). In their study, an injection mold insert was printed at a process rate of 0.036 g/hr. Low process rate is the major for the high specific energy consumption result. The customized system was equipped with a CO_2 laser (wavelength 10.6 μm) to heat deposited powder material. The laser absorptivity for steel is usually lower at wavelength of 10.6 μm than at 1.06 μm as was discussed in Chapter IV. According to the measurement by Tolokno et al. 2000, the powder bed absorptivity for iron is 64% at 1.06 μm wavelength and 45% at 10.6 μm. In addition, CO2 lasers have worse energy

efficiency than fiber lasers due to the different cooling system setups. Optomec, a manufacturer for directed energy deposition machines, reports process rate of 0.5 kg/hr with 1 kW fiber laser equipped [90]. Although little information is reported for acquiring the process rate, the spec sheet data would still be a closer estimate to commercialized machine.

Material extrusion process, specifically FDM, and powder bed fusion process have been the center of environmental research topics for the past decade. This is due to the capability of both technologies to produce functional part and the success of industrial commercialization.

Junk and Cote 2012 measured the energy consumption of Stratasys Dimension SST 1200es machine printing throttle valves (shown in Figure V.5 below) [91]. The specific energy was measured to be 180 MJ/kg to 230 MJ/kg depending on different level of material filling. Process rate is calculated to be 9.4 g/hr. Baumers et al. 2011 measured energy consumption for printing single and full bed of a sample part (shown in Figure V.6 below) on a Fortus 400MC machine [92]. They found that while the process rate is low at around 20 g/hr, the specific energy consumption was measured to be 536 MJ/kg for single part experiment and 519 MJ/kg for full bed settings. Corman 2014 measured the energy consumption and process rate of three different size Stratasys FDM machines (Mojo, Dimension Elite, Fortus) [3]. A NIST testing part was built in each measurement as shown in Figure III.5. Only the energy consumption during the build phase was considered for specific energy consumption calculation. The process rate ranges from 12 g/hr to 18 g/hr and specific energy consumption from 41 MJ/kg to 290 MJ/kg for increasing machine size (build area). EPRI 2014 also measured the process of printing NIST testing parts on two Fortus machines with big build area [26]. The process rate was measured to be 22 g/hr with energy consumption from 280 MJ/kg to 400 MJ/kg. It can be observed that the process rate for different scale machine is rather constant at around 10 g/hr, while the specific energy consumption increases noticeably with the size of the machines. The low throughput results from the constraints on the filament heating and dispensing mechanisms which does not change across all size machines. The increasing energy consumption trend results from the heating of increased build chamber area, while heating and dispensing material only accounts for less than 1% of the total consumed energy. More details could be found in Chapter III.

Figure V.5 Throttle valve printed on Dimension SST 1200es with ABS material machine [91]

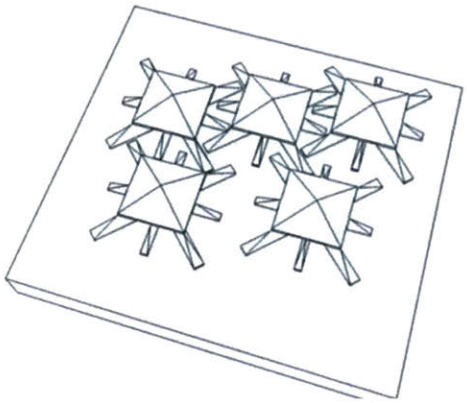

Figure V.6 Sample parts printed on a Fortus 400MC with ABS material machine [92]

Kellens et al. 2011 studied the energy consumption of eight different subsystems to analyze the building stage Concept Laser M3 Linear machine as mentioned earlier in this section [87]. The specific energy consumption for printing AISI 316L steel part was measured to be 97 MJ/kg. Baumers et al. 2010 studied the effect of print volume utilization on specific energy consumption [66]. Sample parts with the same geometry as shown in Figure V.6 were printed with SAE 316L steel powders on a MTT SLM 250 (now Renishaw AM 250) machine both as a single part and as a full bed of six. 140 MJ/kg energy was required to print a single part at the process rate of 0.04 kg/hr, while 110 MJ/kg was measured to successfully print six parts at the rate of 0.056 kg/hr. The process rate and specific energy consumption could be improved by half an order of magnitude as shown in Figure V.4 by arrows. Faludi et al. also conducted experiments to compare embodied energy for printed turbine samples with different print volume utilization (one turbine versus twelve turbines) as shown in Figure V.7 below [93]. The turbines were printed with aluminum alloy powder AlSi10Mg; each turbine weighs 58 g. They measured the energy consumption during the print job including machine warm up phase, build phase, and cool down phase. Note that energy consumption by a chiller used to cool down the laser system was measured separately. In addition, energy consumption during powder sieving and cleaning chamber with vacuum immersion separators were also measured and included in determining the total energy during manufacturing. They found that for the specific energy for printing one part is 1.2 GJ/kg at a processing rate of 0.004 kg/hr, while for printing twelve parts (full bed) is 570 MJ/kg at the processing rate of 0.011kg/hr. Due to the difference in material, the specific energy in this study is much higher than studies reported by Baumers et. al and Kellens et al. Moreover, the energy consumed by the chiller for laser system consisted almost half of the total build phase energy. It is therefore crucial in all the studies to clarify whether the chiller energy consumption is measured and included.

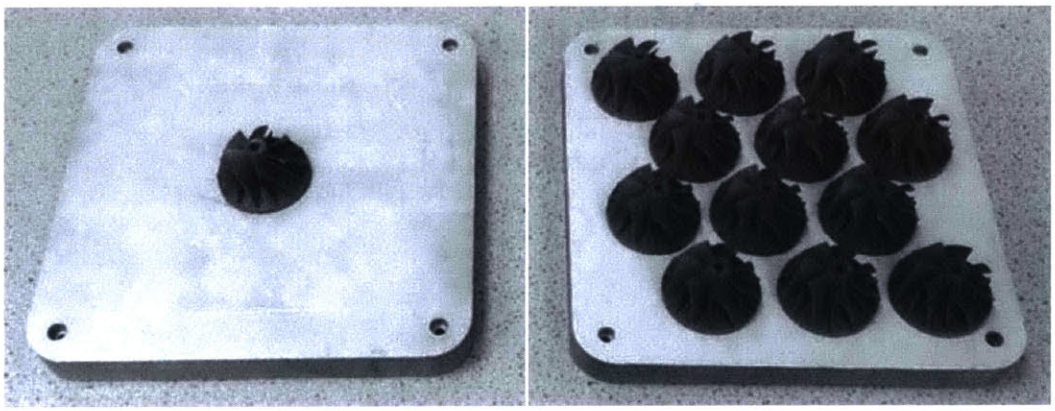

Figure V.7 Different build volume utilization for printing turbines

The technology used in post processing the part built by metal powder bed fusion machine consists many separate conventional processes. The post processing usually involves sawing/wire EDM to take the part off the building platform, hand machining (e.g. with dremel tools) to remove supporting structures, conventional machining (e.g. milling, drilling, etc.) to achieve accurate geometry and good surface finish. When wire electrical discharging machining is applied to separate printed parts from the substrate, substantial energy is added to the

embodied energy of the final product. According to Faludi et al., 33 MJ is required to remove a single part from the substrate with wire EDM and 142 MJ for full print bed scenario [93]. The part separation energy would in turn consists 33% and 26% respectively in total energy consumed by the product. Heat treatment is also usually applied to achieve good mechanical properties. The post processing for metal powder bed fusion could be lengthy and therefore less of interest to the researchers, but it can play a very important role in obtaining major long term goals of additive manufacturing (e.g. fully automatic system, desktop sized high power machine, etc.). It would be beneficial to standardize the post processing methods and even make it more automatic.

Sreenivasan and Bourell 2009 reported their study on environmental performance of polymer powder bed fusion process [94]. The calculated the process rate and energy consumption following the same method reported by Luo et al. in 1999. The results (1.35 kg/hr, 37.7 MJ/kg) is therefore not plotted in Figure V.4. Kellens et al. 2011 studied energy consumption of printing nylon powders with an EOS P760 machine [87]. The process rate was reported to be from 0.16 kg/hr to 0.21 kg/hr for a series of experiments. The specific energy consumption ranged from 130 MJ/kg to 150 MJ/kg. Telenko et al. 2012 studied the energy efficiency of polymer powder bed fusion processes (Selective laser sintering/SLS) for printing nylon parts with 3D systems HIQ+HS system [18]. Paintball gun holders were printed in the experiment as shown in Figure V.8 below. The process rate was not directly reported, but could be estimated from the geometry of the parts printed to be 0.41 kg/hr. The specific energy consumption was measured to be 130 MJ/kg. Baumers et al. 2011 also studied the energy consumption on polymer powder bed fusion processes [19]. A prosthetic part was printed on both 3D systems HIQ+HS machine and EOS P 390 machine with nylon based powders as shown in Figure V.9 below. The process rate was measured to be 0.072 kg/hr and 0.041 kg/hr respectively. The specific energy consumption was measured to be 200 MJ/kg and 240 MJ/kg.

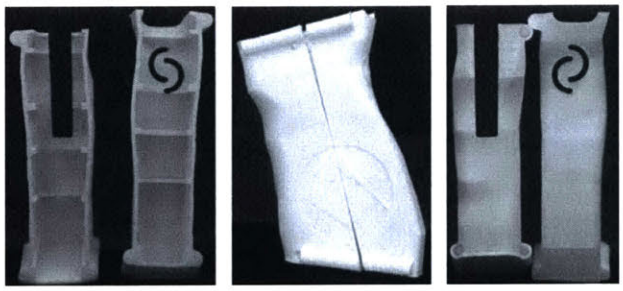

Figure V.8 Paintball gun holder [18]

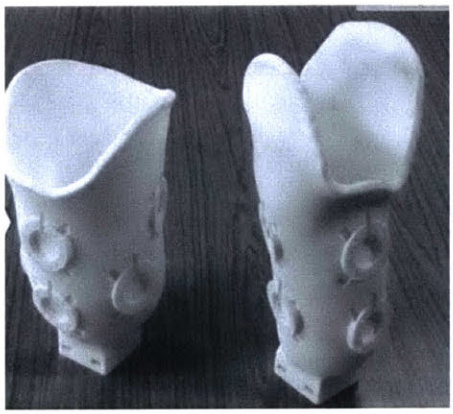

Figure V.9 Prosthetic part [19]

It is worthwhile noting that in polymer powder bed fusion processes, a noticeable faction of energy is utilized to heat up the chamber and material within to an elevated temperature. For nylon powders, as an example, the powders within the chamber is heated up to over 170 °C while its melting temperature (or glaze point) is from 172 to 180 °C [19]. The chamber is usually kept at a temperature higher than the crystallization temperature of the material, which increases

the crystallization of the molten material [95]. For a rough estimate in this calculation, full crystallization is assumed. The adiabatic modeled rate could therefore be underestimated. The powder bed to be sintered is only a few degrees away from melting temperature. For this calculation, the temperature difference is assumed to be 10 °C which was also taken as parameters in practice [95]. In order to heat the powders to such high temperature, the chamber heating process could take up to 40% of the total power consumed while running [87]. We applied simple adiabatic model to polymer powder bed fusion processes with parameters listed below. The processing rate is calculated to be within 1.23 kg/hr for 50W laser at different bed temperature. The results reported by Baumers et al. 2011 [19] is around 6% of the adiabatic model rate. A potential cause for such low adiabatic efficiency is the low thermal conductivity of polymer material (0.127 to 0.144 W/mK [96]) which inquires more time for heat to transfer from the surface to the bottom of the printing layer. Additionally, the numbers reported by Baumers et al. was based on the build time of a sample part which included recoating time and scanning inefficiency. A better comparison to the adiabatic printing rate would be the printing rate of a single track during the build of a sample part.

Parameter	**Value**	**Reference**
Heat capacity [J/(kg-^{0}C)]	2350	[96]
Melting temperature [^{0}C]	184	[96]
Plate temperature [^{0}C]	175-185	[19]
Latent heat [J/kg]	115,000	[96]
Laser material absorption rate	0.95	[97]

Table V.2 PA 2200 parameters used in modeling

3. Manufacturing energy consumption comparison between metal powder bed fusion and conventional manufacturing

Various research groups have attempted to assess the lifecycle energy consumption of parts made with additive manufacturing technology. By comparing them to conventional technologies, they're seeking the boundaries within which additive manufacturing shows advantages in terms of energy consumption. In this section, case studies comparing the energy consumption for the two different manufacturing methods will be reviewed.

3.1 Light weight metal aircraft components (forging, machining versus powder bed fusion)

Huang et al. compared the lifecycle energy consumption of several aircraft components produced with both powder bed fusion technology and conventional technologies (milling, grinding, forging, etc. [98], concluding with the results that adopting additive manufacturing could lead to significant energy savings from reduced weights.

The examples in this study demonstrates a weight reduction ranging from 35% to 65% because of design freedom. To reduce weight, hollow structures and complex geometries are largely applied as can be seen in Figure V.10 below. Meanwhile, the comparison assumes the buy-to-fly ratio for conventional manufacturing to be 8:1 for subtractive machining and 4.5 to 1 for forming, while the buy-to-fly ratio for additive manufacturing is 1.5 to 1. According to Huang et al., buy-to-fly ratio is defined as the ratio of the mass of raw material needed per unit mass of finished component [98]. Note that, not all the unused/unsintered powders in a job could be reused directly considering the standards of the application. Some processes would require virgin powder or the powders to be recertified to build their part. The low buy-to-fly ratio for powder bed fusion process is based on the assumption of the possibility to reuse most of the unused powder.

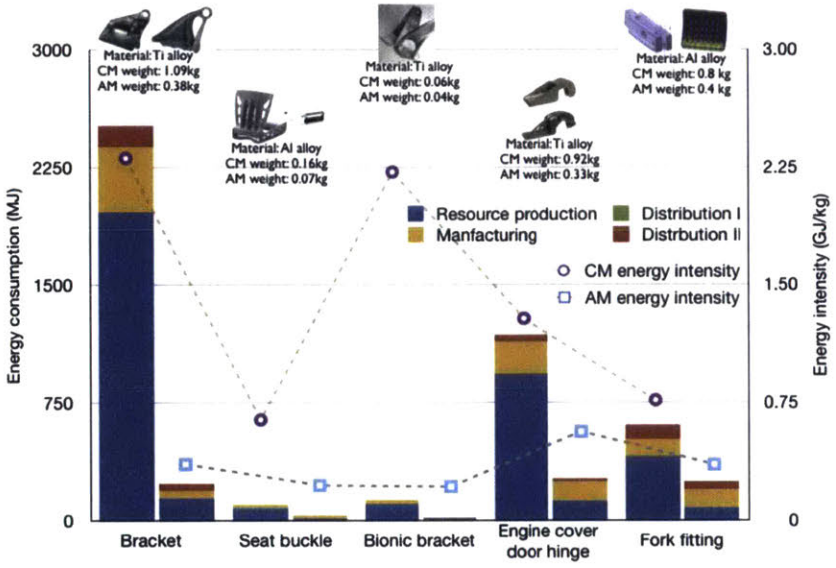

Figure V.10 Cradle to gate primary energy results for case study components [98]

Throughout the study, the energy efficiencies of different processes were assumed to be the same for different materials due to lack of data.

The powder metallurgy process (gas atomization) is assumed to have the same energy efficiency, for which energy consumption scales with the energy required to heat the material to melting temperature. Huang et al. reported the estimates for atomization energy to be around 20MJ/kg for different materials (Ti, Ni, Al alloy, Steel). Note that latent heat of fusion is not included in the scaling, nor the use of inert gases to prevent oxidation during atomization.

The energy for machining process is assumed to scale with the strain energy required for metals deformation under linear plasticity. It is reported by Huang et al. that primary energy intensity for milling and machining ranges from 3MJ/kg for aluminum to 160MJ/kg for titanium. According to Dahmus and Gutowski, strain energy (or specific cutting energy) consists only one part of the total energy required in actual production, additional energy are required for auxiliary equipment (e.g. workpiece handling equipment, cutting fluid handling equipment, computer, etc.) [99]. When breaking down the machining energy, the specific cutting energy consists 48.1% to 69.4% of the total depending on the machine used. Adopting a universal scaling factor will thus introduce uncertainty to the estimation of machining energy.

Powder bed fusion process is also assumed to have the same energy efficiency. The specific energy for powder bed fusion is also assumed to scale with the energy required to heat the material to melting temperature. Huang et al. reported primary energy intensity for laser powder bed fusion process ranging from 70MJ/kg for aluminum alloy to 800MJ/kg for Titanium.

Using the above assumptions, Huang et al. estimated the energy savings for the five different cases. Their results showed a great reduction in energy consumption by an average of 50 to 70% per kg final product. The case study is applicable to scenarios where drastic differences exist between weights of the materials processed with conventional and additive methods: high buy-to-fly ratio with conventional manufacturing versus low buy-to-fly ratio with additive manufacturing, the existence of unique light weight design via additive manufacturing. These requirements in turn may limit the application to unique industries like aerospace.

3.2 Repair industrial gas turbine burner (conventional manufacturing versus powder bed fusion)

Walachowicz et al. from Siemens compared energy consumption for repairing an industrial gas turbine burner with conventional manufacturing methods and with powder bed fusion process [84]. They demonstrated energy savings to repair the gas turbine burner with additive manufacturing process.

The gas turbine burner tip needs to be repaired after every 20,000 hours of operation. The convention method involves replacing the damaged parts with new prefabricated interchangeable parts of the same function, geometry and material. Due to the nature of nickel based super alloy, a large portion of the burner need to be removed including undamaged parts (nozzle, burner ring spacer, mixing tube, clamp pipe, etc.). In addition, during production of the nickel based super alloy parts, a lot of waste material is generated because of the limited number of shaping process

allowed for this high strength material. As a result, the conventional process has a high buy-to-fly ratio.

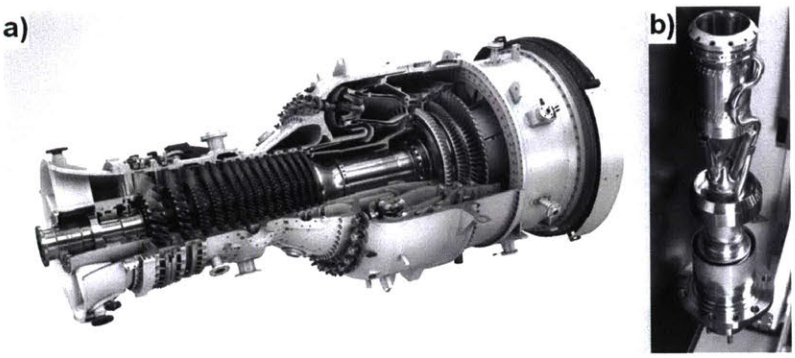

Figure V.11 (a) 50 MW class gas turbine Siemens SGT-800 with annular combustion chamber fired by 30 burners and (b) a burner after refurbishment using Additive Manufacturing repair process

When using additive manufacturing process to repair the burner tip, only the tip which is made from nickel based super alloy needs to be removed. The burner is then mounted onto a customized EOS M 280 machine where powder material is deposited layer by layer and selectively melted. The printed tip then undergoes finishing process which includes polishing.

Sankey diagrams were constructed to illustrate the measured energy and mass flow for both conventional and additive manufacturing repairing processes as shown in Figure V.12 below. For both repairing processes, primary data was collected through measurement in Siemens facility and external suppliers while data for upstream processes was modeled with generic data from ecoinvent v3.1. Note that Argon consumption is also measured for additive manufacturing repairing method along with the electricity consumption during the process.

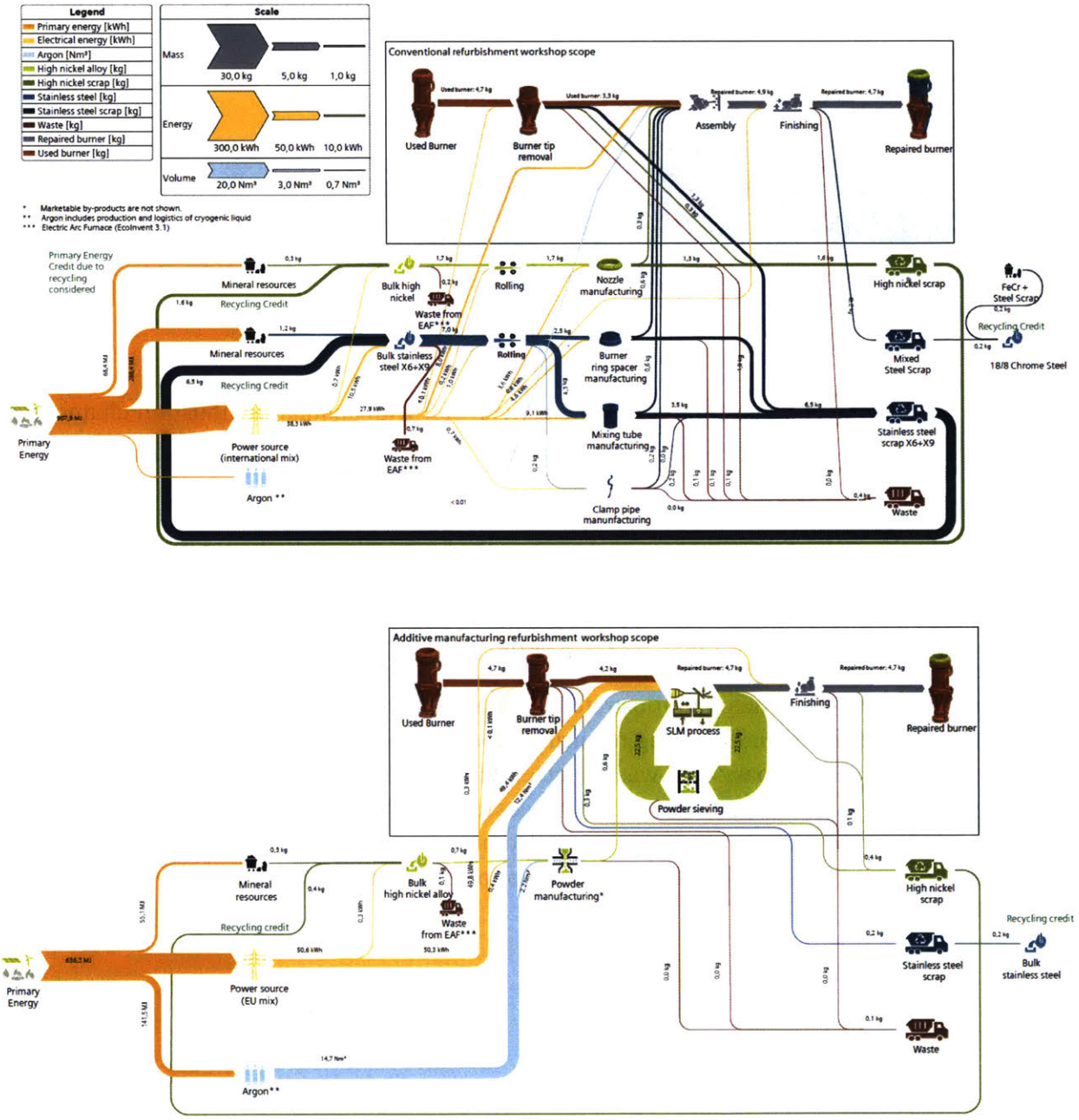

Figure V.12 Sankey diagram for energy and mass flows for the conventional burner tip (A, upper) and additive manufacturing (B, lower) repair process (measured), and individual primary energy contributions (LCA calculation) [84]

The energy used to additively print the 0.6 kg nickel alloy tip is 182.2 MJ (primary energy 439.6MJ), which is the biggest sector of all the energy consumed. It is assumed that the unmolten loose powder are nearly fully recycled. The primary energy for Argon is 141.5 MJ, which is 22.2% of the total energy consumed. For conventional repairing process, the majority of

the energy is also consumed by the manufacturing process. 13.0 MJ is consumed in manufacturing 1.6 kg of nickel alloy.

Although, the energy required to process unit material is much higher for powder bed fusion than for conventional manufacturing methods, the high buy-to-fly ratio offsets and reverts the total energy consumption for the process. It is also important to note that, the embodied energy of Argon used in the printing process could be substantial and therefore has a big impact in the embodied energy of the final product, especially for reactive powders which require Argon atmosphere in storage.

3.3 Nylon paintball gun handles (injection molding versus powder bed fusion)

Due to lack of research in comparing energy consumption for metal parts made with conventional and additive technologies, a case comparing energy consumption for parts made with Nylon will be reviewed in this section. Powder bed fusion process for polymer material hasn't been discussed in depth in the previous chapters, but it demonstrates similar pros and cons when compared to conventional processes.

Telenko and Seepersad compared the energy efficiency of selective laser sintering and injection of molding paintball gun handles as shown in Figure II.16 and also Figure V.13 below [18].

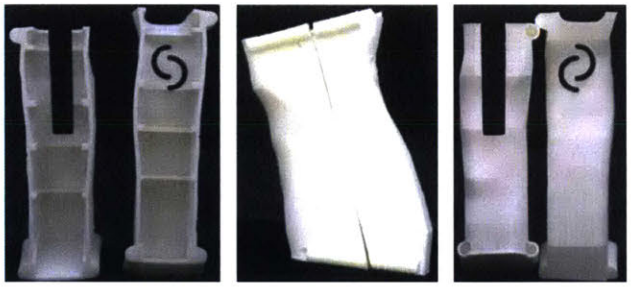

Figure V.13 Paintball gun holder [18]

Telenko and Seepersad assumed same material (Nylon) being used for powder bed fusion and injection molding processes with different yield in material production and manufacturing. The specific energy consumption for making nylon 12 granulate is assumed to be 116MJ/kg from GaBi. The material production yield for injection molding is taken as 100%, while for powder bed fusion 98%. During the manufacturing phase, yield for injection molding is taken as 90%, while for powder bed fusion a 60% yield is assumed taking into account powder utilization and used powder disposal.

The energy consumption during manufacturing for injection molding is broken down into two parts: energy consumed to produce steel mold and energy directly related to the molding process. The energy consumption during manufacturing for powder bed fusion is also broken down into two parts: energy consumed to preheat the building chamber and energy directly related to printing process. For both processes, the first energy component is a fixed value, and the second component varies with the number of parts.

The total energy consumption for material production and manufacturing of parts made with the two processes are shown in Figure V.14 and Figure V.15 below. For powder bed fusion process, energy consumption during direct printing and material production dominates the total energy consumed. When shown as energy per part (Figure V.15), powder bed fusion appears to be less energy intensive than the tool making at low production volume. This is mainly because of high variable energy component and low fixed energy component during powder bed fusion production compared to injection molding. Specific energy during the manufacturing phase for powder bed fusion can be calculated to be 130MJ/kg for full build and 145MJ/kg for small build.

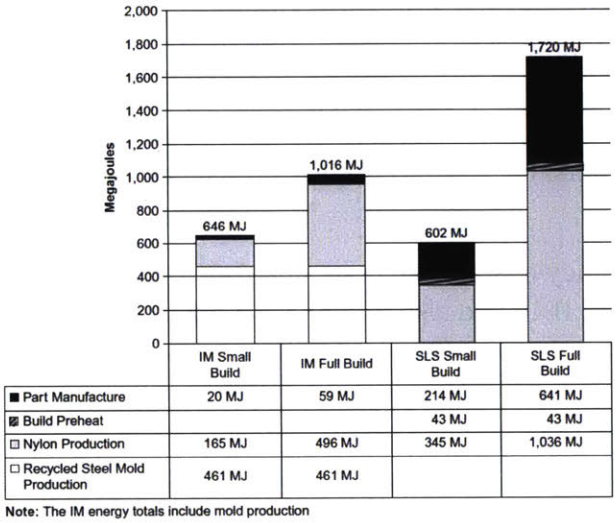

Figure V.14 The energy breakdown for IM and SLS of small (nparts = 50) and full (nparts = 150) builds of a representative part [18]

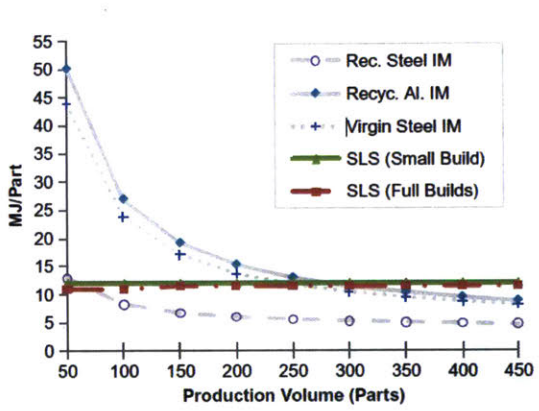

Figure V.15 Total energy use per part versus production volume for SLS and IM of the paintball handle [18]

This case study explores the scenario in which energy consumption for powder bed fusion could be smaller at low production volume when significant tool making energy is required upfront for conventional manufacturing. In addition, utilizing number of products built per job could help reduce the specific energy consumption. According to the research, with small build (50 parts) energy required to produce each part is 12.0 MJ, while for full build (150 parts) energy required per part is 11.5 MJ. This is mainly due to the fixed energy consumption during machine pre-heat consists a smaller fraction in the total energy consumed at better bed utilization.

4. Conclusion

Energy consumption for powder bed fusion processes are typically higher than conventional methods during mass production due to its inherent inefficiency in energy use. Researchers have identified scenarios in which energy consumed by powder bed fusion process is favorable to conventional methods. Powder bed fusion process could save energy when parts made conventional method have high buy-to-fly ratio or require tooling upfront for small production

volume. These scenarios are limited to specific industries and particular applications. In order to expand the application boundary and make powder bed fusion more competitive to conventional manufacturing, the energy efficiency of laser melting powder material needs further improvement.

VI. Conclusion and Future Work

Additive technologies are increasingly involved in design and manufacturing due to their capability of printing unique complex-shaped geometries with relatively short amount of time. The idea of generating a part layer by layer from a computer aided design of three dimensional geometry gave birth to an expanding industry now surpasses 5.1 billion dollars [4]. New machines are being developed for various new applications and for new materials every day. ASTM Committee F42 took an initiative to categorize these new machines into seven technology groups[2]. With its help, we are able to study the unique working principles of each category without the risk of much redundant work.

When additive technologies are used in design and prototyping, the ease of use and relative fast modeling speed have made them favorable to most conventional technologies such as machining, wood prototyping, etc. For machines developed for manufacturing purposes, however, it is important that they have competitive production rate, energy consumption and cost when compared to other already established technologies. When mass production is considered, additive manufacturing technologies suffer from slow production rate and high energy consumption. To further improve any of these technologies, it is important to understand the physics principles behind in order to find ways to break potential limiting barriers for rate and energy.

In this thesis, we focused on the analysis of processing rate and energy consumption for two most popular additive manufacturing technologies: material extrusion and powder bed fusion. We specifically look into the heat transfer involved in both technologies because both technologies rely on transferring heat into solid-state material to fully melt it before it could be bounded to for a solid layer.

For material extrusion, we analyzed fused deposition modeling (FDM) and big area additive manufacturing (BAAM) technologies. While for both technologies material is selectively dispensed through a nozzle or orifice, the production rate is differed by three orders of magnitude. FDM technology applies heat to wire filament which runs through a 1.8 mm diameter cylindrical liquefier. The heating zone of the liquefier is 2 cm long with good heat insulation. With this setup, the machine is capable of printing rather high resolution parts. A constant wall temperature heat transfer model is developed for this setup, and it is found that the processing rate is limited to around 0.035 kg/hr to ensure a favorable exit temperature. The modeled rate is faster than empirical results which is mainly caused by printing strategy inefficiency and mechanical movement of the nozzle. The model also suggests that the processing rate is proportional to the length of the liquefier and is related to the natural log of the dimensionless temperature. There are several major ways to improve the process rate: increase the length of the heating zone, increase the material temperature before the entrance of the heating zone, change the heat transfer mechanism to be more efficient, etc. Go et al. 2017 [25] further analyzed the rate limiting barriers from mechanical system and resolution requirement, they mapped out a processing window bounded by all three different limiting factors. BAAM technology applies a single screw extruder to melt materials in pellet form. The screw used in the extruder is about 60 cm long. We reviewed a mathematical model developed by Tadmor and Gogos [33], and found

out that viscous heat dissipation dominates the heating of the material compared to the heating from the high temperature wall. The models suggests that the processing rate is related to the helical length of the screw channel, the channel width and the rotational speed of the screw. With estimated parameters for the BAAM setup, the processing rate is calculated to be 160 kg/hr. Some potential reasons for the big process rate difference are: BAAM technology has a much longer heating zone (1 m versus 2 cm) compared to FDM technology, BAAM technology heats up the material with both heat conduction from the wall and viscous dissipation while FDM only utilizes heat transfer from the wall, BAAM technology is printing material at worse resolution compared to FDM (8 mm versus 2 mm).

For powder bed fusion processes, we analyzed the metal powder bed fusion process with laser as the heating source. Three different models were presented with the focus on heat transfer. The adiabatic processing rate model predicts the theoretic maximum processing rate by assuming perfect energy transit into the material. The experiments reported processing rate is much lower than the theoretic limit at the same power. To quantify the effect of heat transfer on limiting the processing rate, some crucial physical parameters involved in the process are reviewed including laser material absorptivity, thermal conductivity, capillarity, etc. It is found out that the absorptivity for metal material can reach its optimum by equipping the system with a 1.06 μm wavelength laser. Moreover, the effective absorptivity is higher in powder bed than dense material. The effective thermal conductivity of a metal powder bed is much lower than that of dense material. Analysis on capillarity shows that penetration of the molten material into the powder bed occurs on a time scale much smaller than material exposure time to the laser. The capillarity is therefore crucial to heat transfer in the depth direction. Based on the findings, each heat transfer model for the whole process can be divided into three sub stages, i.e. volumetric heating, capillary penetration, and heat conduction. In the volumetric heating stage, heat is transferred from laser directly into the depth of the powder layer. Conductive heat transfer is limited due to the low effective thermal conductivity. After the top surface material is melted, the process enters the second stage where the capillary pressure gradient drives the molten material to fill in the pores of the powder bed beneath it. Heat conduction is then modeled in the third stage within the liquid solid mixture. The models show that heat transfer is one of the major limitations to the current processing rate. To achieve higher processing rate, higher laser power and a chamber with elevated temperature is preferred. The processing rate efficiency compared to the adiabatic rate limit is, however, limited by the nature of heat transfer. To improve the efficiency, fundamental change of heat transfer mode is necessary in the future.

We also reviewed energy consumption of powder bed fusion processes since it's been extensively reported. The results showed that specific energy consumption for powder bed fusion processes are higher than conventional processes. Utilizing the print bed volume could alter the specific energy consumption by half to an order of magnitude. When mass production is considered, specific energy consumption for powder bed fusion processes during the build phase is usually not favorable compared to conventional competitors due to its inherent inefficiency in energy use. Researchers have identified a couple energy saving favorable scenarios: high buy-to-fly ratio parts, tooling required upfront, small production volume, etc. These scenarios are, however, limited to specific industries and particular applications.

Although this thesis highlights the limitations from heat transfer on the processing rate of material extrusion and powder bed fusion technologies, the models developed in this thesis are somewhat preliminary by making assumption that would simplify the modeling to achieve analytical results. Finite element analysis could be useful to study the phenomenon with complex boundary conditions. Moreover, the processing rate of these technologies are bounded not only by heat transfer, but also by the mechanical setup of these machines. As a result, many more factors include printing strategy and mechanical movement limitations, should be considered when developing a model to further quantify the processing rate window for a typical process.

VII. Reference

[1] S. V. Murphy and A. Atala, "3D bioprinting of tissues and organs," *Nat. Biotechnol.*, vol. 32, no. 8, pp. 773–785, Aug. 2014.

[2] F42 Committee, "Terminology for Additive Manufacturing Technologies," ASTM International, 2012.

[3] G. Corman, "Energy and Resource Efficiency of Additive Manufacturing Technologies," Master Thesis, RWTH Aachen University, 2014.

[4] T. T. Wohlers, T. Caffrey, and R. I. Campbell, *Wohlers Report 2016: 3D Printing and Additive Manufacturing State of the Industry : Annual Worldwide Progress Report*. Wohlers Associates, 2016.

[5] "3D Printing in Dentistry 2015: A Ten Year Opportunity Forecast and Analysis." [Online]. Available: http%3A%2F%2Fwww.smartechpublishing.com%2Freports%2F3d-printing-in-dentistry-2015-a-ten-year-opportunity-forecast-and-analysis. [Accessed: 10-Jul-2015].

[6] J.-P. Kruth, G. Levy, F. Klocke, and T. H. C. Childs, "Consolidation phenomena in laser and powder-bed based layered manufacturing," *CIRP Ann. - Manuf. Technol.*, vol. 56, no. 2, pp. 730–759, 2007.

[7] R. M. German, P. Suri, and S. J. Park, "Review: liquid phase sintering," *J. Mater. Sci.*, vol. 44, no. 1, pp. 1–39, Jan. 2009.

[8] R. M. German, *Powder Metallurgy Science*. Metal Powder Industries Federation, 1994.

[9] H. J. Niu and I. T. H. Chang, "Selective laser sintering of gas and water atomized high speed steel powders," *Scr. Mater.*, vol. 41, no. 1, pp. 25–30, Jun. 1999.

[10] R. Li, Y. Shi, Z. Wang, L. Wang, J. Liu, and W. Jiang, "Densification behavior of gas and water atomized 316L stainless steel powder during selective laser melting," *Appl. Surf. Sci.*, vol. 256, no. 13, pp. 4350–4356, Apr. 2010.

[11] A. b. Spierings, N. Herres, and G. Levy, "Influence of the particle size distribution on surface quality and mechanical properties in AM steel parts," *Rapid Prototyp. J.*, vol. 17, no. 3, pp. 195–202, Jan. 2011.

[12] M. Badrossamay, E. Yasa, J. Van Vaerenbergh, and J.-P. Kruth, "Improving Productivity Rate in SLM of Commercial Steel Powders," *Pap. Present. RAPID 2009 Conf. Expo. Schaumbg. IL*, 26-27 May.

[13] W. Meiners, K. Wissenbach, and A. Gasser, "Selective laser sintering at melting temperature," US6215093 B1, 10-Apr-2001.

[14] P. J. Apinya Laohaprapanon, "Optimal Scanning Condition of Selective Laser Melting Processing with Stainless Steel 316L Powder," *Adv. Mater. Res.*, vol. 341–342, pp. 816–820, 2012.

[15] H. Schleifenbaum, A. Diatlov, C. Hinke, J. Bültmann, and H. Voswinckel, "Direct photonic production: towards high speed additive manufacturing of individualized goods," *Prod. Eng.*, vol. 5, no. 4, pp. 359–371, Aug. 2011.

[16] D. Buchbinder, H. Schleifenbaum, S. Heidrich, W. Meiners, and J. Bültmann, "High Power Selective Laser Melting (HP SLM) of Aluminum Parts," *Phys. Procedia*, vol. 12, Part A, pp. 271–278, 2011.

[17] N. Hopkinson and P. M. Dickens, "Analysis of rapid manufacturing—using layer manufacturing processes for production," *Proc. Inst. Mech. Eng. Part C J. Mech. Eng. Sci.*, no. 217 (C1), pp. 31–39, 2003.

[18] C. Telenko and C. C. Seepersad, "A comparison of the energy efficiency of selective laser sintering and injection molding of nylon parts," *Rapid Prototyp. J.*, vol. 18, no. 6, pp. 472–481, 2012.
[19] M. Baumers, C. Tuck, D. L. Bourell, R. Sreenivasan, and R. Hague, "Sustainability of additive manufacturing: measuring the energy consumption of the laser sintering process," *Proc. Inst. Mech. Eng. Part B J. Eng. Manuf.*, vol. 225, no. B12, pp. 2228–2239, Dec. 2011.
[20] W. J. Swanson, J. S. Batchelder, K. C. Johnson, T. A. Hjelsand, and J. W. Comb, "Print head assembly and print head for use in fused deposition modeling system," US8647102 B2, 11-Feb-2014.
[21] P. J. Leavitt, "Extrusion head for use in extrusion-based layered deposition modeling," US7625200 B2, 01-Dec-2009.
[22] M. E. Adams, D. J. Buckley, and R. E. Colborn, *Acrylonitrile-butadiene-styrene Polymers*. iSmithers Rapra Publishing, 1993.
[23] "Acrylonitrile Butadiene Styrene (ABS) Typical Properties Generic ABS | UL Prospector." [Online]. Available: https://plastics.ulprospector.com/generics/1/c/t/acrylonitrile-butadiene-styrene-abs-properties-processing. [Accessed: 23-Jan-2017].
[24] J. H. Lienhard and J. H. Lienhard, *A heat transfer textbook*. Mineola, N.Y. : Dover Publications, c2011., 2011.
[25] J. Go, S. N. Schiffres, A. G. Stevens, and A. J. Hart, "Rate limits of additive manufacturing by fused filament fabrication and guidelines for high-throughput system design," *Addit. Manuf.*, vol. 16, pp. 1–11, Aug. 2017.
[26] Marek Samotyj, "What is Advanced Manufacturing and Why Should We Care About It?," presented at the Silicon Valley Manufacturing Roundtable Meeting, 24-Sep-2014.
[27] "Visit to Oak Ridge National Laboratory," Dec-2014.
[28] M. J. Stevens and J. A. Covas, "Principles of melt flow in single-screw extruders," in *Extruder Principles and Operation*, Springer Netherlands, 1995, pp. 127–174.
[29] H. S. Rowell and D. Finlayson, "Screw viscosity pumps," *Eng. 00137782*, vol. 126, pp. 385–387, Sep. 1928.
[30] B. H. Maddock, "A Visual Analysis of Flow and Mixing in Extruder Screws," *SPE J.*, vol. 15, pp. 383–389, 1959.
[31] Z. Tadmor and C. G. Gogos, *Principles of polymer processing*. Hoboken, N.J. : Wiley-Interscience, c2006., 2006.
[32] Z. Tadmor and I. Klein, *Engineering principles of plasticating extrusion*. Van Nostrand Reinhold Co., 1970.
[33] Z. Tadmor, "Fundamentals of plasticating extrusion. I. A theoretical model for melting," *Polym. Eng. Sci.*, vol. 6, no. 3, pp. 185–190, Jul. 1966.
[34] "3ders.org - See how a 3D printed car is really made with Local Motors' 3D Printing 101 | 3D Printer News & 3D Printing News." [Online]. Available: http://www.3ders.org/articles/20160330-see-how-a-3d-printed-car-is-really-made-with-local-motors-3d-printing-101.html. [Accessed: 02-Feb-2017].
[35] C. I. Chung, *Extrusion of Polymers: Theory and Practice*. Hanser Publishers, 2000.
[36] "HanserPublications.com. Analyzing and Troubleshooting Single-Screw Extruders." [Online]. Available: http://www.hanserpublications.com/Products/268-analyzing-and-troubleshooting-single-screw-extrusion.aspx. [Accessed: 02-Feb-2017].

[37] M. Van Elsen, M. Baelmans, P. Mercelis, and J.-P. Kruth, "Solutions for modelling moving heat sources in a semi-infinite medium and applications to laser material processing," *Int. J. Heat Mass Transf.*, vol. 50, no. 23–24, pp. 4872–4882, Nov. 2007.
[38] H. S. Carslaw and J. C. Jaeger, *Conduction of Heat in Solids*. Clarendon Press, 1986.
[39] A. V. Gusarov and I. Smurov, "Modeling the interaction of laser radiation with powder bed at selective laser melting," *Phys. Procedia*, vol. 5, Part B, pp. 381–394, 2010.
[40] F. Verhaeghe, T. Craeghs, J. Heulens, and L. Pandelaers, "A pragmatic model for selective laser melting with evaporation," *Acta Mater.*, vol. 57, no. 20, pp. 6006–6012, Dec. 2009.
[41] Y. Zhang and A. Faghri, "Melting of a subcooled mixed powder bed with constant heat flux heating," *Int. J. Heat Mass Transf.*, vol. 42, no. 5, pp. 775–788, Mar. 1999.
[42] B. Zhang, L. Dembinski, and C. Coddet, "The study of the laser parameters and environment variables effect on mechanical properties of high compact parts elaborated by selective laser melting 316L powder," *Mater. Sci. Eng. A*, vol. 584, pp. 21–31, Nov. 2013.
[43] Y. Zhang, A. Faghri, C. W. Buckley, and T. L. Bergman, "Three-Dimensional Sintering of Two-Component Metal Powders With Stationary and Moving Laser Beams," *J. Heat Transf.*, vol. 122, no. 1, pp. 150–158, Jul. 1999.
[44] T. Mans, "Laser Beam Sources," in *Tailored Light 2*, R. Poprawe, Ed. Springer Berlin Heidelberg, 2011, pp. 155–172.
[45] G. R. Fowles, *Introduction to modern optics*. New York : Dover Publications, 1989, c1975., 1989.
[46] R. Wester, "Absorption of Laser Radiation," in *Tailored Light 2*, R. Poprawe, Ed. Springer Berlin Heidelberg, 2011, pp. 15–41.
[47] *Handbook of the EuroLaser Academy - Volume 2 | Springer.* .
[48] W. M. Steen and J. Mazumder, "Theory, Mathematical Modelling and Simulation," in *Laser Material Processing*, Springer London, 2010, pp. 251–294.
[49] T. J. Wieting and J. T. Schriempf, "Infrared absorptances of partially ordered alloys at elevated temperatures," *J. Appl. Phys.*, vol. 47, no. 9, pp. 4009–4011, Sep. 1976.
[50] G. S. Arnold, "Absorptivity of several metals at 10.6 [mgr]m: empirical expressions for the temperature dependence computed from Drude theory," *Appl. Opt.*, vol. 23, no. 9, pp. 1434–1434, May 1984.
[51] S. V. Garnov, V. I. Konov, A. S. Silenok, O. G. Tsarkova, V. N. Tokarev, and F. Dausinger, "Experimental study of temperature dependence of reflectivity and heat capacity of steels and alloys at continuous wave Nd:YAG laser heating," 1997, vol. 3093, pp. 160–175.
[52] G. Seibold, F. Dausinger, and H. Hugel, "Absorptivity of Nd:YAG-laser radiation on iron and steel depending on temperature and surface conditions," presented at the Proceedings of the Laser Materials Processing Conference. ICALEO 2000. LIA Vol.89, 2000.
[53] J. P. Kruth, L. Froyen, J. Van Vaerenbergh, P. Mercelis, M. Rombouts, and B. Lauwers, "Selective laser melting of iron-based powder," *J. Mater. Process. Technol.*, vol. 149, no. 1–3, pp. 616–622, Jun. 2004.
[54] P. Mercelis and J.-P. Kruth, "Residual stresses in selective laser sintering and selective laser melting," *Rapid Prototyp. J.*, vol. 12, no. 5, pp. 254–265, 2006.
[55] N. K. Tolochko, Y. V. Khlopkov, S. E. Mozzharov, M. B. Ignatiev, T. Laoui, and V. I. Titov, "Absorptance of powder materials suitable for laser sintering," *Rapid Prototyp. J.*, vol. 6, no. 3, pp. 155–161, Sep. 2000.

[56] M. Rombouts, L. Froyen, A. V. Gusarov, E. H. Bentefour, and C. Glorieux, "Light extinction in metallic powder beds: Correlation with powder structure," *J. Appl. Phys.*, vol. 98, no. 1, p. 013533, Jul. 2005.
[57] Y. S. Touloukian, R. W. Powell, C. Y. Ho, and P. G. Klemens, "Thermophysical Properties of Matter - The TPRC Data Series. Volume 1. Thermal Conductivity - Metallic Elements and Alloys," 1970.
[58] A. V. Luikov, A. G. Shashkov, L. L. Vasiliev, and Y. E. Fraiman, "Thermal conductivity of porous systems," *Int. J. Heat Mass Transf.*, vol. 11, no. 2, pp. 117–140, Feb. 1968.
[59] A. V. Gusarov and E. P. Kovalev, "Model of thermal conductivity in powder beds," *Phys. Rev. B*, vol. 80, no. 2, p. 024202, Jul. 2009.
[60] M. R. Alkahari, T. Furumoto, T. Ueda, A. Hosokawa, R. Tanaka, and M. S. Abdul Aziz, "Thermal Conductivity of Metal Powder and Consolidated Material Fabricated via Selective Laser Melting," *Key Eng. Mater.*, vol. 523–524, pp. 244–249, Nov. 2012.
[61] J. Pak and O. A. Plumb, "Melting in a Two-Component Packed Bed," *J. Heat Transf.*, vol. 119, no. 3, pp. 553–559, Aug. 1997.
[62] G. Hofmann and L. Barleon, "Reduced coolability of particle beds as a result of capillary effects at horizontal phase boundaries," presented at the International ANS/ENS Topical Meeting on Thermal Reactor Safety (1986 : San Diego, Calif.), 1986.
[63] M. E. Fraser, W. K. Lu, A. E. Hamielec, and R. Murarka, "Surface tension measurements on pure liquid iron and nickel by an oscillating drop technique," *Metall. Trans.*, vol. 2, no. 3, pp. 817–823, Mar. 1971.
[64] D. Ceotto, "Thermal diffusivity, viscosity and prandtl number for molten iron and low carbon steel," *High Temp.*, vol. 51, no. 1, pp. 131–134, Feb. 2013.
[65] IAEA, "Thermophysical Properties of Materials for Nuclear Engineering: A Tutorial and Collection of Data," 2009.
[66] M. Baumers, C. Tuck, R. Hague, I. Ashcroft and R. Wildman, "A comparative study of metallic additive manufacturing power consumption," in *Solid freeform fabrication symposium*, 2010, pp. 278–288.
[67] "Latent Heat - The Physics Hypertextbook." [Online]. Available: http://physics.info/heat-latent/. [Accessed: 03-Sep-2015].
[68] J. P. Kruth, B. Vandenbroucke, J. van Vaerenbergh, and P. Mercelis, "Benchmarking of different SLS/SLM processes as Rapid Manufacturing techniques," presented at the Proceedings of the PMI, paper 525, Gent, Belgium, 2005.
[69] J.-P. Kruth, M. Badrossamay, E. Yasa, J. Deckers, L. Thijs, and J. V. Humbeeck, "Part and material properties in selective laser melting of metals.," *Proc. 16th Int. Symp. Electromachining ISEM XVI Shanghai*, 2010.
[70] Bochuan Liu, Ricky Wildman, Christopher Tuck, Ian Ashcroft, Richard Hague, "Investigation the effect of particle size distribution on processing parameters optimisation in selective laser melting process," in *International solid freeform fabrication symposium: an additive manufacturing conference. University of Texas at Austin, Austin*, 2011, pp. 227–238.
[71] E. Yasa, J. Deckers, and J.-P. Kruth, "The investigation of the influence of laser re-melting on density, surface quality and microstructure of selective laser melting parts," *Rapid Prototyp. J.*, vol. 17, no. 5, pp. 312–327, Jan. 2011.

[72] C. Kamath, B. El-dasher, G. F. Gallegos, W. E. King, and A. Sisto, "Density of additively-manufactured, 316L SS parts using laser powder-bed fusion at powers up to 400 W," *Int. J. Adv. Manuf. Technol.*, vol. 74, no. 1–4, pp. 65–78, Sep. 2014.
[73] Z. Sun, X. Tan, S. B. Tor, and W. Y. Yeong, "Selective laser melting of stainless steel 316L with low porosity and high build rates," *Mater. Des.*, vol. 104, pp. 197–204, Aug. 2016.
[74] K. Kempen, L. Thijs, J. Van Humbeeck, and J.-P. Kruth, "Mechanical Properties of AlSi10Mg Produced by Selective Laser Melting," *Phys. Procedia*, vol. 39, pp. 439–446, 2012.
[75] "Wiesner et al. 2014 - Multi-Laser Selective Laser Melting," presented at the 8th International Conference on Photonic Technologies LANE, 2014.
[76] C. Van Gestel, "Study of physical phenomena of selective laser melting towards increased productivity," PhD Thesis, École polytechnique fédérale de Lausanne, 2015.
[77] A. V. Gusarov, I. Yadroitsev, P. Bertrand, and I. Smurov, "Model of Radiation and Heat Transfer in Laser-Powder Interaction Zone at Selective Laser Melting," *J. Heat Transf.*, vol. 131, no. 7, pp. 072101–072101, May 2009.
[78] T. R. Society, "Marangoni effects in welding," *Philos. Trans. R. Soc. Lond. Math. Phys. Eng. Sci.*, vol. 356, no. 1739, pp. 911–925, Apr. 1998.
[79] M. Rombouts, J. P. Kruth, L. Froyen, and P. Mercelis, "Fundamentals of Selective Laser Melting of alloyed steel powders," *CIRP Ann. - Manuf. Technol.*, vol. 55, no. 1, pp. 187–192, Jan. 2006.
[80] A. Klassen, T. Scharowsky, and C. Körner, "Evaporation model for beam based additive manufacturing using free surface lattice Boltzmann methods," *J. Phys. Appl. Phys.*, vol. 47, no. 27, p. 275303, Jul. 2014.
[81] W. R. Morrow, H. Qi, I. Kim, J. Mazumder, and S. J. Skerlos, "Environmental aspects of laser-based and conventional tool and die manufacturing," *J. Clean. Prod.*, vol. 15, no. 10, pp. 932–943, 2006.
[82] A. J. Yule and J. J. Dunkley, *Atomization of melts for powder production and spray deposition*. Oxford University Press, 1994.
[83] M. F. Ashby, H. Shercliff, and D. Cebon, *Materials: engineering, science, processing and design*. Butterworth-Heinemann, 2013.
[84] Frank Walachowicz1, Ingo Bernsdorf1, Ulrike Papenfuss1, Christine Zeller1, Andreas Graichen2, and Vladimir Navrotsky2, Noorie Rajvanshi3, and Christoph Kiener1§, "Comparative energy, resource and recycling lifecycle analysis of the industrial repair process of gas turbine burners using conventional machining and additive manufacturing," *J. Ind. Ecol.*, 2017.
[85] N. P. Lavery, D. J. Jarvis, S. G. R. Brown, N. J. Adkins, and B. P. Wilson, "Life cycle assessment of sponge nickel produced by gas atomisation for use in industrial hydrogenation catalysis applications," *Int. J. Life Cycle Assess.*, vol. 18, no. 2, pp. 362–376, Feb. 2013.
[86] O. D. Neikov, I. B. Murashova, N. A. Yefimov, and S. Naboychenko, *Handbook of Non-Ferrous Metal Powders: Technologies and Applications*. Elsevier, 2009.
[87] K. Kellens, E. Yasa, R. Renaldi, W. Dewulf, J.-P. Kruth, and J. Duflou, "Energy and Resource Efficiency of SLS/SLM Processes," presented at the SFF Symposium, 2011.
[88] T. G. Gutowski, M. S. Branham, J. B. Dahmus, A. J. Jones, A. Thiriez, and D. P. Sekulic, "Thermodynamic Analysis of Resources Used in Manufacturing Processes," *Environ. Sci. Technol.*, vol. 43, no. 5, pp. 1584–1590, Mar. 2009.

[89] Y. Luo, Z. Ji, M. C. Leu, and R. Caudill, "Environmental performance analysis of solid freedom fabrication pocesses," in *Proceedings of the 1999 IEEE International Symposium on Electronics and the Environment, 1999. ISEE -1999*, 1999, pp. 1–6.
[90] "OPTOMEC LENS 850R spec sheet," Jan-2017. [Online]. Available: https://www.optomec.com/wp-content/uploads/2014/04/LENS_850-R_datasheet.pdf.
[91] S. Junk and S. Côté, "A Practical Approach to Comparing Energy Effectiveness of Rapid Prototyping Technologies," in *AEPR'12, 17th European Forum on Rapid Prototyping and Manufacturing*, Paris, France., 2012.
[92] M. Baumers, C. Tuck, R. Wildman, I. Ashcroft, and R. Hague, "Energy inputs to additive manufacturing: does capacity utilization matter?," in *Solid Freeform Fabrication Symposium*, Austin (TX), USA., 2011, vol. 1000, pp. 30–40.
[93] J. Faludi, M. Baumers, I. Maskery, and R. Hague, "Environmental Impacts of Selective Laser Melting: Do Printer, Powder, Or Power Dominate?," *J. Ind. Ecol.*, 2017.
[94] R. Sreenivasan, A. Goel, and D. L. Bourell, "Sustainability issues in laser-based additive manufacturing," *Phys. Procedia*, vol. 5, Part A, pp. 81–90, 2010.
[95] R. D. Goodridge, C. J. Tuck, and R. J. M. Hague, "Laser sintering of polyamides and other polymers," *Prog. Mater. Sci.*, vol. 57, no. 2, pp. 229–267, Feb. 2012.
[96] "Properties for powder PA 2200," 30-Jan-2017. [Online]. Available: https://www.shapeways.com/rrstatic/material_docs/mds-strongflex.pdf.
[97] T. Laumer *et al.*, "Fundamental investigation of laser beam melting of polymers for additive manufacture," *J. Laser Appl.*, vol. 26, no. 4, p. 042003, Nov. 2014.
[98] R. Huang *et al.*, "Energy and emissions saving potential of additive manufacturing: the case of lightweight aircraft components," *J. Clean. Prod.*, 2016.
[99] J. B. Dahmus and T. G. Gutowski, "An Environmental Analysis of Machining," presented at the ASME 2004 International Mechanical Engineering Congress and Exposition, Anaheim, California, USA, 2004, pp. 643–652.